

## **Chapter 1 Introduction**

Cancer is a big threat to the human society. According to GLOBOCAN 2012, an estimated 14.1 million new cancer cases and 8.2 million cancer-related deaths occurred in 2012 globally, compared with 12.7 million and 7.6 million, respectively, in 2008.[1] In the United States, cancer is also the second most common cause of death, leading to 1 in every 4 deaths.[2]

### **1.1 Cancer pathology**

A tumor is a population of abnormal cells characterized by temporally unrestricted growth and the ability to grow in at least three different tissue compartments (i) the original compartment, (ii) the mesenchyme of the primary site (tumor invasion) and (iii) a distant mesenchyme (tumor metastasis).[3] Though some tumors grow (e.g. leukemia) as cell suspensions, most tumors grow as solid tissues. Such neoplastic tissues can be divided into three parts: cellular, interstitial and vascular.[4]

Because of the fast growth of tumor cells, the generation process of new blood vessels from the pre-existing ones is vital, since it can transport oxygen and nutrients to the new tumor cells.[5] This process, which is termed as angiogenesis, is a fundamental step during the transition of a tumor from a benign to a malignant state. It is regulated by angiogenic molecules, such as the vascular endothelial growth factor (VEGF).[6] Compared to normal physiological vessels, tumor blood vessels show

abnormalities, including an increased tortuosity, a deficiency in pericytes and an aberrant basement membrane formation, resulting in enhanced permeability of the tumor vasculatures.[7]

The abnormalities of tumor vasculatures result in large pores in the tumor vasculatures, ranging from 100 nm to several hundred nanometers in diameter, [8-10] whereas the normal vessel junctions are around 5-10 nm only. These large pores allow large macromolecules including nanoparticles, to penetrate into tumors.[11, 12] The lymphatic vessels in the tumor area are pressed by the proliferating tumor cells, and most of them are in a collapsed state, which cannot clear out the macromolecules.[13] The greater permeability of the tumor vasculature and the impaired lymphatic system cause a longer retention time for these macromolecules in the tumor area, which is called the enhanced permeability and retention (EPR) effect.[10, 13] In order to take advantage of the EPR effect, the molecular weight of the macromolecules should be 40 kDa at least.[14] The EPR effect can effectively improve the accumulation of macromolecules in the tumor area. The concentration of macromolecules in tumor tissue is thus five to ten times higher than that in normal tissue, 24 h after intravenous injection. [10, 15] The EPR effect has been exploited for the “passive targeting” of tumors by nanoparticles, which can be used for the delivery of conventional small molecule drugs. The EPR effect has been applied by many kinds of drug delivery vehicles since its discovery twenty years ago.[14, 16, 17]

In addition to angiogenesis, another important characteristic of tumor tissue is a relatively low pH. The extracellular pH of a tumor area ranges from 5.8 to 7.8, which

is more acidic than that of normal tissue (pH of 7.4).[18] This is related with the accumulation of lactic acid and carbonic acid by aerobic/anaerobic glycolysis, glutaminolysis and ATP hydrolysis in the cells. In contrast, the intracellular pH of tumor and normal tissue is similar (7.2).

## **1.2 Challenges for cancer therapy**

Current cancer therapy methods include surgery, chemotherapy, radiation therapy, photodynamic therapy (PDT) and thermal therapy. Surgery is the primary method of cancer treatment, however, in many cases cannot remove the tumor tissue completely due to the fact that tumor and normal healthy tissue are virtually indistinguishable to the surgeon's eye. Sometimes, complete surgery cannot be operated on certain kinds of tumors, such as brain tumors, due to their location. Chemotherapy is a method for cancer treatment by using cytotoxic anti-neoplastic drugs, most of which are small molecule drugs. The therapeutic efficacy of chemotherapy is limited by its strong side effects and by multidrug resistance. Radiation therapy uses high energy radiation to kill cancer cells by damaging their DNA. The radiation, consisting of X-rays and gamma rays, can generate OH radicals, which reacts with oxygen or other substrates to create other reactive oxygen species (ROS). Radiation may cause secondary malignancy in the irradiated area and damage normal tissues as well. One potential method to alleviate these side effects is the use of radiosensitizers, which makes tumor cells more sensitized to radiation therapy. Photodynamic therapy (PDT) is a relatively new treatment method, which relies on the reaction between PDT drugs (also known as photosensitizers) and light, resulting in the generation of reactive

oxygen species (ROS). Compared to chemotherapy and radiation therapy, PDT has higher selectivity. However, its efficacy is limited by the penetration depth of the excitation light, the local level of oxygen and the delivery of photosensitizers.

Most chemotherapy drugs, photosensitizers (PDT) and radiosensitizers (for radiation therapy) are small molecule drugs. Often their therapeutic performance can be compromised due to some non-ideal properties, including poor solubility, rapid breakdown of the drug *in vivo*, unfavorable pharmacokinetics, poor biodistribution and lack of selectivity to diseased tissue.[19] In addition, the performance of these small molecule drugs may be abated by the drug-resistance of tumor cells. The cellular drug resistance may be related with altered apoptosis regulation, transport based mechanisms (P-glycoprotein efflux system, the multi-drug resistance associated protein (MRP)).[20, 21]

### **1.3 Nanoparticles for cancer imaging and therapy**

Nanotechnology has the potential to be a powerful delivery vehicle for cancer imaging and therapy.[16, 17, 22-27] For example, a paclitaxel-loaded albumin nanoparticle (nab-paclitaxel, Abraxane) has been approved by the US Food and Drug Administration (FDA) for the treatment of breast cancer, non-small-cell lung cancer (NSCLC) and advanced pancreatic cancer.[28, 29] Depending on their composition, nanoparticles (NPs) can be divided into lipid-based vehicles (liposomes, solid lipid NPs and micelles), polymer carriers (hydrogel NPs, dendrimers), metallic NPs (gold, silver), carbon structures (carbon nanotubes, nano-diamonds) and inorganic NPs (silica-based).[26, 30] The biodistribution and clearance of NPs are strongly

influenced by their properties, such as size, surface charge, shape, composition and surface modification.[31]

It is believed that the diameter of NPs for cancer imaging and therapy should be in the range of 10 to 100 nm for longer circulation in blood and efficient accumulation in tumor tissues.[22] Larger NPs are easily removed by the reticuloendothelial system (RES). Particles smaller than 6 to 8 nm are filtered by the kidney and cleared from the blood circulation. In addition, the average effective pore size of normal endothelium is around 5 nm, and the renal excretion cut-off size has been established to be around 5.5 nm, thus necessitating the use of particles greater than 10 nm in size.[16]

The surface charge of NPs affects their interaction with the local environment, thus influencing the ultimate destination of NPs in the body. NPs with low or neutral charge are usually preferred as a drug delivery vehicle because of their minimal interaction with proteins in the blood vessels.[16, 22, 31] NPs with positive charge may be subjected to nonspecific internalization into cells,[31] whereas negatively charged NPs are repelled by the endothelial cells, which is negatively charged as well.[22, 31]

To minimize the nonspecific interactions and the unfavorable clearance of NPs, polyethylene glycol (PEG) is introduced onto the NP surface, by grafting, absorption or conjugation, which is termed as PEGylation.[32, 33] PEGylation prevents the rapid clearance of NPs from the body, since opsonins are not able to cover the NP surface effectively.[33, 34] One assumption is that this is related with the conformation of the PEG molecules on the NP surface.[33] PEG chains are in an extended conformation

in solution because of their hydrophilicity and flexibility. However, they are converted to a more condensed and higher energy conformation when the proteins are attracted to the NP surface, which may generate an opposing force and repel the proteins away from the NP surface.[33] PEG chains also inhibit the clearance of NPs by neutralizing the surface charge of NPs and increasing the hydrophilicity of the NPs. It is reported that PEG with MW > 2000 would be the most effective to reduce the clearance of NPs.[33]

The NPs can take advantage of the EPR effect and accumulate in the tumor area effectively because of the leaky vasculature structure. In this way, they can carry the drug loads into the tumor area, which is called “passive targeting”.[22] On the other hand, the enhanced accumulation of drug-loaded NPs in tumor areas can also be achieved by the attachment onto the NP surface of tumor-targeting moieties, called “active targeting”. These tumor-targeting ligands on the NP surface can recognize receptors on cancer cells, via receptor-mediated endocytosis.[35-37] They can facilitate the retention time of NPs in the tumor area [38], penetrate into the tumor tissue [39] and even overcome drug resistance by neutralizing the P-glycoprotein-mediated drug efflux pump [40]. Some examples of targeting ligands include peptides, antibodies, aptamers and folate.[41] Compared to molecular-drug conjugates, e.g. polymer-drug conjugates, the NPs can contain multiple targeting moieties on their surface. These multiple ligands can improve the binding affinity of NPs to tumor cells significantly, which is called “multivalency effect”.[42]

#### **1.4 Multifunctional hydrogel nanoparticles**

Hydrogel nanoparticles are one type of nanoparticles, which are three dimensional polymeric networks linked via physical or covalent interaction. They can absorb a large amount of water in aqueous solution, which is due to the hydrophilic groups in the polymer. They can swell and shrink, which can be explained by ion osmotic swelling pressure and ion exchange kinetics.[43] The swelling properties of hydrogels are affected by polymer morphology (structure, porosity), polymer composition (lengths, ionic character and hydrophilicity of the monomers and crosslinkers) and temperature, as well as by factors affecting ionization equilibrium, such as pH and ionic strength. With its unique swelling/deswelling behavior, hydrogels can be designed and prepared to respond to various physical or chemical stimuli. Hydrogels are biocompatible and injectable. Because of these properties, hydrogels are suitable for *in vivo* biomedical applications, e.g. drug delivery systems [17, 22] and tissue engineering [44].

Polymers used for the preparation of hydrogel nanoparticles include natural polymers and synthetic polymers. The natural polymers are alginate, hyaluronan, chitosan, dextran and cellulose. Examples of synthetic polymers include poly(lactic-co-glycolic acid) (PLGA), polyacrylic acid, polyacrylamide, poly(ethylene oxide), polypropylene oxide (PPO), PEO-PPO-PEO block copolymers (Pluronics®) and poly(vinyl alcohol).[17] Hydrogel NPs can be prepared via reverse microemulsion polymerization, physically/chemically cross-linking of polymers and spray drying.

Hydrogel NPs have excellent properties as drug carriers.[17, 27] They combine the advantages of hydrogel biocompatibility with the hydrogel NPs' engineerability and

flexibility, and have enabled multifunctionality, e.g. theranostic treatment, controlled release kinetics, stealth circulation and biodegradability. They are highly soluble in water, and can be made controllably biodegradable.[45] They can carry high payloads of drugs and also protect its contents from interference by enzymes in the living biological environment, as well as enabling specific targeting of cancer cells by attachment with surface ligands.[27] The drugs are loaded into NPs by physical entrapment or covalent conjugation. Surface modification of hydrogel NPs, e.g. PEGylation and attachment with targeting ligands, is typically done via conjugation with amine or carboxyl groups onto the NP surface. The main mechanism for drug release from NPs is concentration-dependent diffusion, which is affected by loading of drugs in the NPs, the solubility of drugs in buffer in the solvent, and the properties of the NPs (e.g. composition, degree of cross-linking, surface charge).[43] The drug release can be adjusted to be responsive to temperature, pH or reducing agents, because of the swelling behavior of hydrogel NPs with various physical or chemical stimuli. Hydrogel NPs have been widely used as carriers for various kinds of drugs for chemotherapy [46] and photodynamic therapy, [47-49] as well as contrast agents for MRI imaging [47] and visible tumor delineation.[50] (Figure 1.1) In addition, hydrogel NPs may deliver multiple kinds of molecules together, aimed at combination of therapy and image-guided therapy.

#### **1.4.1 Hydrogel nanoparticles for chemotherapy**

A large fraction of the hydrogel NPs for cancer therapy has been focused on chemotherapy. Hydrogel NPs can improve the solubility, biodistribution and



accumulation to tumor tissue of chemotherapy drugs, thus improving their therapeutic performance. A nanoparticle formulation of paclitaxel (Genexol-PM) was approved for the treatment of breast and lung cancers in Korea.[51] Genexol-PM is based on a polymeric micelle, which is composed of copolymers of PEG and poly-(D,L-lactic acid). In addition, another kind of targeted hydrogel NPs containing docetaxel (BIND-014), has been tested in preclinical studies and in early phase clinical trials for metastatic lung cancer and tonsillar cancer.[52] BIND-014 was composed of PLGA/PEG and targeted to a prostate-specific membrane antigen (PSMA), which is expressed on prostate cancer cells and on blood vessel endothelial cells of many types of non-prostate solid tumors.

Polyacrylamide NPs were used for the delivery of cisplatin for vascular-targeted chemotherapy.[46] The NPs were conjugated with the tumor targeting peptide F3, which then binded to tumor blood vessel endothelial cells and to certain other kinds of tumor cells, via interaction with the nucleolin expressed on these cells' surfaces. Cisplatin, a common chemotherapy drug, was loaded into these NPs via physical absorption ("post loading"). The results showed that the F3 peptide enhanced the uptake of NPs by human ovarian tumor cells and tumor endothelial cells *in vitro*. In addition, the F3-NPs primarily bound to tumor endothelial cells *in vivo*. The cytotoxicity results showed that F3-Cis-NPs can cause, *in vivo*, tumor regression in both drug-sensitive and drug-resistant cell lines.

In addition, a pH-responsive polymer NP that expands in response to pH change was developed. One kind of monomer of this NP includes a 2, 4, 6-

trimethoxybenzaldehyde group, which is stable at pH 7.4, but can be hydrolyzed at pH 5. With this protecting group, this NP can be converted from hydrophobic (pH 7.4) to hydrophilic (pH 5), resulting in a size increase of the NPs, and thus enhanced drug release. Paclitaxel was loaded into this NP successfully. *In vivo* studies showed that paclitaxel-loaded NPs were more effective for the prevention of lung cancer, compared to the conventional paclitaxel delivery with Cremophor EL/ethanol.[53]

Hydrogel NPs have been shown to alleviate the drug resistance effect of cancer cells via various mechanisms.[24, 40] Polymeric micelles based on Pluronic P85 were reported to interact with P-glycoprotein (cell-surface protein pump), and induce cell membrane permeability.[54] One kind of polymer NPs composed of stearyl-modified dextran can bypass P-glycoprotein.[55] In addition, some types of NPs can carry both chemotherapy drugs and P-glycoprotein inhibitor (e.g. verapamil) into drug-resistant cells, which showed a synergistic effect of overcoming drug resistance.[56]

#### **1.4.2 Hydrogel nanoparticles for photodynamic therapy**

Photodynamic therapy (PDT) is a cancer treatment method that uses photo-drugs, which are photosensitizers (PS), along with light, to kill cancer cells. The photosensitizers react with oxygen and generates reactive oxygen species (ROS), in which singlet oxygen may be the dominant species during PDT. These ROS can interact with plasma membranes, mitochondria, golgi apparatuses, lysosomes, etc, leading to cell death via apoptosis, necrosis or autophagy.[57] The efficiency of photodynamic therapy depends on the photosensitizers' ability to produce ROS, the accumulation of the photosensitizers at the tumor tissue, the tissue oxygen

concentration and the administered light dose including intensity and duration.

Hydrogel NPs have been widely used for the delivery of photosensitizers. They can improve the photosensitizers solubility and avoid their aggregation, which would reduce their efficacy.[27] Photosensitizers can be loaded into hydrogel NPs by physical entrapment and by covalent conjugation. Since the efficiency of PDT relies on the generation and delivery of ROS, it is not necessary for the photosensitizers to be released out of the NP.[49] The advantages of physical entrapment include easy preparation, and also the release of drugs from the NPs, thus avoiding quenching of the singlet oxygen inside the NPs. Covalent conjugation can improve the loading of photosensitizers in the NPs and avoid leaching out of drugs to undesired areas, thus minimizing nonspecific damage to healthy tissue.

Polyacrylamide (PAA) NPs are the most widely studied hydrogel matrix for PDT. Several kinds of photosensitizers were loaded into PAA NPs successfully, including methylene blue [48, 49, 58], photophrin [47], meta-tetra(hydroxyphenyl)chlorin (mTHPC) [59] and 2-devinyl-2-(1-hexyloxyethyl) pyropheophorbide (HPPH) [45]. After attachment with tumor-targeting F3 peptide, the photosensitizer-loaded NPs showed effective cell killing both *in vitro* and *in vivo*. [47, 49]

In addition, aerosol OT (AOT)-alginate NPs were used as a carrier of doxorubicin (Dox) and methylene blue (MB) for a combination therapy, of chemotherapy and PDT.[60, 61] Both doxorubicin and MB were loaded into NPs via physical entrapment. The NP-mediated delivery enhanced the intracellular accumulation of Dox and MB significantly, and inhibited the tumor growth in JC tumors (mammary

adenocarcinoma, a drug-resistant mouse tumor model) in female Balb/c mice.

### **1.4.3 Hydrogel nanoparticles for cancer imaging**

Most contrast agents for cancer imaging are small molecules, which have low selectivity for the disease area and short circulation time in the plasma. The advantages of hydrogel NPs also benefit the delivery of contrast agents. Hydrogel NPs allow the long retention of contrast agents in the plasma and enhance their accumulation, thus improving the tumor specificity via the EPR effect and sensitivities of these imaging agents. Hydrogel NPs have been used for several kinds of cancer imaging, including magnetic resonance imaging (MRI), [47, 62, 63] positron emission tomography (PET), [64] and photoacoustic imaging [65]. For example, superparamagnetic iron oxide (SPIO) nanocrystals were embedded into PAA NPs for MRI imaging of 9L brain tumor *in vivo*. [47] In addition, the decoration with F3 peptide improved the contrast signal and retention time of the iron oxide-loaded NPs in the tumor area. [47] With high payloads of SPIO, these NPs showed much higher R2 and R2\* relaxivities (5 times) than other SPIOs. In addition, a tumor-targeted dye-loaded hydrogel NPs was developed successfully for intraoperative visual delineation of brain tumors. [50]

### **1.5 Organization of the dissertation**

This dissertation focused on the development of targeted hydrogel nanoplatfoms and their application to cancer therapy and imaging. Specifically, we explored the applications of hydrogel nanoplatfoms for (i) photodynamic therapy, (ii) overcoming

multidrug resistance and (iii) brain tumor delineation for surgery.

Chapter 2 described two novel kinds of methylene blue (MB)-conjugated polyacrylamide (PAA) nanoparticles, based on two separate MB derivatives, aimed at tumor-targeted photodynamic therapy. This covalent conjugation with the NPs (i) improves the loading of MB, (ii) prevents any leaching of MB from the NPs and (iii) protects the MB from the effects of enzymes in the biological environment. The loading of MB into these two kinds of NPs is controlled by the input amount, resulting in concentrations with optimal singlet oxygen production. For each of the MB-NPs, the highest singlet oxygen production was found for an MB loading of around  $11 \text{ nmol mg}^{-1}$ . The MB-NPs were modified with F3 peptide, which binds to angiogenic tumor vasculatures, and to certain kinds of tumor cells, via interaction with the nucleolin expressed on the cell's surface. After decoration with F3 peptide, each of these NPs was taken up, selectively, by MDA-MB-435 tumor cells, *in vitro*. PDT tests demonstrated that both kinds of targeted NPs resulted in effective tumor cell kill, following illumination, without any dark toxicity.

In Chapter 3, a highly engineerable hydrogel NP was developed as a carrier for the optimal co-delivery to tumor cells of a chemodrug, doxorubicin (Dox) and a chemosensitizer, verapamil (Vera), aiming at alleviating tumor MDR, as well as optimizing the drug's delivery and reducing its side effects. The hydrogel NPs were prepared via the copolymerization of acrylamide, 2-carboxyethyl acrylate (CEA) and 3-(acryloyloxy)-2-hydroxypropyl methacrylate. Dox and Vera were separately post-loaded into two different sets of NPs. We delivered both Dox-NPs and Vera-NPs into

the Dox-resistant NCI/ADR-RES cells. The codelivery seems to have overcome these cells' efflux pumps; it increased the intracellular accumulation of Dox, and significantly enhanced the cell killing ability of Dox. Overall, these findings suggest that such synergistic co-delivery, with hydrogel NPs, provides a promising route for overcoming tumor MDR and for minimizing toxicity, from either drug or sensitizer.

The therapeutic performance of drug-loaded NPs can be improved further with active targeting of the NPs. In chapter 4, a peptide-conjugated hydrogel nanoparticle was introduced, which is formed with a matrix based on a copolymer of acrylamide (AA) and 2-carboxyethyl acrylate (CEA), for the targeted delivery of DOX. The co(CEA-AA) NP is conjugated with a tumor-targeting peptide, F3. A copper (I) catalyzed "click reaction" was used for the attachment of an alkyne-functionalized F3 peptide to the azide-functionalized NPs. The F3 peptide dramatically improved the uptake of the co(CEA-AA) NPs by the nucleolin-overexpressing glioma cell line 9L, which is known to be related to nucleolin-mediated endocytosis.[66, 67] In addition, the uptake of F3-targeted NPs by 9L cells is much higher than their uptake by the breast cancer cell line MCF-7 (lower expression of nucleolin on surface). Notably, the F3 peptide also significantly enhanced the uptake of these NPs by the drug-resistant cell line NCI/ADR-RES. The attachment with F3 peptide does not affect the ability of these NPs to deliver doxorubicin. Dox-loaded F3-targeted NPs show a marginally better cell killing ability to 9L cells and NCI/ADR-RES cells *in vitro*, as compared to non-targeted Dox-loaded NPs.

Chapter 5 described the development of tumor-targeted, intensely blue colored NP

agents, based on coomassie blue-covalently linked PAA NPs, for brain tumor delineation. The coomassie blue (CB) derivative developed by Guochao Nie in our group, can be incorporated into PAA NPs via free radical polymerization. Such CB-linked NPs were prepared in a reverse microemulsion system. Compared to that of blank NPs, the synthesis procedure for CB-linked NPs was modified significantly so as to achieve sufficient dye loading, optimizing the ratio of surfactants, initiators and solvent for the monomer mixture solution. The NPs were also decorated with polyethylene glycol (PEG), to improve their stability in the blood plasma and to prevent nonspecific binding. The F3 peptide was also attached to the NPs, so as to maximize accumulation in the brain tumor tissues. An *in vivo* tumor staining experiment, in 9L-glioma bearing rats, showed that these F3-targeted, CB-linked NPs had a better contrast delineation effect, as well as a longer retention time in the tumor area, compared to nontargeted, CB-linked, PAA NPs.

Chapter 6 is a summary of the work included in this dissertation and also delineates future directions and applications for these multifunctional nanoplatfoms.

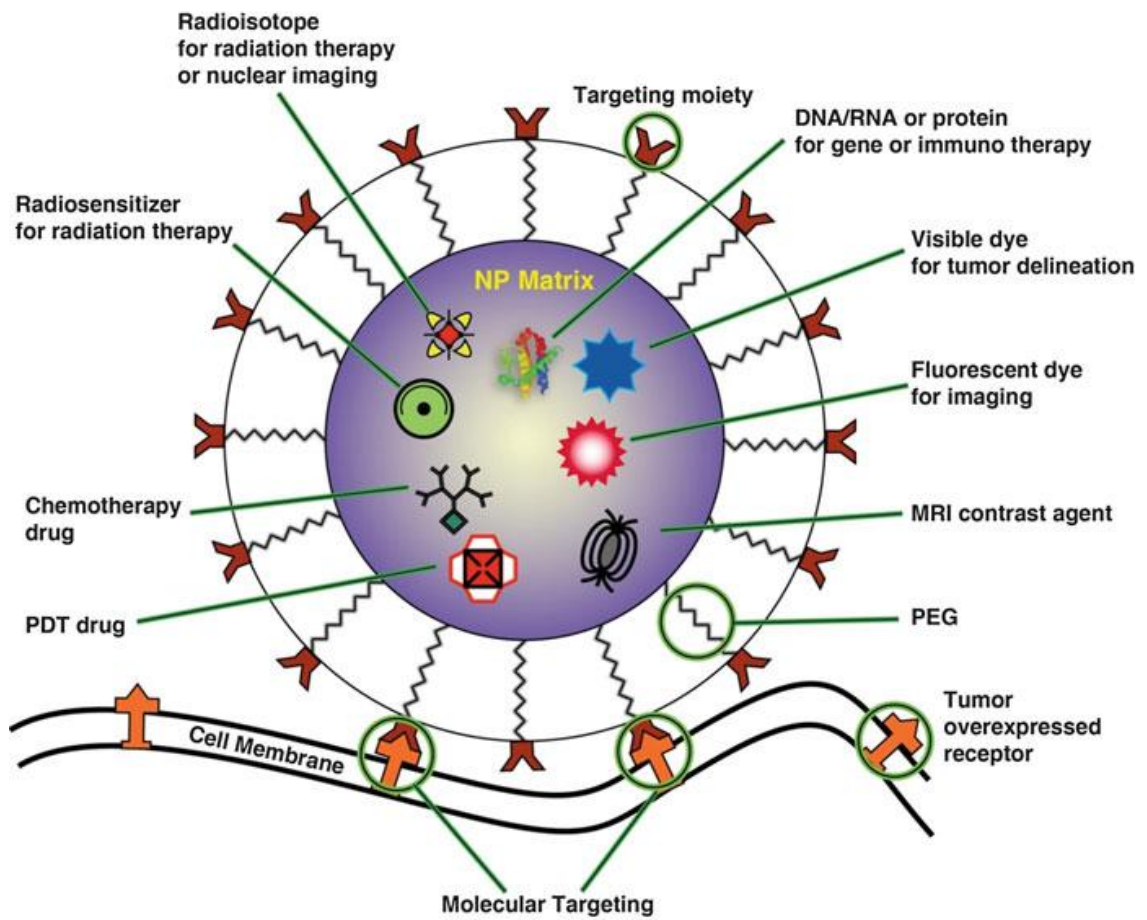


Figure 1.1 Schematic diagram of a targeted multifunctional nanoparticle with therapeutic and imaging options for cancer detection and therapy.[17]



## References

1. Cancer, I.A.f.R.o., *GLOBOCAN 2012*. 2012.
2. Society, A.C., *Cancer Facts & Figures 2013*, 2013.
3. Clark, W.H., *Tumour progression and the nature of cancer*. British Journal of Cancer, 1991. **64**(4): p. 14.
4. Jain, R.K., *Transport of molecules in the tumor interstitium: A review*. Cancer Research, 1987. **47**(12): p. 3039-3051.
5. Carmeliet, P. and R.K. Jain, *Angiogenesis in cancer and other diseases*. Nature, 2000. **407**(6801): p. 249-257.
6. Plank, M.J. and B.D. Sleeman, *Tumour-Induced Angiogenesis: A Review*. Journal of Theoretical Medicine, 2003. **5**(3-4): p. 137-153.
7. Jain, R.K., *Delivery of molecular medicine to solid tumors: Lessons from in vivo imaging of gene expression and function*. Journal of Controlled Release, 2001. **74**(1-3): p. 7-25.
8. Hobbs, S.K., et al., *Regulation of transport pathways in tumor vessels: Role of tumor type and microenvironment*. Proceedings of the National Academy of Sciences, 1998. **95**(8): p. 4607-4612.
9. Baban, D.F. and L.W. Seymour, *Control of tumour vascular permeability*. Advanced Drug Delivery Reviews, 1998. **34**(1): p. 109-119.
10. Iyer, A.K., et al., *Exploiting the enhanced permeability and retention effect for tumor targeting*. Drug Discovery Today, 2006. **11**(17-18): p. 812-818.
11. Jain, R.K. and T. Stylianopoulos, *Delivering nanomedicine to solid tumors*. Nature Reviews Clinical Oncology, 2010. **7**(11): p. 653-664.
12. Jang, S.H., et al., *Drug delivery and transport to solid tumors*. Pharmaceutical Research, 2003. **20**(9): p. 1337-1350.
13. Maeda, H., et al., *Tumor vascular permeability and the EPR effect in macromolecular therapeutics: a review*. Journal of Controlled Release, 2000. **65**(1-2): p. 271-284.
14. Maeda, H., G.Y. Bharate, and J. Daruwalla, *Polymeric drugs for efficient tumor-targeted drug delivery based on EPR-effect*. European Journal of Pharmaceutics and Biopharmaceutics, 2009. **71**(3): p. 409-419.
15. Maeda, H., *The enhanced permeability and retention (EPR) effect in tumor vasculature: The key role of tumor-selective macromolecular drug targeting*. Advances in Enzyme Regulation, Vol 41, 2001. **41**: p. 189-207.
16. Barreto, J.A., et al., *Nanomaterials: Applications in Cancer Imaging and Therapy*. Advanced Materials, 2011. **23**(12): p. H18-H40.
17. Lee, Y.-E.K. and R. Kopelman, *Targeted, Multifunctional Hydrogel Nanoparticles for Imaging and Treatment of Cancer: Multifunctional Nanoparticles for Drug Delivery Applications*, S. Svenson and R.K. Prud'homme, Editors. 2012, Springer US. p. 225-255.
18. Gerweck, L.E., S. Vijayappa, and S. Kozin, *Tumor pH controls the in vivo efficacy of weak acid and base chemotherapeutics*. Molecular Cancer Therapeutics, 2006. **5**(5): p. 1275-1279.
19. Allen, T.M. and P.R. Cullis, *Drug Delivery Systems: Entering the Mainstream*. Science, 2004. **303**(5665): p. 1818-1822.
20. Brown, R. and M. Links, *Clinical relevance of the molecular mechanisms of resistance to anti-cancer drugs*. Expert Reviews in Molecular Medicine, 1999. **1**(15): p. 1-21.
21. Krishna, R. and L.D. Mayer, *Multidrug resistance (MDR) in cancer Mechanisms, reversal using modulators of MDR and the role of MDR modulators in influencing the pharmacokinetics of anticancer drugs*. European Journal of Pharmaceutical Sciences, 2000. **11**(4): p. 265-283.
22. Davis, M.E., Z. Chen, and D.M. Shin, *Nanoparticle therapeutics: an emerging treatment modality for cancer*. Nature Reviews Drug Discovery, 2008. **7**(9): p. 771-782.
23. Petros, R.A. and J.M. DeSimone, *Strategies in the design of nanoparticles for therapeutic applications*. Nature Reviews Drug Discovery, 2010. **9**(8): p. 615-627.
24. Brigger, I., C. Dubernet, and P. Couvreur, *Nanoparticles in cancer therapy and diagnosis*. Advanced Drug Delivery Reviews, 2012. **64**, **Supplement**(0): p. 24-36.

25. Wang, A.Z., R. Langer, and O.C. Farokhzad, *Nanoparticle Delivery of Cancer Drugs*. Annual Review of Medicine, 2012. **63**(1): p. 185-198.
26. Chow, E.K.-H. and D. Ho, *Cancer Nanomedicine: From Drug Delivery to Imaging*. Science Translational Medicine, 2013. **5**(216): p. 216rv4.
27. Koo, Y.E.L., et al., *Brain cancer diagnosis and therapy with nanoplatforms*. Advanced Drug Delivery Reviews, 2006. **58**(14): p. 1556-1577.
28. Sparreboom, A., et al., *Comparative Preclinical and Clinical Pharmacokinetics of a Cremophor-Free, Nanoparticle Albumin-Bound Paclitaxel (ABI-007) and Paclitaxel Formulated in Cremophor (Taxol)*. Clinical Cancer Research, 2005. **11**(11): p. 4136-4143.
29. Miele, E., et al., *Albumin-bound formulation of paclitaxel (Abraxane (R) ABI-007) in the treatment of breast cancer*. International Journal of Nanomedicine, 2009. **4**(1): p. 99-105.
30. Tang, W., et al., *Photodynamic characterization and in vitro application of methylene blue-containing nanoparticle platforms*. Photochemistry and Photobiology, 2005. **81**(2): p. 242-249.
31. Alexis, F., et al., *Factors Affecting the Clearance and Biodistribution of Polymeric Nanoparticles*. Molecular Pharmaceutics, 2008. **5**(4): p. 505-515.
32. Zalipsky, S., *Chemistry of polyethylene glycol conjugates with biologically active molecules*. Advanced Drug Delivery Reviews, 1995. **16**(2-3): p. 157-182.
33. Owens Iii, D.E. and N.A. Peppas, *Opsonization, biodistribution, and pharmacokinetics of polymeric nanoparticles*. International Journal of Pharmaceutics, 2006. **307**(1): p. 93-102.
34. Knop, K., et al., *Poly(ethylene glycol) in Drug Delivery: Pros and Cons as Well as Potential Alternatives*. Angewandte Chemie International Edition, 2010. **49**(36): p. 6288-6308.
35. Xiao, K., et al., *"OA02" Peptide Facilitates the Precise Targeting of Paclitaxel-Loaded Micellar Nanoparticles to Ovarian Cancer In Vivo*. Cancer Research, 2012.
36. von Maltzahn, G., et al., *In Vivo Tumor Cell Targeting with "Click" Nanoparticles*. Bioconjugate Chemistry, 2008. **19**(8): p. 1570-1578.
37. Werner, M.E., et al., *Folate-Targeted Polymeric Nanoparticle Formulation of Docetaxel Is an Effective Molecularly Targeted Radiosensitizer with Efficacy Dependent on the Timing of Radiotherapy*. ACS Nano, 2011. **5**(11): p. 8990-8998.
38. Nie, G., et al., *Hydrogel Nanoparticles with Covalently Linked Coomassie Blue for Brain Tumor Delineation Visible to the Surgeon*. Small, 2012. **8**(6): p. 884-891.
39. Hu, Q., et al., *F3 peptide-functionalized PEG-PLA nanoparticles co-administrated with tLyp-1 peptide for anti-glioma drug delivery*. Biomaterials, 2013. **34**(4): p. 1135-1145.
40. Ma, P. and R.J. Mumper, *Anthracycline nano-delivery systems to overcome multiple drug resistance: A comprehensive review*. Nano Today, 2013. **8**(3): p. 313-331.
41. Yu, B., et al., *Receptor-targeted nanocarriers for therapeutic delivery to cancer*. Molecular Membrane Biology, 2010. **27**(7): p. 286-298.
42. Hong, S., et al., *The Binding Avidity of a Nanoparticle-Based Multivalent Targeted Drug Delivery Platform*. Chemistry & Biology, 2007. **14**(1): p. 107-115.
43. Kashyap, N., N. Kumar, and M.N.V.R. Kumar, *Hydrogels for Pharmaceutical and Biomedical Applications*. 2005. **22**(2): p. 107-150.
44. Drury, J.L. and D.J. Mooney, *Hydrogels for tissue engineering: scaffold design variables and applications*. Biomaterials, 2003. **24**(24): p. 4337-4351.
45. Wang, S., et al., *Multifunctional Biodegradable Polyacrylamide Nanocarriers for Cancer Theranostics—A "See and Treat" Strategy*. ACS Nano, 2012. **6**(8): p. 6843-6851.
46. Winer, I., et al., *F3-targeted cisplatin-hydrogel nanoparticles as an effective therapeutic that targets both murine and human ovarian tumor endothelial cells in vivo*. Cancer Research, 2010. **70**(21): p. 8674-8683.
47. Reddy, G.R., et al., *Vascular targeted nanoparticles for imaging and treatment of brain tumors*. Clinical Cancer Research, 2006. **12**(22): p. 6677-6686.
48. Tang, W., et al., *Encapsulation of methylene blue in polyacrylamide nanoparticle platforms protects its photodynamic effectiveness*. Biochemical and Biophysical Research Communications, 2008. **369**(2): p. 579-583.
49. Hah, H.J., et al., *Methylene Blue-Conjugated Hydrogel Nanoparticles and Tumor-Cell Targeted Photodynamic Therapy*. Macromolecular Bioscience, 2011. **11**(1): p. 90-99.

50. Orringer, D.A., et al., *In vitro characterization of a targeted, dye-loaded nanodevice for intraoperative tumor delineation*. Neurosurgery, 2009. **64**(5): p. 965-971.
51. Kim, T.Y., et al., *Phase I and pharmacokinetic study of Genexol-PM, a cremophor-free, polymeric micelle-formulated paclitaxel, in patients with advanced malignancies*. Clinical Cancer Research, 2004. **10**(11): p. 3708-3716.
52. Hrkach, J., et al., *Preclinical Development and Clinical Translation of a PSMA-Targeted Docetaxel Nanoparticle with a Differentiated Pharmacological Profile*. Science Translational Medicine, 2012. **4**(128): p. 128ra39.
53. Griset, A.P., et al., *Expansile Nanoparticles: Synthesis, Characterization, and in Vivo Efficacy of an Acid-Responsive Polymeric Drug Delivery System*. Journal of the American Chemical Society, 2009. **131**(7): p. 2469-2471.
54. Alakhov, V.Y., et al., *Hypersensitization of multidrug resistant human ovarian carcinoma cells by pluronic P85 block copolymer*. Bioconjugate Chemistry, 1996. **7**(2): p. 209-216.
55. Susa, M., et al., *Doxorubicin loaded Polymeric Nanoparticulate Delivery System to overcome drug resistance in osteosarcoma*. BMC Cancer, 2009. **9**.
56. Song, X.R., et al., *Reversion of multidrug resistance by co-encapsulation of vincristine and verapamil in PLGA nanoparticles*. European Journal of Pharmaceutical Sciences, 2009. **37**(3-4): p. 300-305.
57. Buytaert, E., M. Dewaele, and P. Agostinis, *Molecular effectors of multiple cell death pathways initiated by photodynamic therapy*. Biochimica Et Biophysica Acta-Reviews on Cancer, 2007. **1776**(1): p. 86-107.
58. Qin, M., et al., *Methylene blue covalently loaded polyacrylamide nanoparticles for enhanced tumor-targeted photodynamic therapy*. Photochemical & Photobiological Sciences, 2011. **10**(5): p. 832-841.
59. Gao, D., et al., *Ultrafine Hydrogel Nanoparticles: Synthetic Approach and Therapeutic Application in Living Cells*. Angewandte Chemie International Edition, 2007. **46**(13): p. 2224-2227.
60. Khdair, A., et al., *Nanoparticle-mediated combination chemotherapy and photodynamic therapy overcomes tumor drug resistance in vitro*. European Journal of Pharmaceutics and Biopharmaceutics, 2009. **71**(2): p. 214-222.
61. Khdair, A., et al., *Nano particle-mediated combination chemotherapy and photodynamic therapy overcomes tumor drug resistance*. Journal of Controlled Release, 2010. **141**(2): p. 137-144.
62. Ross, B., et al., *Photonic and magnetic nanoexplorers for biomedical use: from subcellular imaging to cancer diagnostics and therapy*. Proc. SPIE, 2004. **5331**: p. 76-83.
63. Kopelman, R., et al., *Multifunctional nanoparticle platforms for in vivo MRI enhancement and photodynamic therapy of a rat brain cancer*. Journal of Magnetism and Magnetic Materials, 2005. **293**(1): p. 404-410.
64. Sun, G., et al., *Strategies for Optimized Radiolabeling of Nanoparticles for in vivo PET Imaging*. Advanced Materials, 2007. **19**(20): p. 3157-3162.
65. Ray, A. and R. Kopelman, *Hydrogel nanosensors for biophotonic imaging of chemical analytes*. Nanomedicine, 2013. **8**(11): p. 1829-1838.
66. Porkka, K., et al., *A fragment of the HMGN2 protein homes to the nuclei of tumor cells and tumor endothelial cells in vivo*. Proceedings of the National Academy of Sciences, 2002. **99**(11): p. 7444-7449.
67. Christian, S., et al., *Nucleolin expressed at the cell surface is a marker of endothelial cells in angiogenic blood vessels*. Journal of Cell Biology, 2003. **163**(4): p. 871-878.

## **Chapter 2 Methylene Blue covalently loaded Polyacrylamide Nanoparticles for Enhanced Tumor-targeted Photodynamic Therapy**

Some of the material in this chapter has been adapted with minor modifications from the following publication:

Qin, M., Hah, H.J., Kim, G., Nie, G., Lee, Y.-E.K., Kopelman, R. et al., Methylene blue covalently loaded polyacrylamide nanoparticles for enhanced tumor-targeted photodynamic therapy. *Photochemical & Photobiological Sciences*, 2011. 10(5): p. 832-841.

### **Introduction**

Photodynamic therapy (PDT) is gaining increasing recognition as a medical treatment for cancer, especially skin cancer, and for other dermatological problems, such as acne, as well as for macular degeneration. This treatment uses PDT-drugs (called photosensitizers), in combination with light, to kill selected cells. It relies on the generation of singlet oxygen and other kinds of reactive oxygen species (ROS), causing cell death by apoptosis, necrosis and/or autophagy.[1] The first clinical PDT treatment was approved in the US in 1995.[2] Since then, PDT has been approved for the treatment of skin actinic keratosis, several forms of cancer, blindness due to age-related macular degeneration, etc.[3-5] PDT is a localized treatment, selectively activated by light, and thus causing low systemic toxicity. It can be applied by itself or in combination with other treatment methods, e.g., chemotherapy and surgery.[6]

An ideal photosensitizer for PDT should have a stable composition, photostability, minimum dark toxicity, high absorption in the red or near infrared region of the

spectrum, reasonable hydrophilicity, target specificity, and quick clearance from the body.[7] Many kinds of photosensitizers have been developed so far. However, very few of them satisfy those requirements. Methylene blue (MB), a hydrophilic phenothiazine derivative,[8-10] has been used as a drug in clinical applications for malaria and methemoglobinemia.[11, 12] MB has also been approved as a potent PDT drug for local treatment of periodontal diseases (Periowave, Canada), because of its relative low toxicity and high generation yield of singlet oxygen.[13, 14] MB exhibited phototoxicity towards a variety of tumor cell lines in vitro.[9, 15] Combined with illumination, MB was reported to cause 75% destruction of human colon tumor xenografts.[16] Also the local administration of MB intralesionally had some success with recurrent inoperable esophageal cancer in three patients.[17]

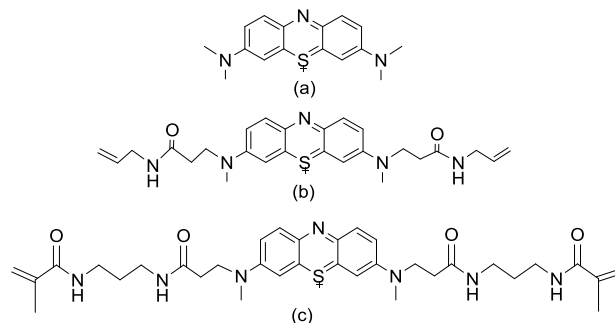
Some drawbacks of MB have limited its further clinical application as a PDT agent. The activity of MB became relatively low when injected intravenously or intravesically, which was attributed to poor tumor localization.[9, 13] In addition, the methylene blue photosensitizer is converted to its leuco- (colorless) isomer in the biological environment, a non-photosensitizer with negligible photodynamic activity.[18] This MB reduction is catalysed by either NADH/NADPH dehydrogenases within the cell or transmembrane thiazine dye reductase at the cell surface.[11, 19]

In order to improve the performance of photosensitizers, they should be targeted specifically to the tumor cells. This can be achieved by embedding them inside a nanoparticle (NP) and attaching a targeting group on the periphery of the particle,

e.g., antibodies or tumor-specific peptides. For instance, F3 peptide, a 31-amino acid peptide, is known to bind to the angiogenic tumor vasculatures, as well as to some tumor cells, by interacting with nucleolin, a cell surface receptor.[20, 21] The effect of enhanced permeability and retention (EPR) of NPs can also improve the local distribution of photosensitizers.[22] The nanoparticle matrix has to be porous to the outgoing singlet oxygen.[23] The design concept of NP-based PDT was first introduced in 2000 and the in vivo performance was demonstrated subsequently[24-28] We note that for drugs such as MB that can be inactivated by plasma enzymes,[23, 29-31] a protective carrier system is necessary, e.g., the nanoparticle matrix.[32] As a drug carrier, the advantages of NPs also include good solubility, high loading of drugs and alleviating the multidrug resistance effect of cancer cells.[31, 33]

The polyacrylamide (PAA) nanoparticle, due to its ideal size, biocompatibility and hydrophilicity, has been used for in vivo cancer imaging and treatment.[24-27] MB has been loaded in PAA NPs by encapsulation or by covalent linkage, exhibiting phototoxicity in a variety of cancer cell lines in vitro.[23, 32, 34-37] The encapsulation method resulted in low dye loading and the MB-encapsulated NPs required prolonged PDT illumination time or high dose for cell kill. Moreover, the encapsulated MB may leach out of the NPs. In our previous studies, MB was conjugated into PAA NPs via a two-step reaction (MBSE-PAA NPs).[37] This conjugation method prevented the drug leaching phenomena, increased significantly the loading of MB, and improved the singlet oxygen production of the NPs. The singlet oxygen production, which is a critical parameter of MB-conjugated PAA NPs

for PDT, is controlled largely by the structure of the MB derivative and by its loading into the NPs.[9] One question we were interested in about MB-PAA NPs is whether better singlet oxygen production of the NPs can be obtained by varying the MB derivatives and their loading into the NPs. Recently, two new kinds of MB derivatives (see Scheme 2.1 for their chemical structures), 3,7-bisallylmethylene blue (MBI) and 3,7-bismethylacrylamide methylene blue (MBII), were synthesized in our lab (The synthetic details will be reported separately). In the work reported here, MBI and MBII were conjugated into PAA NPs via a one-step reaction. For both MBI-PAA NPs and MBII-PAA NPs, the loading was controlled by the amount of MB derivatives that were added before polymerization. We report below the relationship between MB loading and singlet oxygen production for both kinds of MB-conjugated NPs, as well as the optimal singlet oxygen production. We compare the singlet oxygen production of MB-encapsulated NPs, MBSE-PAA NPs, MBI-PAA NPs and MBII-PAA NPs. We also show that this NP matrix protects the conjugated MB from the reduction by diaphorase (NADH dehydrogenase), while maintaining its photodynamic activity. The MBI-PAA NPs and MBII-PAA NPs were surface-conjugated with F3 peptide targeting groups for PDT specific to selected tumor cells.[37] The in vitro PDT experiments show that both kinds of NPs, when combined with illumination, are capable of killing MDA-MB-435 cancer cells effectively. We believe that our work reported here may further the application of MB for photodynamic therapy.



Scheme 2.1 Molecular structure of (a) methylene blue (MB), (b) 3, 7-bisallylmethylene blue (MBI), and (c) 3,7-bismethylacrylamide methylene blue (MBII).

## Experimental

### Materials

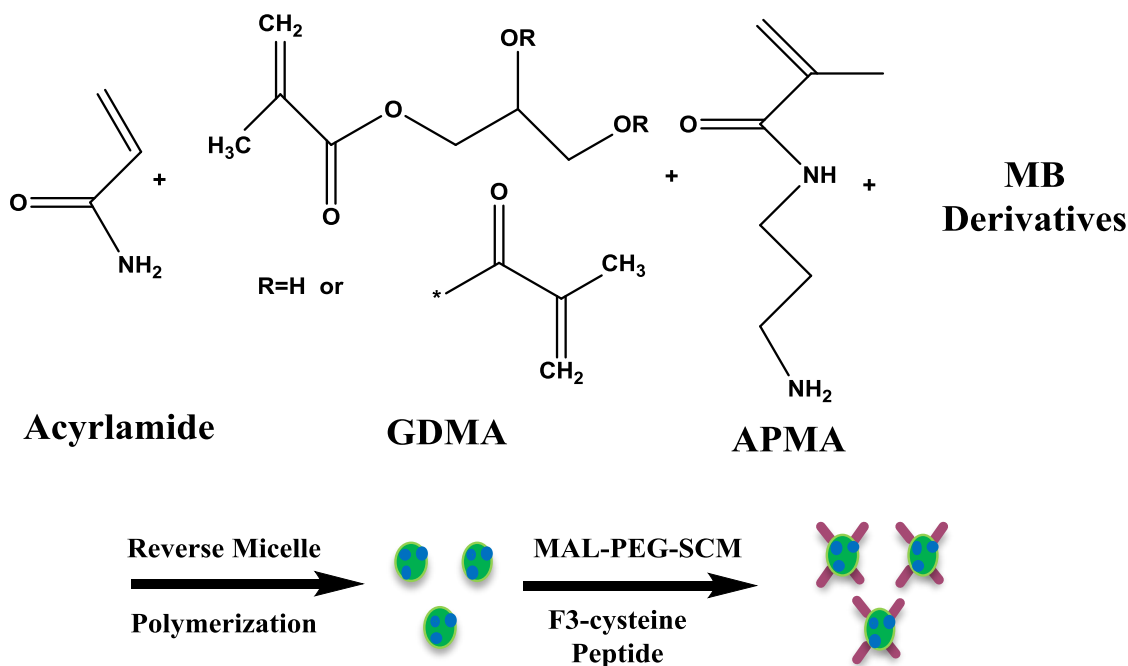
3,7-bisallylmethylene blue (MBI) and 3,7-bismethylacrylamide methylene blue (MBII) were synthesized in our lab. Acrylamide (AA), glycerol dimethacrylate (GDMA, 85%), ammonium persulfate (APS), N,N,N',N'-tetramethylethylenediamine (TEMED), sodium dioctyl sulfosuccinate (AOT), Brij 30, dimethylformamide (DMF), dimethylsulfoxide (DMSO), phosphate-buffered saline tablet (PBS),  $\beta$ -nicotinamide adenine dinucleotide, reduced dipotassium salt (NADH), diaphorase from *Clostridium Kluyveri* (NADH dehydrogenase) and 3-(4,5-dimethylthiazolyl-2)-2,5-diphenyltetrazolium bromide (MTT) were purchased from Sigma Aldrich. N-(3-Aminopropyl)methacrylamide hydrochloride (APMA) was purchased from Polysciences. Anthracene-9,10-dipropionic acid disodium salt (ADPA), calcein acetoxymethyl ester (calcein AM) and propidium iodide (PI) were purchased from Invitrogen. Ethanol (95%) and hexane were purchased from Fisher Scientific. F3-Cys peptide (KDEPQRRSARLSAKPAPPKPEPKPKKAPAKKC) was purchased from SynBioSci. The MAL-PEG-SCM (2K) (SCM: Succinimidyl Carboxy Methyl ester,



one type of NHS ester) was purchased from Creative PEGWorks. All the water used was purified with a Milli-Q system from Millipore.

### **Preparation of MB-conjugated PAA NPs**

MBI-PAA NPs and MBII-PAA NPs were synthesized with a reverse microemulsion polymerization method (in scheme 2.2). Deoxygenated hexane (45 mL), AOT (1.95 g) and Brij 30 (4.9 mL) were mixed together, and the mixture was stirred vigorously to produce a microemulsion. AA (610 mg), APMA (45 mg), GDMA (403 mg) and MBI or MBII were dissolved in DI water (1.2 mL) directly. The amount of MB added ranged from 10 mg to 90 mg, depending on the required loading of MB. The solution was sonicated until dissolved completely. Then the monomer solution was added into the hexane solution under argon atmosphere for 20 min. Fresh APS solution (200  $\mu$ L, 50% w/v) and TEMED (150  $\mu$ L) were added into the mixture solution to initiate polymerization. After 2 h reaction, hexane was removed by rotary evaporation. The residue was suspended in ethanol and transferred into an Amicon ultra-filtration cell (Millipore Corp.). In order to remove the surfactants and unreacted monomers, the NPs were washed with ethanol and DI water respectively with a 300 kDa filter membrane under the pressure of 15-20 psi. This washing process was repeated five times. After filtration with 0.2  $\mu$ m filter PTFE membrane (Whatman), the NPs were lyophilized and stored in freezer. The loading of MB in the NPs was controlled by the amount of MB added in.



Scheme 2.2 Preparation and F3-targeting of polyacrylamide nanoparticles

### Characterization

The loading of MB in the NPs was evaluated by taking absorption spectra of the MB-conjugated PAA NP suspensions in DI water ( $1 \text{ mg mL}^{-1}$ ) with a UV-1601 UV-vis spectrometer (Schimadzu). The fluorescence spectra of MB-conjugated NP suspension in PBS buffer ( $0.3 \text{ mg mL}^{-1}$ ) were taken with a FluoroMax-3 Spectrofluorometer (Jobin Yvon Horiba). Scanning electron microscopy (SEM) images of NPs were obtained with an FEI Nova Nanolab dualbeam focussed ion beam workstation and scanning electron microscope. The sample for SEM analysis was prepared as follows: 1) NP solution ( $0.1 \text{ mg mL}^{-1}$ ) was sonicated for 30 min to make sure the NPs were dispersed completely; 2) A drop of NP solution was placed on the SEM specimen mount and dried completely under room temperature; 3) Then the sample was coated with gold before SEM analysis. The size and zeta potential of NPs

in aqueous solution ( $1 \text{ mg mL}^{-1}$ ) were measured using dynamic light scattering (DLS) with a Delsa Nano (Beckman Coulter).

### **Dye leaching tests**

A MB-PAA NP solution ( $1 \text{ mL}$ ,  $1 \text{ mg mL}^{-1}$ ) was mixed with a bovine serum albumin (BSA) solution ( $1 \text{ mL}$ ,  $4 \%$ ). The mixture solution in PBS buffer ( $\text{pH } 7.4$ ) was stirred at  $37 \text{ }^\circ\text{C}$  for  $1.5 \text{ h}$ . After that, the solution was diluted to  $8 \text{ mL}$  in PBS buffer ( $\text{pH } 7.4$ ) and transferred to an Amicon ultra-filtration cell (Millipore Corp.). The solution was filtered with filter membrane ( $300 \text{ kDa}$ ) till the filtrate was  $5 \text{ mL}$ . Then a PBS buffer ( $5 \text{ mL}$ ,  $\text{pH } 7.4$ ) was added to the Amicon ultra-filtration cell and this filtering process was repeated for 3 times. The filtrates ( $5 \text{ mL}$ ) 1, 2 and 3 were collected respectively. The fluorescence emission intensity was measured with FluoroMax-3 Spectrofluorometer (Jobin Yvon Horiba).

### **F3 peptide attachment to MB-conjugated NPs**

MAL-PEG-SCM ( $4 \text{ mg}$ ) was added into a MB-conjugated PAA solution ( $2.5 \text{ mL}$ ,  $20 \text{ mg mL}^{-1}$ , PBS ( $\text{pH } 7.4$ )), and the solution was stirring for  $30 \text{ min}$  at room temperature. Then the NP solution was transferred to an Amicon centrifugal filter ( $100 \text{ kDa}$ ). The NP solution was rinsed with centrifugation at  $4000 \times g$  for  $20 \text{ min}$ . After 3 times washing, the NP solution was concentrated to be around  $20 \text{ mg mL}^{-1}$ , and mixed with an F3-Cys peptide solution ( $110 \text{ } \mu\text{L}$ ,  $100 \text{ mg mL}^{-1}$ ) under stirring. After stirring overnight, the NP solution was rinsed with centrifugation for 3 times and collected at  $20 \text{ mg mL}^{-1}$ . Then the NP solution was mixed with an L-cysteine

solution (63  $\mu\text{L}$ , 10  $\text{mg mL}^{-1}$ ). After 2 h reaction, the NP solution was washed with centrifugation for 3 times and collected at 20  $\text{mg mL}^{-1}$ . The amount of peptides conjugated on the NPs was determined by quantitative amino acid analysis (QAAA).

### **PEGylation of MB-conjugated NPs**

MAL-PEG-SCM (4 mg) was added into a MB-conjugated PAA solution (2.5 mL, 20  $\text{mg mL}^{-1}$ , PBS (pH 7.4)), and the solution was stirring for 30 min at room temperature. After that, the NP solution was transferred to an Amicon centrifugal filter (100 kDa). The NP solution was rinsed with centrifugation at 4000  $\times g$  for 20 min. After 3 times washing, the NP solution was concentrated to be around 20  $\text{mg mL}^{-1}$ , and mixed with an L-cysteine solution (125  $\mu\text{L}$ , 10  $\text{mg mL}^{-1}$ ). After 2 h reaction, the NP solution was washed with centrifugation for 3 times and collected at 20  $\text{mg mL}^{-1}$ .

### **Singlet oxygen detection**

The generation of singlet oxygen ( $^1\text{O}_2$ ) from MB-conjugated PAA NPs was determined by the ADPA method.[23, 38] An MB-conjugated PAA NP solution (2 mL) in PBS buffer (0.3  $\text{mg mL}^{-1}$ ) was mixed with an ADPA solution (80  $\mu\text{L}$ , 100  $\mu\text{M}$ ) in a 4 mL-cuvette. The solution was illuminated at 660 nm with a slit width of 10 nm with a 150 W ozone-free xenon-arc lamp. The actual power illuminated on the sample was around 2 mW. After illumination at different time scales (0, 1, 3, 5, 10, and 15 min), the fluorescence emission spectra of ADPA were collected under the excitation at 378 nm.

In this method, ADPA reacts with  $^1\text{O}_2$  and generates ADPA endoperoxide. The decay of [ADPA] follows first order kinetics if the rate of deactivation of  $^1\text{O}_2$  by reaction with ADPA is negligible compared to the deactivation by the solvent:[38]

$$\ln\left(\frac{[\text{ADPA}]_t}{[\text{ADPA}]_0}\right) = -kt \quad (1)$$

$$k = k_c [^1\text{O}_2] = \phi^{^1\text{O}_2} I^{\text{abs}} \frac{k_c}{k_d} \quad (2)$$

Where  $k_c$  is the rate constant of chemical quenching of  $^1\text{O}_2$  by ADPA, and  $k_d$  is the decay rate of  $^1\text{O}_2$  to  $^3\text{O}_2$  by energy transfer to the solvent or to other species in solution.  $\phi^{^1\text{O}_2}$  is the generation efficiency of  $^1\text{O}_2$  of a photosensitizer, and  $I^{\text{abs}}$  is the rate of photo absorption.

Here, the rate constant  $k$  is an indicator of singlet oxygen efficiency,  $\phi^{^1\text{O}_2}$ .

### **Enzymatic reduction test of MB**

The enzymatic reduction of MB was tested by the method reported before.[32] An aliquot of MB, MBI or MBII solution (3 mL, 3  $\mu\text{M}$ ) in PBS buffer (pH 7.4) was mixed with NADH (0.45  $\mu\text{mol}$ ) and diaphorase (0.05 mg). The fluorescence intensity of MB at 680 nm in the mixed solution was measured for 1 h with a FluoroMax-3 Spectrofluorometer (Jobin Yvon Horiba). The MBI-PAA NP or MBII-PAA NP solution (0.3 mg mL<sup>-1</sup>) was tested in the same way. As a control, the fluorescence intensity of these solutions without NADH and diaphorase was measured under the same condition for the photobleaching effect.

### **MTT assay**

The dark toxicity of MBI-PAA NPs and MBII-PAA NPs was analyzed, using an MTT assay, for the human melanoma cell line MDA-MB-435. The cells were incubated with MBI-PAA NPs or MBII-PAA NPs ( $0.2 \text{ mg mL}^{-1}$ ) on 96-well plates, containing 5000 cells in each well, for 1 hour before testing with the MTT assay. The cells were treated with an MTT reagent ( $0.5 \text{ mg mL}^{-1}$ ) for an additional 4 h. Then, the produced formazan crystals were solubilized in DMSO overnight. The visible absorption from each well was measured at 550 nm in a Biochrom Anthos microplate reader.

### ***In vitro* targeting and photodynamic tests**

The human melanoma cell line MDA-MB-435 was incubated with F3-targeted MB-PAA NPs (F3-MB-PAA NPs,  $0.1 \text{ mg mL}^{-1}$ ) or PEGylated MB-PAA NPs (PEG-MB-PAA NPs,  $0.1 \text{ mg mL}^{-1}$ ) for 15 min on the cover slips, cultivated in 6-well cover plates. Then the tumor cells were washed with cell culture media three times to remove the unbound NPs. The fluorescence images of the cells were taken using a 647 nm laser with  $400 \text{ }\mu\text{W}$  of power (exposure time: 0.2 s) and analyzed for cellular NP uptake by a Perkin Elmer Ultra View Confocal microscope system equipped with an argon-krypton laser. Calcein AM ( $0.4 \text{ }\mu\text{M}$ ) and PI ( $7 \text{ }\mu\text{M}$ ) were then added into cells and PDT was performed on cells with the same light source but with 1 min illumination (ca.  $100 \text{ J cm}^{-2}$ ). After 20 min, the fluorescence staining images of calcein AM and PI were taken. The excitation wavelength and emission wavelength of calcein AM are 488 nm and 525 nm, respectively, while the excitation wavelength and emission wavelength of PI are 568 nm and 600 nm, respectively.

## Results and discussion

### Preparation and characterization of MB-conjugated PAA NPs

Two critical elements for the successful preparation of NPs are the ratio of organic phase/water/surfactants and the amount of initiators. The first one is related with the formation of the nanodroplets in the continuous phase, while the second one is related with the polymerization inside these droplets. Compared to the preparation conditions of blank PAA NPs,[39] the following two modifications were made for the MB-conjugated PAA NPs: (a) Higher than typically used amounts of initiators (25 times of APS and 4 times of TEMED) are required for the preparation of MB-conjugated NPs. (b) In order to avoid aggregation of NPs, higher amounts of surfactants (2 times of AOT and 1.5 times of Brij 30) are necessary while the amount of hexane and water are kept the same as before. In this reaction, AA is the main monomer, GDMA is a biodegradable cross linker, and APMA provides the amine groups, which can be used for NP modification. High amounts of initiators may result from partial quenching of free radicals by the higher amounts of surfactants, as well as by the MBI and MBII.

The spectral characteristics and the MB loading of the NPs were determined by both UV-*vis* spectroscopy and fluorescence spectroscopy, seen in Figure 2.1(a) and 2.1(b). Compared to the absorption wavelength (652 nm) of the MBI solution, the absorption of MBI-PAA NPs is shifted to a longer wavelength (654 nm). Similarly, the absorption wavelength of MBII is also shifted from 654 nm in the MBII solution to 656 nm in the MBII-PAA NP solution. It should be noted that there is a noticeable peak at 610 nm in the absorption spectra of both MBI-PAA NPs and MBII-PAA NPs, in contrast

to the absorption spectra of MBI solution and MBII solution. The presence of the 610 nm peak indicates formation of MB dimers inside the NPs,[40-42] probably due to the relatively high concentration of MB within the NPs. MB dimers were also formed at high concentrations of MB in aqueous solution (where there is no conjugation).[40] It is interesting to see that MB dimers were formed even when the MB derivative was covalently conjugated inside the NPs. MB aggregates, other than dimers, are not likely to occur as MB is conjugated to the NP polymeric matrix. The MB loading in the NPs was estimated based on the peak area between 420-800 nm, using the Beer-Lambert law. The loading of MB is correlated well with the amount of MB added in. The MBI loading ranges from 6.4 nmol mg<sup>-1</sup> to 23.3 nmol mg<sup>-1</sup> in the 5 batches of MBI-PAA NPs; while, for MBII-PAA NPs, the MBII loading ranges from 5.5 nmol mg<sup>-1</sup> to 136.9 nmol mg<sup>-1</sup>.

The fluorescence excitation and emission spectra of the MBI and MBII-conjugated PAA NPs as well as MBI and MBII solutions are shown in Figure 2.1(b). The excitation and emission peak wavelengths of the MBI-PAA NPs are at 663 nm and 680 nm, respectively, which are the same as those of the MBI solution. The excitation and emission wavelengths of the MBII-PAA NPs were also the same as those of the MBII solution (662 nm and 680 nm). The fluorescence intensities of MBI-PAA NPs and MBII-PAA NPs were a little weaker than those of MBI and MBII in solution, under the same dye concentration, which is probably due to the formation of more MB dimers, or self-quenching of MB within the NPs.



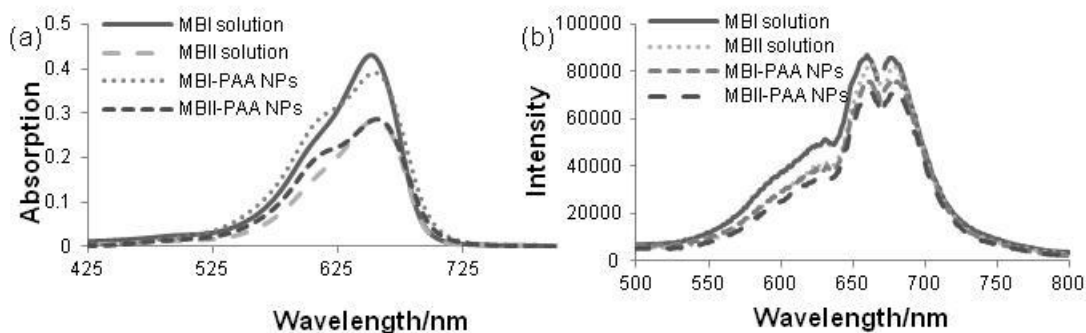


Figure 2.1 (a) UV-vis spectra of 1 mg mL<sup>-1</sup> MBI-PAA NP (MBI loading: 11.0 nmol mg<sup>-1</sup>), 1 mg mL<sup>-1</sup> MBII-PAA NP (MB loading: 10.4 nmol mg<sup>-1</sup>), 11.0 μM MBI and 10.4 μM MBII solutions, when dissolved in DI water. (b) Excitation and emission spectra of 0.3 mg mL<sup>-1</sup> MBI-PAA NP (MBI loading: 11.0 nmol mg<sup>-1</sup>), 0.3 mg mL<sup>-1</sup> MBII-PAA NP (MB loading: 10.4 nmol mg<sup>-1</sup>), 3.3 μM MBI and 3.1 μM MBII solutions, when dissolved in PBS buffer (pH 7.4).

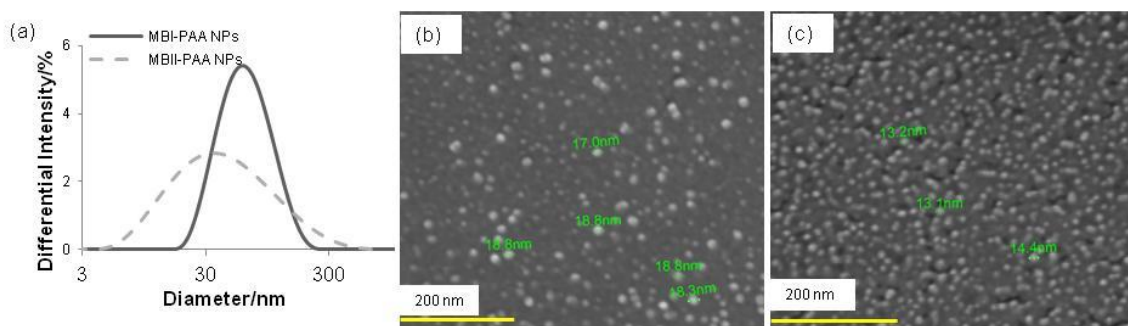


Figure 2.2 (a) DLS curves of MBI-PAA NPs (MBI loading: 6.4 nmol mg<sup>-1</sup>) and MBII-PAA NPs (MBII loading: 10.4 nmol mg<sup>-1</sup>); (b) SEM image of MBI-PAA NPs (MBI loading: 11.0 nmol mg<sup>-1</sup>) and (c) SEM image of MBII-PAA NPs (MBII loading: 10.4 nmol mg<sup>-1</sup>).

The formation and size of the NPs was tested by dynamic light scattering (DLS), as in Figure 2(a). The DLS data showed that the size of the MBI-PAA NPs in the aqueous solution increased from 57 to 112 nm when the loading of MBI increased from 6.4 nmol mg<sup>-1</sup> to 23.3 nmol mg<sup>-1</sup>. Similarly, for MBII-PAA NPs, the size of NPs ranged from 30 to 99 nm when the MB loading ranged from 5.5 nmol mg<sup>-1</sup> to 30.1 nmol mg<sup>-1</sup>. This phenomenon demonstrates that under similar preparation conditions, the size of the NPs is influenced by the amount of MB per NP. The morphology of the

MBI-PAA NPs (MBI loading:  $11.0 \text{ nmol mg}^{-1}$ ) and MBII-PAA NPs (MBII loading:  $10.4 \text{ nmol mg}^{-1}$ ) was also analyzed by SEM, seen in Figure 2.2(b) and 2.2(c). The average diameters of the MBI-PAA NPs and MBII-PAA NPs from SEM are 18.4 nm and 13.6 nm, respectively, compared to 74.4 nm of MBI-PAA NPs and 38.4 nm of MBII-PAA NPs in aqueous solution, respectively (from DLS). These results verified that the MB-PAA NPs in aqueous solution are larger than the size given by the SEM images, since hydrogel PAA NPs absorb water and swell in aqueous solution. Both MBI-PAA NPs and MBII-PAA NPs are very soluble in both DI water and PBS buffer, the solubility of which is around  $100 \text{ mg mL}^{-1}$  in PBS buffer. Additionally, these NPs were incubated with a BSA solution at  $37 \text{ }^\circ\text{C}$  for 1.5 h, in order to test the leaching of MB out of the NPs. The spectral results in Figure 2.3(a) and 2.3(b) show that no MB leached out from the NPs, which means that the covalent conjugation method practically prevents the PDT drug from leaching out of the NPs.

### **Singlet oxygen production efficiency**

The efficiency of photodynamic therapy relies on the  $^1\text{O}_2$  production, which is represented by the k value in equation (3). The k values of both MBI-PAA NPs and MBII-PAA NPs were tested by the ADPA method with the same NP concentration ( $0.3 \text{ mg mL}^{-1}$ ). Plotting the graph of  $\ln([\text{ADPA}]_t/[\text{ADPA}]_0)$  vs. time, the k value is the slope of the curve, seen in Figure 2.4.

We studied the relationship between the k value and the MB loading in both kinds of NPs, as shown in Figure 2.5. For MBI-PAA NPs, when the drug loading increased, starting from  $6.4 \text{ nmol mg}^{-1}$ , the k value increased gradually to a maximum when the

drug loading was about  $11.0 \text{ nmol mg}^{-1}$ ; then, when the drug loading continued to increase from  $11.0 \text{ nmol mg}^{-1}$  to  $23.3 \text{ nmol mg}^{-1}$ , the  $k$  value decreased. This means that the optimal  $^1\text{O}_2$  production from the MBI-PAA NPs was found at an MB loading of around  $11.0 \text{ nmol mg}^{-1}$ . The relationship between the  $k$  value and the drug loading of the MBII-PAA NPs showed a similar trend in which the  $k$  values increased with the MB loading up to  $10.4 \text{ nmol mg}^{-1}$  and then decreased. The highest  $k$  value for the MBII-PAA NPs was found for an MB loading of  $10.4 \text{ nmol mg}^{-1}$ . The phenomenon — a decrease of  $k$  values when the MB loading increases beyond an optimal loading — is most probably related to the dimerization of MB inside the NPs. As the MB loading increases, the ratio of MB dimers (absorption max at  $610 \text{ nm}$ ) to MB monomers (absorption max at  $655 \text{ nm}$ ), within the NPs, increases while the amount of MB monomer molecules per NP also increases (Figure 2.6(a)). The  $^1\text{O}_2$  production from the NPs relies on the amount of MB monomer molecules per NP. The  $k$  value of the MBII-PAA NPs appears to increase at a loading of  $30.1 \text{ nmol mg}^{-1}$ , compared to that at  $14.0 \text{ nmol mg}^{-1}$ , but this may not be significant due to the uncertainties (see error bars in Figure 2.5). If real, this trend might be due to a higher absolute amount of MB monomer molecules in the NPs with dye loading of  $30.1 \text{ nmol mg}^{-1}$  (this is hard to tell due to the significant spectral overlap of monomer and dimer absorption peaks — Figure 2.6(a)). We note that at the higher loading, the self-quenching of MB excited states must also increase (see relative increase in dimer absorption peak — Figure 2.6(a)), and therefore the  $^1\text{O}_2$  production at an MB loading of  $30.1 \text{ nmol mg}^{-1}$  is still less than that at  $10.4 \text{ nmol mg}^{-1}$ . The fluorescence intensity of MB, which also depends on the amount of MB monomer molecules per NP (Figure 2.6(b)), shows a

similar trend to that of the  $^1\text{O}_2$  production (k values in Figure 2.5), though, again, the fluorescence values for the 14.0 and 30.1  $\text{nmol mg}^{-1}$  loadings are the same, within the error bars (see Figure 2.6(b)).

We also compared the best k values for the MB-encapsulated PAA NPs, MBSE-PAA NPs, MBI-PAA NPs and MBII-PAA NPs (see Table 2.1). The MB-conjugated PAA NPs of all the preparations (MBSE-PAA NPs, MBI-PAA NPs and MBII-PAA NPs) resulted in better  $^1\text{O}_2$  production than the MB-encapsulated NPs, which is primarily related with the higher loading of MB in the conjugated NPs. The  $^1\text{O}_2$  production of MB-conjugated PAA NPs followed this order: MBI-PAA NPs > MBII-PAA NPs > MBSE-PAA NPs.

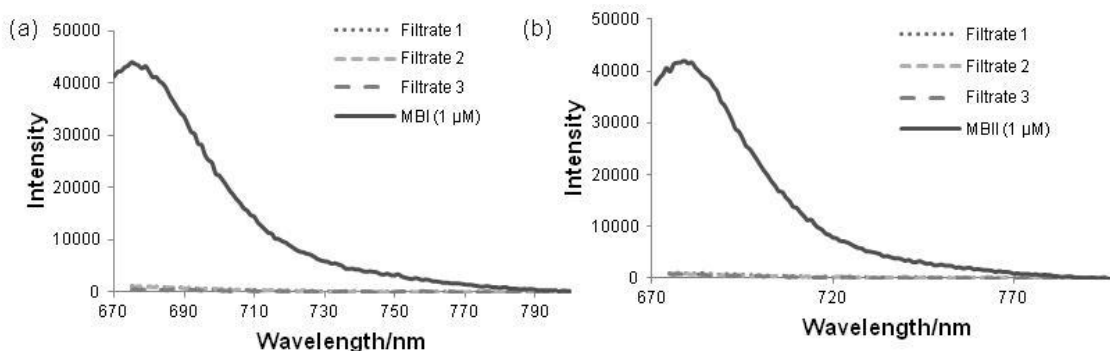


Figure 2.3 Fluorescence emission spectra of MB in the filtrates of (a) MBI-PAA NP solution (dye loading:  $13.8 \text{ nmol mg}^{-1}$ ) and (b) MBII-PAA NP solution (dye loading:  $12.9 \text{ nmol mg}^{-1}$ ) after dye leaching test, showing no measurable leaching of MB from the NPs.

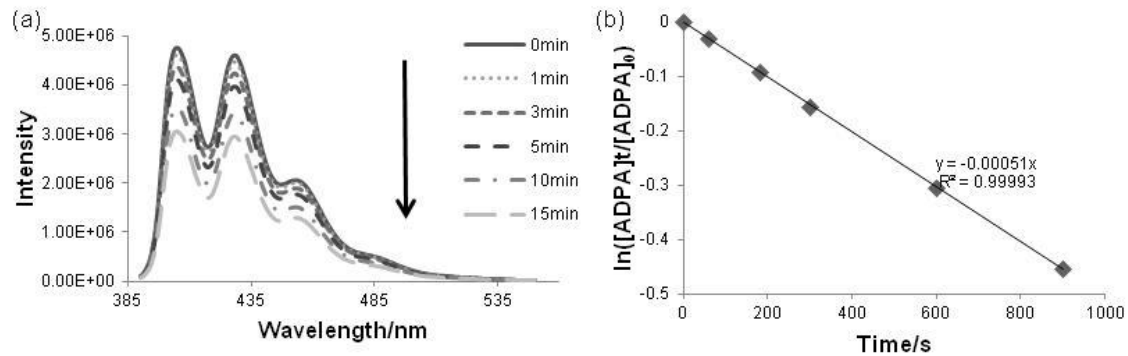


Figure 2.4 (a) Fluorescence spectra of ADPA in a mixed PBS buffer solution (pH 7.4) with  $0.3 \text{ mg mL}^{-1}$  MBII-PAA NP (MBII loading:  $10.4 \text{ nmol mg}^{-1}$ ) solution, after irradiation at 660 nm for 0, 1, 3, 5, 10, and 15 min. (b) Linear fit on the change of ADPA fluorescence intensity at 406 nm to irradiation time, showing the  $k$  value of MBII-PAA NPs (MBII loading:  $10.4 \text{ nmol mg}^{-1}$ ) was  $5.1 \times 10^{-4} \text{ s}^{-1}$ .

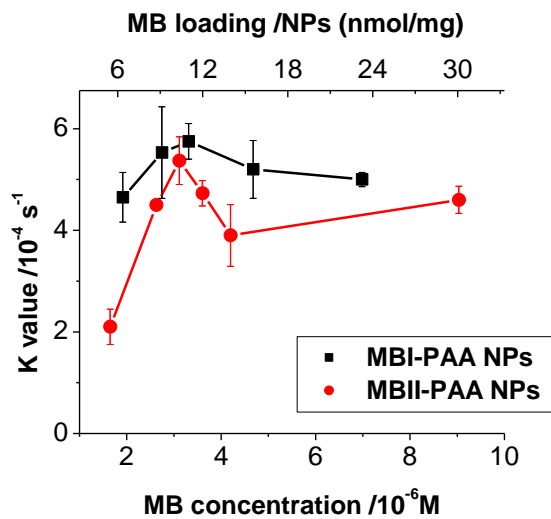


Figure 2.5  $k$  value vs. MB concentration and MB loading of the NPs in MBI-PAA NPs and MBII-PAA NPs solution ( $0.3 \text{ mg mL}^{-1}$  in PBS buffer)

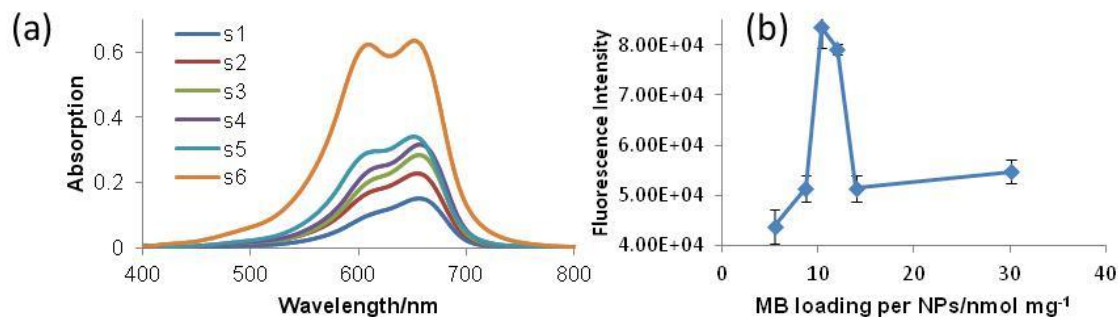


Figure 2.6 UV-*vis* spectra of MBII-PAA NPs ( $1 \text{ mg ml}^{-1}$  in DI water (a) and fluorescence intensity vs. MB loading in MBII-PAA NPs ( $0.3 \text{ mg ml}^{-1}$  in PBS buffer, excitation / emission:  $660 \text{ nm} / 680 \text{ nm}$ ) (b). S1 to S6 in (a) are MBII-PAA NPs with MB loading of  $5.5 \text{ nmol mg}^{-1}$ ,  $8.7 \text{ nmol mg}^{-1}$ ,  $10.4 \text{ nmol mg}^{-1}$ ,  $12.0 \text{ nmol mg}^{-1}$ ,  $14.0 \text{ nmol mg}^{-1}$  and  $30.1 \text{ nmol mg}^{-1}$  respectively.

### Enzymatic reduction of Methylene Blue

Our group reported earlier that the encapsulation of MB into PAA NPs prevented the interaction of MB with enzymes and thus effectively maintained its photodynamic activity.[32] In order to verify the hypothesis that the conjugation method can also largely prevent the MB from reduction by enzymes outside the NPs, the MB-PAA NP solution or MB solution was tested by the same method. When it was mixed with NADH and the diaphorase ( $24 \text{ kDa}$ ), the reduction of MB was confirmed by the decrease of fluorescence intensity of MB at  $680 \text{ nm}$  in both MB and MB-PAA NP solution. The temporal changes in the fluorescence emission intensity at  $680 \text{ nm}$  of the MB, MBI, MBII, MBI-PAA NP and MBII-PAA NP solutions are shown in Figure 2.7. Over 80% decrease of fluorescence intensity was found for MB, MBI and MBII solution in 1 h. However, only a 30 % and 50% decrease of fluorescence signal was found for MBI-PAA NP and MBII-PAA NP solutions, respectively. These results confirm that the PAA matrix helps, at least in part, to protect the dyes from the

biological environment and to retain their photodynamic activities. The reason for this protection may be that the diaphorase can not penetrate into the NPs because of its large molecular size. However, part of MB conjugated on the particle surface was reduced by diaphorase. That is why the decrease of fluorescence intensity was still found for the MB-PAA NPs solution.

Table 2.1 Best k values of MB-encapsulated NPs, MBSE-PAA NPs, MBI-PAA NPs and MBII-PAA NPs in PBS buffer (pH 7.4)

NPs	MB-encapsulated NPs [23]	MBSE-PAA NPs [37]	MBI-PAA NPs	MBII-PAA NPs
MB loading /NPs (nmol mg <sup>-1</sup> )	3.3	7.7	11.0	10.4
k value (10 <sup>-4</sup> s <sup>-1</sup> )	1.0±0.1	9.3±0.5	20.1±1.5	16.3±1.4

The k values above are for the NP solutions of 1 mg mL<sup>-1</sup>. The k values of MBI-PAA NPs and MBII-PAA NPs at 1 mg mL<sup>-1</sup> were converted from those at 0.3 mg mL<sup>-1</sup> using equation (2) and absorbance values of the NP solutions at 0.3 and 1 mg mL<sup>-1</sup>.

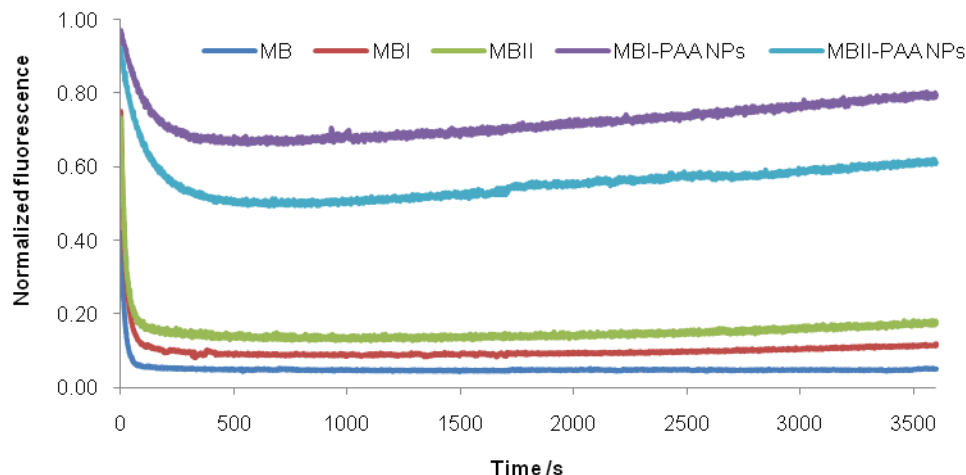


Figure 2.7 Enzymatic reduction test results: normalized fluorescence emission intensity at 680 nm of MB (3  $\mu$ M), MBI (3  $\mu$ M), MBII (3  $\mu$ M), MBI-PAA NP (0.3 mg mL<sup>-1</sup>, dye loading: 11.0 nmol mg<sup>-1</sup>) and MBII-PAA NP (0.3 mg mL<sup>-1</sup>, dye loading: 10.4 nmol mg<sup>-1</sup>) solutions. All samples were dissolved in PBS buffer (pH 7.4), and mixed with 0.45  $\mu$ mol NADH and 0.05 mg diaphorase. The photobleaching effect of MB was removed from all the curves.

## **PEGylation and F3 peptide attachment to MB-conjugated PAA NPs**

In our previous studies, the F3-conjugated PAA NPs were demonstrated to have efficient binding to, internalization into, and, as a result, enhanced therapeutic efficiency toward tumor cell lines that express high levels of nucleolin on their cell surface, e.g. the MDA-MB-435 breast cell line and the 9L glioma cell line, compared to tumor cell lines with low expression of nucleolin, e.g. the MCF-7 breast cancer cell line.[37, 43, 44] This targeting specificity was confirmed to depend on F3-nucleolin interactions, by comparing the targeting efficiency of NPs conjugated with F3 peptides and those of NPs with scrambled F3 peptides.[43] We have also shown that the F3-targeted PAA NPs can deliver efficiently diagnostic and/or therapeutic small molecules to glioma and ovarian tumor rodent models, enabling effective therapeutic outcomes.[28, 39]

In order to prepare NPs that selectively target specific tumor cells, the PAA NPs were modified by attachment of the F3 peptides via a cross linker, MAL-PEG-SCM. The SCM groups from MAL-PEG-SCM react with the amine groups on the NP surface and generate amide groups, while the MAL groups react with the thiol groups of the F3 peptides and generate carbon-sulfur bonds. PEG was reported to improve the hydrophilicity of NPs and increase the circulation time of NPs in the body.<sup>25</sup> [45] In order to test the targeting effect of F3-modified NPs, PEGylated NPs were used as a negative control. The QAAA results showed that the amount of F3 peptide attached on the NPs was 0.027  $\mu\text{mol}/(\text{mg NPs})$ .

The PEGylation and F3-peptide conjugation of the NPs were also monitored with



the zeta potential test. Before modification, the zeta potential of MBII-PAA NPs was ~15.4 mV, because of the positive amine groups on the surface; after PEGylation, since most of the NP surface was covered with neutral PEG, the zeta potential of the NPs was close to neutral (~1.8 mV); after reaction with the F3 peptide, the whole NP surface became positively charged again (~8.6 mV), which is related with the cationic nature of the F3 peptide.

### ***In vitro* targeting and PDT**

In order to verify the cell kill effects of the MB-conjugated NPs, *in vitro* PDT tests were performed on the MDA-MB-435 tumor cell line, which is known to express high levels of nucleolin. The NPs with MB loadings around 11 nmol mg<sup>-1</sup> were chosen for the *in vitro* PDT test because of their highest <sup>1</sup>O<sub>2</sub> production.

The uptake of MB-PAA NPs by tumor cells was monitored via the fluorescence images of tumor cells, based on the MB fluorescence under the confocal microscope (Fig. 8). The NPs were incubated with the cells for 15 min—the optimal incubation time for sufficient specific binding but minimal nonspecific binding.[43] It was observed that the F3-MB-NPs accumulated in the cell membrane and cytoplasm after 15 min incubation, while the PEG-modified MB-NPs did not. These results are consistent with previous results published by our group.[37, 44] Note that the light dose used for fluorescence imaging was not high enough to cause PDT effects on the cells—it was only 1/300 of the PDT dose (0.2 s vs. 1 min). The amount of F3-MB-NPs per cell was estimated to be ~ 6 x 10<sup>-8</sup> mg per cell, based on the previously reported saturated amount of NPs per cell and the current incubation condition that

corresponds to ~40% saturation.[43, 44]

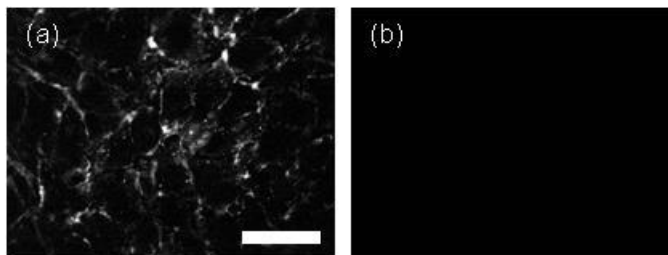


Figure 2.8 Confocal microscopy images of MDA-MB-435 cells after 15 min incubation with (a) F3-MBI-PAA NPs and (b) PEG-MBI-PAA NPs. NP concentration:  $0.3 \text{ mg mL}^{-1}$ ; dye loading:  $11.0 \text{ nmol mg}^{-1}$ ; scale bar:  $50 \text{ }\mu\text{m}$ .

The fluorescence images of the tumor cells treated with calcein AM and PI before and after PDT are shown in Fig. 9. Before illumination, both F3-MBI-NP-treated tumor cells and PEG-MBI-NP-treated tumor cells were alive (Figure 2.9(a) and 2.9(b)). At 20 min after a 1 min illumination, almost all F3-MBI-NP-treated tumor cells were dead, while the PEG-MBI-NP-treated tumor cells were still alive. In addition, the F3-MBI-NP-treated tumor cells were killed only in the area under illumination; in contrast, and as a control, the cells in the area with no illumination stayed alive, indicating that the NPs showed no dark toxicity after 15 min incubation (Figure 2.9). Analogous viability changes were also found for the PEG-MBII-NP-treated tumor cells and the F3-MBII-NP-treated cells. After only 1 min illumination, the F3-MBII-NPs killed the MDA-MB-435 tumor cells effectively, under illumination, but showed no cytotoxicity under dark conditions.

### **Dark toxicity of nanoparticles**

The dark toxicity effect of the MB-PAA NPs on the MDA-MB-435 cells was evaluated by an MTT assay, as shown in Figure 2.10. The cell viabilities were over

90% after incubation with MBI-PAA NPs ( $0.2 \text{ mg mL}^{-1}$ ) or MBII-PAA NPs ( $0.2 \text{ mg mL}^{-1}$ ) for 1 h, respectively. Both kinds of MB-PAA NPs showed no significant cytotoxicity when not under illumination.

## **Discussion and Conclusions**

Two novel variants of MB-conjugated PAA NPs were synthesized, enabling a high, non-leachable and an optimized photosensitizer loading for high  $^1\text{O}_2$  production. The prepared MB-conjugated PAA NPs showed significantly lower MB deactivation by enzymes, compared to their respective MB derivatives, giving an expectation of high *in vivo* PDT efficacy. The MB loading amount in these two kinds of NPs was controlled by the input amount, enabling optimization of  $^1\text{O}_2$  production. The best  $^1\text{O}_2$  production, for both MBI-NPs and MBII-NPs, was obtained with MB loadings around  $11 \text{ nmol mg}^{-1}$ . It was found that the highest  $^1\text{O}_2$  production of the NPs followed the order of MBI-PAA NPs > MBII-PAA NPs > MBSE-PAA NPs > MB-encapsulated PAA NPs. Both MBI-NPs and MBII-NPs were modified by attaching the tumor-targeting ligand, F3 peptide. *In vitro* PDT data showed that both kinds of targeted NPs, F3-MBI-PAA-NPs and F3-MBII-PAA-NPs, killed tumor cells effectively, with only 1 min illumination, in contrast to the same NPs with no F3. None of the NPs, targeted and untargeted, showed dark toxicity. We believe that our current work will contribute towards further applications of MB in photodynamic therapy.

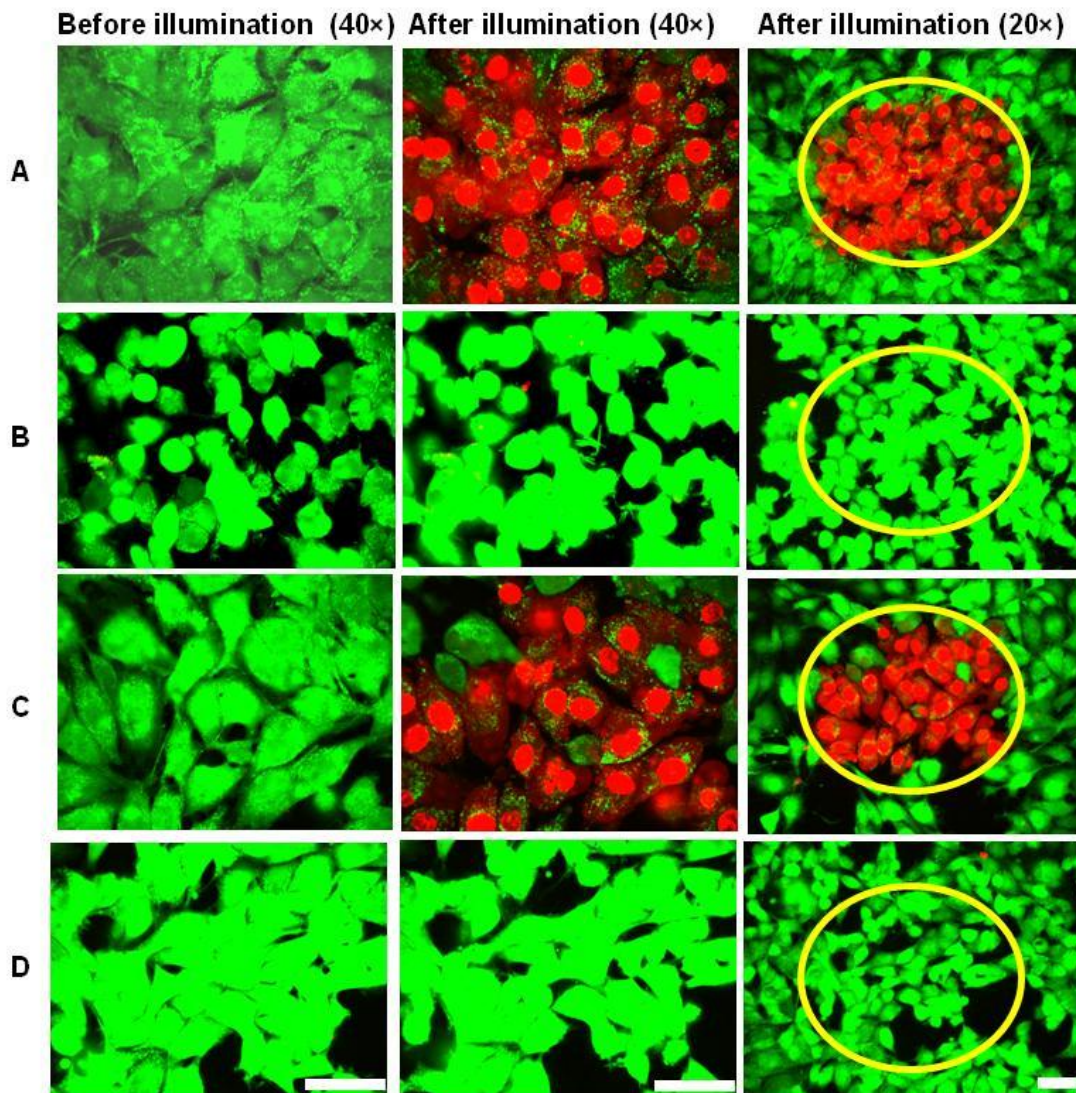


Figure 2.9 Confocal microscopy images of MDA-MB-435 cells stained with calcein-AM (green, living cell) and PI (red, dead cell), using a 20 $\times$  or 40 $\times$  objective lens, respectively. The cells were incubated with F3-targeted or PEGylated NP solution ( $0.1 \text{ mg mL}^{-1}$  in PBS buffer (pH 7.4)) for 15 min, respectively: (a) F3-MBI-PAA NPs; (b) PEG-MBI-PAA NPs; (c) F3-MBII-PAA NPs; (d) PEG-MBII-PAA NPs. After incubation, the cells were illuminated at 647 nm with 400  $\mu\text{W}$  of power (ca.  $100 \text{ J cm}^{-2}$ ) for 1 min. These images were taken before illumination and 20 min after illumination. In the images after illumination (20 $\times$ ), only the cells in the circled central area were illuminated. Scale bar: 50  $\mu\text{m}$

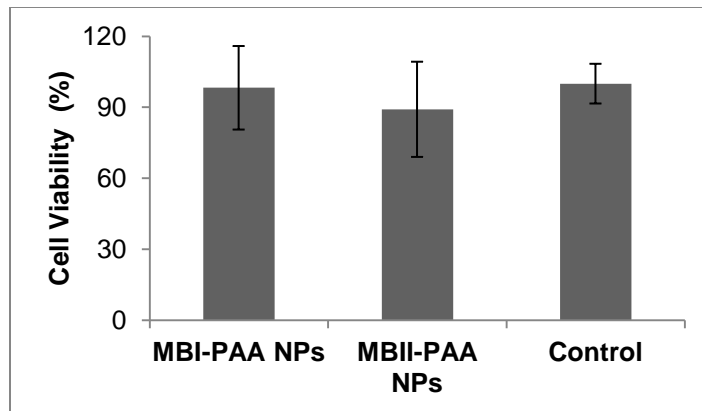


Figure 2.10 The viability of MDA-MB-435 cells from MTT assay, after incubation for 1 h with  $0.2 \text{ mg mL}^{-1}$  MBI-PAA NP solution (Dye loading:  $11.0 \text{ nmol mg}^{-1}$ ) and  $0.2 \text{ mg mL}^{-1}$  MBII-PAA NP solution (Dye loading:  $10.4 \text{ nmol mg}^{-1}$ ), respectively. These results showed the dark toxicity of MBI-PAA NPs and MBII-PAA NPs. The average value was obtained from 7 samples. Error bars indicate the standard deviation.

## **Acknowledgements**

This work was supported by grants R01 EB007977 and R01 EB007977-02s1 (RK) and, in part, by R33CA119358 and R33CA119358-03s1 (RK). We acknowledge the staff of the Electron Microscopy Analysis Laboratory at the University of Michigan.

## References

1. Buytaert, E., M. Dewaele, and P. Agostinis, *Molecular effectors of multiple cell death pathways initiated by photodynamic therapy*. *Biochimica Et Biophysica Acta-Reviews on Cancer*, 2007. **1776**(1): p. 86-107.
2. Siegel, M.M., et al., *Comparative mass spectrometric analyses of photofrin oligomers by fast atom bombardment mass spectrometry, UV and IR matrix-assisted laser desorption ionization mass spectrometry, electrospray ionization mass spectrometry and laser desorption/jet-cooling photoionization mass spectrometry*. *Journal of Mass Spectrometry*, 1999. **34**(6): p. 661-669.
3. Dolmans, D.E.J.G.J., D. Fukumura, and R.K. Jain, *Photodynamic therapy for cancer*. *Nature Reviews Cancer*, 2003. **3**(5): p. 380-387.
4. Brown, S.B., E.A. Brown, and I. Walker, *The present and future role of photodynamic therapy in cancer treatment*. *Lancet Oncology*, 2004. **5**(8): p. 497-508.
5. Wilson, B.C. and M.S. Patterson, *The physics, biophysics and technology of photodynamic therapy*. *Physics in Medicine and Biology*, 2008. **53**(9): p. R61-R109.
6. Juarranz, A., et al., *Photodynamic therapy of cancer. Basic principles and applications*. *Clinical & Translational Oncology*, 2008. **10**(3): p. 148-154.
7. Bechet, D., et al., *Nanoparticles as vehicles for delivery of photodynamic therapy agents*. *Trends in Biotechnology*, 2008. **26**(11): p. 612-621.
8. Trindade, G.S., et al., *Methylene blue reverts multidrug resistance: sensitivity of multidrug resistant cells to this dye and its photodynamic action*. *Cancer Letters*, 2000. **151**(2): p. 161-167.
9. Mellish, K.J., et al., *In vitro photodynamic activity of a series of methylene blue analogues*. *Photochemistry and Photobiology*, 2002. **75**(4): p. 392-397.
10. Gabrielli, D., et al., *Binding, aggregation and photochemical properties of methylene blue in mitochondrial suspensions*. *Photochemistry and Photobiology*, 2004. **79**(3): p. 227-232.
11. Bongard, R.D., et al., *Reduction of Thiazine Dyes by Bovine Pulmonary Arterial Endothelial-Cells in Culture*. *American Journal of Physiology-Lung Cellular and Molecular Physiology*, 1995. **13**(1): p. L78-L84.
12. Umbreit, J., *Methemoglobin—It's not just blue: A concise review*. *American Journal of Hematology*, 2007. **82**(2): p. 134-144.
13. Wainwright, M., *Non-porphyrin photosensitizers in biomedicine*. *Chemical Society Reviews*, 1996. **25**(5): p. 351-359.
14. Sharman, W.M., C.M. Allen, and J.E. van Lier, *Photodynamic therapeutics: basic principles and clinical applications*. *Drug Discovery Today*, 1999. **4**(11): p. 507-517.
15. Tuite, E.M. and J.M. Kelly, *Photochemical Interactions of Methylene-Blue and Analogs with DNA and Other Biological Substrates*. *Journal of Photochemistry and Photobiology B-Biology*, 1993. **21**(2-3): p. 103-124.
16. Orth, K., et al., *Photochemotherapy of experimental colonic tumours with intra-tumorally applied methylene blue*. *Langenbecks Archives of Surgery*, 1998. **383**(3-4): p. 276-281.
17. Orth, K., et al., *Intraluminal treatment of inoperable oesophageal tumours by intralesional photodynamic therapy with methylene blue*. *The Lancet*, 1995. **345**(8948): p. 519-520.
18. Orth, K., et al., *Methylene blue mediated photodynamic therapy in experimental colorectal tumors in mice*. *Journal of Photochemistry and Photobiology B-Biology*, 2000. **57**(2-3): p. 186-192.
19. May, J.M., Z.C. Qu, and C.E. Cobb, *Reduction and uptake of methylene blue by human erythrocytes*. *American Journal of Physiology-Cell Physiology*, 2004. **286**(6): p. C1390-C1398.
20. Porkka, K., et al., *A fragment of the HMGN2 protein homes to the nuclei of tumor cells and tumor endothelial cells in vivo*. *Proceedings of the National Academy of Sciences of the United States of America*, 2002. **99**(11): p. 7444-7449.
21. Christian, S., et al., *Nucleolin expressed at the cell surface is a marker of endothelial cells in angiogenic blood vessels*. *Journal of Cell Biology*, 2003. **163**(4): p. 871-878.
22. Maeda, H., *The enhanced permeability and retention (EPR) effect in tumor vasculature: The key role of tumor-selective macromolecular drug targeting*. *Advances in Enzyme Regulation*, Vol 41, 2001. **41**: p. 189-207.

23. Tang, W., et al., *Photodynamic characterization and in vitro application of methylene blue-containing nanoparticle platforms*. Photochemistry and Photobiology, 2005. **81**(2): p. 242-249.
24. Harrel, J.A. and R. Kopelman, *Biocompatible probes measure intracellular activity*. Biophotonics Int., 2000. **7**: p. 22-24.
25. Xu, H., et al., *Photoexcitation-based nano-explorers: Chemical analysis inside live cells and photodynamic therapy*. Israel Journal of Chemistry, 2004. **44**(1-3): p. 317-337.
26. Ross, B., et al., *Photonic and magnetic nanoexplorers for biomedical use: from subcellular imaging to cancer diagnostics and therapy*. Proc. SPIE, 2004. **5331**: p. 76-83.
27. Kopelman, R., et al., *Multifunctional nanoparticle platforms for in vivo MRI enhancement and photodynamic therapy of a rat brain cancer*. Journal of Magnetism and Magnetic Materials, 2005. **293**(1): p. 404-410.
28. Reddy, G.R., et al., *Vascular targeted nanoparticles for imaging and treatment of brain tumors*. Clinical Cancer Research, 2006. **12**(22): p. 6677-6686.
29. Koo, Y.E.L., et al., *Brain cancer diagnosis and therapy with nanoplatforms*. Advanced Drug Delivery Reviews, 2006. **58**(14): p. 1556-1577.
30. Peer, D., et al., *Nanocarriers as an emerging platform for cancer therapy*. Nature Nanotechnology, 2007. **2**(12): p. 751-760.
31. Davis, M.E., Z. Chen, and D.M. Shin, *Nanoparticle therapeutics: an emerging treatment modality for cancer*. Nature Reviews Drug Discovery, 2008. **7**(9): p. 771-782.
32. Tang, W., et al., *Encapsulation of methylene blue in polyacrylamide nanoparticle platforms protects its photodynamic effectiveness*. Biochemical and Biophysical Research Communications, 2008. **369**(2): p. 579-583.
33. Susa, M., et al., *Doxorubicin loaded Polymeric Nanoparticulate Delivery System to overcome drug resistance in osteosarcoma*. BMC Cancer, 2009. **9**: p. 399.
34. Chavanpatil, M.D., et al., *Polymer-surfactant nanoparticles for sustained release of water-soluble drugs*. Journal of Pharmaceutical Sciences, 2007. **96**(12): p. 3379-3389.
35. Khdair, A., et al., *Surfactant-polymer nanoparticles enhance the effectiveness of anticancer photodynamic therapy*. Molecular Pharmaceutics, 2008. **5**(5): p. 795-807.
36. Khdair, A., et al., *Nanoparticle-mediated combination chemotherapy and photodynamic therapy overcomes tumor drug resistance in vitro*. European Journal of Pharmaceutics and Biopharmaceutics, 2009. **71**(2): p. 214-222.
37. Hah, H.J., et al., *Methylene Blue-Conjugated Hydrogel Nanoparticles and Tumor-Cell Targeted Photodynamic Therapy*. Macromolecular Bioscience, 2011. **11**(1): p. 90-99.
38. Moreno, M.J., et al., *Production of singlet oxygen by Ru(dpp(SO<sub>3</sub>)(2))(3) incorporated in polyacrylamide PEBBLES*. Sensors and Actuators B-Chemical, 2003. **90**(1-3): p. 82-89.
39. Winer, I., et al., *F3-targeted cisplatin-hydrogel nanoparticles as an effective therapeutic that targets both murine and human ovarian tumor endothelial cells in vivo*. Cancer Research, 2010. **70**(21): p. 8674-8683.
40. Carroll, M.K., et al., *Interactions between methylene blue and sodium dodecyl sulfate in aqueous solution studied by molecular spectroscopy*. Applied Spectroscopy, 1999. **53**(7): p. 780-784.
41. Patil, K., R. Pawar, and P. Talap, *Self-aggregation of Methylene Blue in aqueous medium and aqueous solutions of Bu<sub>4</sub>NBr and urea*. Physical Chemistry Chemical Physics, 2000. **2**(19): p. 4313-4317.
42. Ghanadzadeh, A., et al., *Concentration effect on the absorption spectra of oxazine I and methylene blue in aqueous and alcoholic solutions*. Journal of Molecular Liquids, 2008. **138**(1-3): p. 100-106.
43. Orringer, D.A., et al., *In vitro characterization of a targeted, dye-loaded nanodevice for intraoperative tumor delineation*. Neurosurgery, 2009. **64**(5): p. 965-971.
44. Lee, Y.E.K., et al., *Near infrared luminescent oxygen nanosensors with nanoparticle matrix tailored sensitivity*. Analytical Chemistry, 2010. **82**(20): p. 8446-8455.
45. van Vlerken, L.E., T.K. Vyas, and M.M. Amiji, *Poly(ethylene glycol)-modified nanocarriers for tumor-targeted and intracellular delivery*. Pharmaceutical Research, 2007. **24**(8): p. 1405-1414.



## **Chapter 3 Overcoming Cancer Multidrug Resistance by Codelivery of Doxorubicin and Verapamil with Hydrogel Nanoparticles**

Some of the material in this chapter has been adapted with minor modifications from the following publication:

Qin, M.; Lee, Y.-E. K.; Ray, A.; Kopelman, R., Overcoming Cancer Multidrug Resistance by Codelivery of Doxorubicin and Verapamil with Hydrogel Nanoparticles. *Macromolecular Bioscience* 2014, accepted for publication.

### **Introduction**

Chemotherapy is one of the main cancer treatment methods. However, its efficacy is often inhibited by multidrug resistance (MDR), a major factor behind aggressive and untreatable disease patterns. MDR is classically defined as a universal state of resilience, against a multiplicity of drugs, including structurally and/or functionally unrelated drugs.[1] The most characterized mechanism of MDR is the drug efflux pump that uses up-regulation of ATP-Binding Cassette (ABC) transporters, e.g. P-glycoprotein (P-gp).[2] Many chemotherapy drugs, including doxorubicin (Dox), encounter drug resistance. While the drug efflux pump effect can be overcome by increasing the dose, and thus the concentration of the drug, this may result in unacceptable toxicity. A chemosensitizer, e.g. verapamil (Vera), can block the pathway of a drug efflux pump and thus increase the *local* concentration of the drug in the MDR tumor cell, thereby improving the therapeutic efficacy of the drug. The

combination of a chemotherapy drug and a chemosensitizer has been found to be a good option for the treatment of MDR.[2] However, previous clinical trials of chemosensitizers were not quite successful. The dosing and scheduling adjustment is challenging because of varying pharmacokinetics, biodistribution and membrane transport considerations.[3] While the sensitizer enables a reduction in dose, and potential toxicity of the chemodrug, serious side effects may also arise from the use of the chemosensitizing drug; for example, a high dose of verapamil may cause serious cardiotoxicity.[4]

Nano-drug delivery systems (nano-DDS) can prolong the systematic circulation time of drugs, enhance their accumulation in the diseased area, due to multivalent targeting and the enhanced permeability and retention (EPR) effect, as well as control of the drug release kinetics, thereby reducing the needed dose, and thus reducing the drug's side effects and enhancing the therapeutic factor.[5, 6] Nano-DDS have indeed been shown to alleviate the MDR effect of cancer cells.[7-10] Nano-DDS may also minimize toxicity due to size-based exclusion from certain organs.[11]

Several recent investigations have explored the codelivery of chemotherapy drugs and chemosensitizers with the aid of various nano-DDS, including liposomes,[12-14] solid-lipid nanoparticles,[15] micelles[16] and polymeric nanoparticles[17, 18]. For example, transferrin (Tf)-conjugated liposomes (Tf-Lip) were used for the codelivery of Dox and Vera. Cell viability tests on Dox-resistant K562 cells, treated with Dox-Vera-Tf-Liposomes, showed 5.2 and 2.8 times greater cytotoxicity ( $IC_{50} = 4.18 \mu M$ ), compared to non-targeted Dox-Vera-liposomes ( $IC_{50} = 21.7 \mu M$ ) and Dox-

Tf-Liposome ( $IC_{50} = 11.5 \mu\text{M}$ ), respectively.[13] Another study reported the successful encapsulation of Dox and Vera into stealth liposomes. The cytotoxicity tests on MLLB2 rat prostate cancer cells showed that the  $IC_{50}$  of Dox-Vera-Liposomes is, respectively, 13 times below that of Dox-liposome + Vera, and 2 times below that of Dox + Vera.[12]

One rational guiding this work is that of dosing simplicity, i.e. it is easier to change the mix (ratio) of two stock NPs, one containing the drug and the other the sensitizer only, compared to producing a series of NPs loaded with a varying ratio of drug/sensitizer. Another is the use of hydrogel NPs, especially polyacrylamide nanoparticles (PAA NPs), which have emerged as an important drug delivery vehicle for cancer imaging and therapy. PAA NPs combine the advantages of hydrogel biocompatibility and the hydrogel NP's engineerability and flexibility, and have enabled multifunctionality, e.g. theranostic treatment, controlled release kinetics, stealth circulation and biodegradability.[5, 19-21] Notably, this biomaterial, polyacrylamide, has been widely used clinically, e.g. it has been used as permanent filler (Aquamid) for facial soft-tissue augmentation for about 20 years.[22] These PAA NPs are highly soluble in water, and have been made controllably biodegradable;[23] they can carry high payloads of drugs and also protect such drugs from interference by enzymes in the living biological environment, as well as contain surface ligands for the specific targeting of cancer cells.[5] PAA NPs (40-100 nm) have been widely used as a delivery vehicle for magnetic resonance imaging, photodynamic therapy, tumor delineation and chemotherapy.[8, 20, 21, 23-27] For example, cisplatin-loaded, F3 peptide-targeted PAA NPs effectively inhibited the

growth of both murine ovarian tumor models and human tumor xenograft models, which was found to be valid not only for cisplatin-sensitive but also for cisplatin-resistant cell lines.[8]

Extending our previous work on PAA NPs, we designed a new kind of hydrogel NP and studied its potential as a codelivery vehicle of doxorubicin and verapamil, for overcoming MDR. This kind of NP was prepared via the copolymerization of acrylamide (AA), 2-carboxyethyl acrylate (CEA) and 3-(acryloyloxy)-2-hydroxypropyl methacrylate (AHM), in a reverse microemulsion system. The novelty of this NP design is in its ability for adjusting the ratio of CEA/AA in the NP matrix, and this ratio determines the release kinetics of Dox. Either Dox or Vera were post-loaded into the NPs. Compared to the co-embedding of Dox and Vera into the same batch of NPs, the loading of drugs into separate NPs is chosen here because it facilitates dose optimization for both *in vitro* and *in vivo* applications. In other words, it is much easier to adjust the ratio of Dox-NPs to Vera-NPs, compared to preparing a series of NPs, each with a different ratio of Dox and Vera. We studied the release kinetics of each drug from the NPs. The NCI/ADR-RES cell line was chosen as a typical example of a Dox-resistant cell line. The accumulation in the NCI/ADR-RES cell line of Dox, from free Dox, Dox-NPs, free Dox + free Vera, and of Dox-NPs + Vera-NPs, was studied by confocal microscopy. The cytotoxicity on the NCI/ADR-RES cell line of either free Dox, Dox-NPs, free Dox + free Vera, Dox-NPs + free Vera, or of Dox-NPs + Vera-NPs, was also evaluated. The results demonstrated that the codelivery of Dox-NPs + Vera-NPs can best increase the intracellular accumulation of Dox, as well as significantly improve the cell-killing ability of Dox,

on this Dox resistant tumor cell line.

## **Experimental**

### **Materials**

Acrylamide (AA), 2-carboxyethyl acrylate (CEA), 3-(acryloyloxy)-2-hydroxypropyl methacrylate (AHM), verapamil, ammonium persulfate (APS), N,N,N',N'-tetramethylethylenediamine (TEMED), acrylic acid N-hydroxysuccinimide ester (acrylic acid-NHS), sodium dioctyl sulfosuccinate (AOT), Brij 30, dimethylsulfoxide (DMSO), phosphate-buffered saline tablet (PBS), and 3-(4,5-dimethylthiazolyl-2)-2,5-diphenyltetrazolium bromide (MTT) were purchased from Sigma Aldrich. Ethanol (95%) and hexane were purchased from Fisher Scientific. Doxorubicin was purchased from LC laboratories. NCI/ADR-RES cell line was purchased from National Cancer Institute. Hoechst 33342, Roswell Park Memorial Institute medium (RPMI-1640) and 0.05% Trypsin-EDTA were purchased from Invitrogen. Fluorescein-5-thiosemicarbazide (5-FTSC) was purchased from Marker Gene Technologies. All the water used was purified with a Milli-Q system from Millipore.

### **Preparation of co(CEA-AA) NPs**

Deoxygenated hexane (45 ml), AOT (1.6 g) and Brij 30 (4.3 ml) were mixed together, which was stirred vigorously to produce a microemulsion. The mixture of AA (497 mg), CEA (432 mg) and AHM (428 mg) were dissolved in DI water (1.3 ml), which was sonicated until dissolved completely. The monomer solution was added into the hexane solution under argon atmosphere. After 20 min, fresh APS solution (100  $\mu$ L,

10 wt%) and TEMED (100  $\mu$ L) were added into the mixture solution to initiate polymerization. After 2 h reaction, hexane was removed by rotary evaporation. The residue was suspended in ethanol and transferred into an Amicon ultra-filtration cell (Millipore Corp.). In order to remove the surfactants and unreacted monomers, NPs were washed with ethanol and DI water 5 times respectively with a 300 kDa filter membrane under the pressure of 15-20 psi. The NP solution were lyophilized and stored in freezer. The ratio of CEA/NPs can be adjusted by modifying the amount of monomers added at the beginning of the reaction

### **Preparation of FITC-labeled NPs**

5-FTSC, acryl acid-NHS (5.6 mg), AA (497 mg) and Brij 30 (0.1 ml) were dissolved in PBS buffer (1.3 ml) and kept stirring overnight. Then the solution was mixed with CEA (432 mg) and AHM (428 mg) and sonicated until dissolved completely. Deoxygenated hexane (45 ml), AOT (1.6 g) and Brij 30 (4.3 ml) were mixed together, which was stirred vigorously to produce a microemulsion. The monomer solution was added into the hexane solution under argon atmosphere. After 20 min, fresh APS solution (100  $\mu$ L, 10 wt%) and TEMED (100  $\mu$ L) were added into the mixture solution to initiate polymerization. After 2 h reaction, hexane was removed by rotary evaporation. The residue was suspended in ethanol and transferred into an Amicon ultra-filtration cell (Millipore Corp.). In order to remove the surfactants and unreacted monomers, NPs were washed with ethanol and DI water for 5 times respectively with a 300 kDa filter membrane under the pressure of 15-20 psi. The NPs were lyophilized and stored in freezer.

### **Characterization of NPs**

The size and zeta potential of NPs in aqueous solution were measured with Delsa Nano (Beckman Coulter). Scanning electron microscopy (SEM) images of NPs were obtained with an FEI Nova Nanolab Dualbeam focussed ion beam workstation and scanning electron microscope.

### **Loading of drugs into NPs**

Both Dox and Vera were loaded into NPs as follows: The NP solution in DI water (10 mg/ml, 1 ml) and a Dox or Vera solution in DI water (10 mg/ml, 20  $\mu$ l) were mixed together and kept stirring overnight. Then the drug-loaded NP solution was centrifuged in a centrifuge filter (100 kDa, Millipore) at 4000 g for three times, in order to remove the unbound drug molecules. The absorbance of Dox and Vera in NP solution was evaluated using an UV-1601 UV-*vis* spectrometer (Schimadzu). The absorption wavelength of Dox and Vera are 480 nm and 280 nm respectively. The concentrations of drugs in the NP solution were calculated from Beer-Lambert Law, while the concentration of the NP solution is known. The loading of drugs into the NPs (%) = (weight of drug to be loaded / weight of drug-loaded NPs) \*100; while the encapsulation efficiency (%) = (weight of drug found loaded / weight of drug input) \* 100.

### **Drug release from NPs**

The release kinetics of drugs from NPs was studied under the sink condition, since the concentration of Dox or Vera in our release study was 0.02 mg/ml, while the

solubility of Dox or Vera in PBS was around 10 mg/ml. Drug-loaded NP solution (1 mg/ml, 10 ml) in PBS buffer was prepared and incubated in water bath at 37 °C for release study. After incubation for 0 h, 1 h, 3 h, 5 h, 8 h and 24 h, 1 ml of Drug-NP solution was taken out and transferred into a centrifuge filter (100 k Da). The NP solution was centrifuged at 4000 g for 15 min at room temperature, and the filtrate was collected for UV-*vis* analysis. The factor of Dox degradation was also considered in the release study because of the easy degradation of Dox in PBS buffer.[28] The release profile of Dox was corrected for degradation of Dox.

### **Cell culture and *in vitro* cytotoxicity tests**

Human ovarian adenocarcinoma cell line NCI/ADR-RES was cultivated in RPMI 1640 medium with 10% heat-inactivated fetal bovine serum (Hi-FBS). *In vitro* cytotoxicity of drug-loaded NPs was analyzed in NCI/ADR-RES cell line, using an MTT assay: The cells were incubated with varying formulations of Dox on 96-well plates (5000 cells/well) for 2 days, in which the final concentration of Dox ranged from 0 to 20 µM. After that, cells were treated with an MTT reagent solution (0.83 mg/ml) in colorless RPMI medium for an additional 4 h. Then, the produced formazan crystals were dissolved in DMSO for 1 h. The visible absorption from each well was measured at 550 nm in a Biochrom Anthos microplate reader.

### **Confocal microscopy imaging**

The cells were cultivated on an eight-well chambered cover glass system (Nunc, Lab-Tek) overnight. After that, the cells were incubated with NP solution (1 mg/ml) for 6



h. Then the Hoechst 33342 (from Invitrogen) dye (1  $\mu\text{g/ml}$ ) was added into the cells and incubated with cells for 30 min. After incubation, unbound NPs and Hoechst dye were removed via rinsing with fresh DPBS buffer three times. The cells were incubated in colorless RPMI 1640 medium for the microscopy study, which was done with a Leica confocal microscope (SP-5X) at the Microscopy and Image Analysis Laboratory of the University of Michigan. The fluorescence signal of Dox was excited at 458 nm and detected over the range of 570 nm – 700 nm, while that of FITC-NPs was excited at 488 nm and the fluorescence was detected over the range of 498 nm – 530 nm. Quantitative analysis was performed by comparing the pixel intensity of the fluorescence images using ImageJ.

### **Statistical analysis**

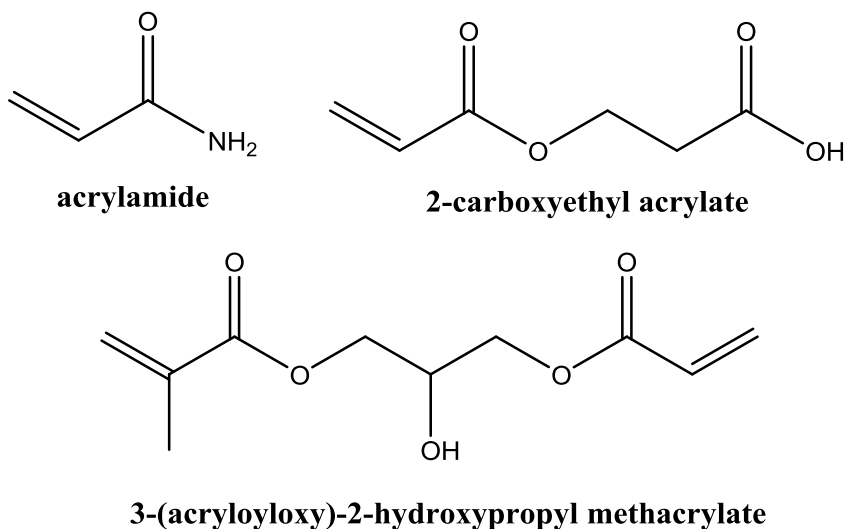
Results are presented as mean  $\pm$  standard deviation from three separate experiments at least. The intracellular uptake and cytotoxicity of Dox on NCI/ADR-RES cells were evaluated by One-Way ANOVA followed by Tukey's multiple comparison test using GraphPad Prism v6.00. All analyses were performed with a confidence interval at 95%. *P*-values  $< 0.05$  were considered significant.

## **Results and Discussion**

### **Preparation and characterization of co(CEA-AA) NPs**

This nanoplatform was prepared by a reverse microemulsion polymerization (Scheme 3.1), in a monomer mixture droplet containing AA (main matrix component), AHM (degradable crosslinker) and CEA (monomer providing negatively charged carboxyl

groups, uniformly throughout the NP). Cationic drugs (e.g. doxorubicin) can be loaded into negatively charged NPs via coulomb interaction. The mole fraction of CEA was varied from 8 % to 42 % so as to find the optimal CEA concentration that would offer high loading, as well as slow release, of Dox. Results from DLS analysis showed that the hydrodynamic diameter of NPs ranged from 48.4 nm to 94.5 nm in PBS buffer (pH 7.4) (Figure 1(a) and Table 3.1). Scanning electron microscopy (SEM) was used to observe the morphology of the dehydrated NPs, which showed an average diameter of around 17 nm (Figure 3.1(b)). The zeta potentials of these hydrogel NPs were around -50 mV to -60 mV in DI water (Table 3.1), which can be attributed to the presence of the carboxyl group in the NPs.



Scheme 3.1 Molecular structures of acrylamide (AA), 2-carboxyethyl acrylate (CEA) and 3-(acryloyloxy)-2-hydroxypropyl methacrylate (AHM).

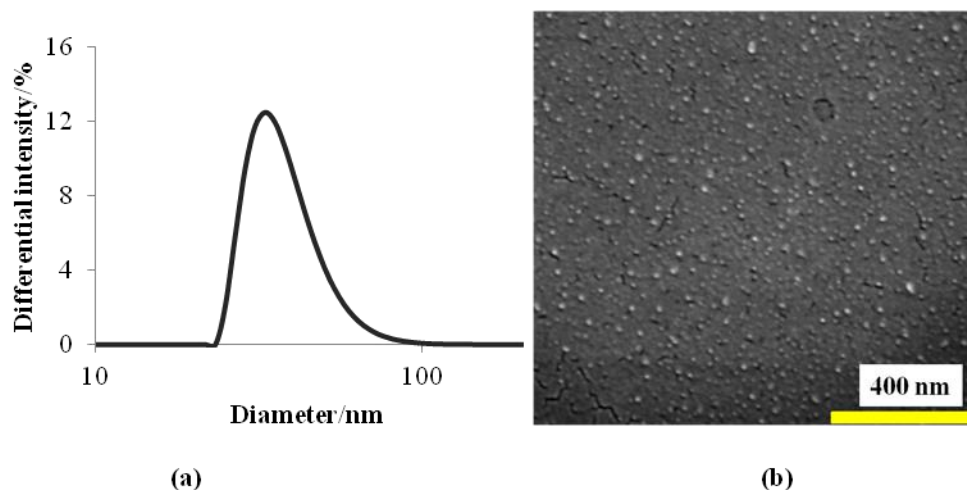


Figure 3.1 Size distribution of hydrogel NPs from DLS (a) and SEM image (b).

### **Ion responsive swelling of co(CEA-AA) NPs**

We analyzed the size of NPs with varying concentration of NaCl (from 0 mM to 1 M) using DLS (Figure 3.2), with NPs containing 25% CEA chosen as example. The results showed that the NP size decreased from 108 nm to 53 nm when NaCl concentration in buffer was increased from 0 mM to 100 mM. Further increase in NaCl concentration from 100 mM to 1 M has no significant impact on the size. These results demonstrate that the NP size was ion concentration-dependent in the range of 0 mM to 100 mM. In contrast, the size of PAA NPs (without any carboxyl group) was stable under varying ion concentrations in the same buffer.

This swelling behaviour is due to the COOH group in the NPs, which are bound to the matrix and cannot diffuse outside. The counter ions (e.g.  $\text{Na}^+$ ,  $\text{Ca}^{2+}$ ), remain confined inside the NPs, to maintain electrical neutrality. Thus the total mobile ion concentration inside the NPs exceeds that of the external solution under lower ion concentration in solution. This causes an osmotic pressure difference and leads to

increased water retention. This may be why the NPs swell in solution with lower ionic strength, and shrink on increasing the ionic strength. Thus the size of the NP, which is related to the osmotic pressure, depends on the difference between the mobile ion concentration inside NP matrix and the external solution.[29]

Table 3.1 Size (diameter) and zeta potential of hydrogel NPs from DLS. Data is shown as mean  $\pm$  standard deviation.

Sample	CEA (mol%)	Size/nm (PBS buffer), pH 7.4)	Zeta potential/mV (DI water)
#1	8%	48 $\pm$ 1	-49 $\pm$ 9
#2	25%	54 $\pm$ 1	-55 $\pm$ 3
#3	42%	74 $\pm$ 3	-59 $\pm$ 1
Dox-NPs <sup>a</sup>	25%	53 $\pm$ 1	-50 $\pm$ 3
Vera-NPs <sup>b</sup>	25%	52 $\pm$ 01	-40 $\pm$ 5

<sup>a</sup>: loading of Dox/NPs: 10% wt; <sup>b</sup>: loading of Vera/NPs: 2% wt

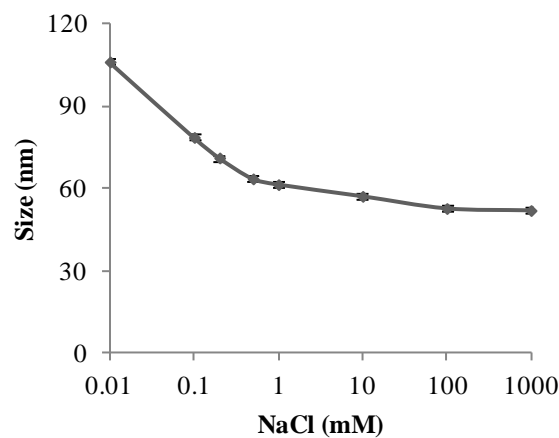


Figure 3.2 Diameter of hydrogel NPs (from DLS) vs. NaCl concentration in DI water. Error bars indicate the standard deviations.

### **Loading of drugs into NPs**

We loaded Dox and Vera into co(CEA-AA) NPs via post-loading, in which the CEA/NPs molar ratio was 8%, 25% and 42%. Dox and Vera were separately loaded into two sets of NPs. The loading of Dox and Vera in the NPs was determined to be 7.7 wt% and 8.0 wt% respectively, while the encapsulation efficiency was 81% and 80% respectively. DLS analysis results (Table 3.1) showed that the hydrodynamic size of Dox-NPs and Vera-NPs were  $53 \pm 1$  nm and  $52 \pm 1$  nm, respectively, which is similar to the size of blank NPs ( $54 \pm 1$  nm). After drug loading, the zeta potential of the NPs changed from  $-55 \pm 3$  mV to  $-50 \pm 3$  mV (Dox-NPs) and  $-40 \pm 5$  mV (Vera-NPs) respectively, probably due to partial neutralization of the surface charge on the NPs by the Dox and Vera. Additionally we were also able to efficiently incorporate methylene blue, a positively charged photosensitizer, into the co(CEA-AA) NPs by post loading (data not shown). These results suggested that the co(CEA-AA) NPs can be used as a high-capacity drug delivery vehicle for cationic drugs. The loading of drugs into NPs can be attributed to noncovalent bonding, especially the strong electrostatic interaction between the anionic NPs and the cationic drug molecules.

### **Degradation of Dox in Dox solution vs. Dox-NP solution**

Doxorubicin easily degrades in PBS buffer at body temperature. We compared the chemical degradation of Dox in free Dox solution and in Dox-NP solution. Figure 3 shows that 37% of Dox in free Dox solution degraded at 37 °C, in PBS buffer, within 24 h. Over the same time period, only 6% of Dox in the Dox-NP solution degraded (Figure 3.3). These results indicate that our NPs can effectively slow down the

degradation of Dox. Our results are analogous to results from a related publication,[30] which demonstrated that the encapsulation of Dox into polymeric NPs, composed of poly(ethylene glycol) and poloxamer 407 (Pluronic<sup>®</sup> F127), lengthened the lifetime of Dox from 50 h to 173 h in PBS buffer. This protective effect can be related to the encapsulation of Dox into the hydrophobic domains of the NPs, reducing the contact of Dox with the hydrophilic environment, which may induce a keto/enol tautomerization and deprotonation of Dox.<sup>[31]</sup>

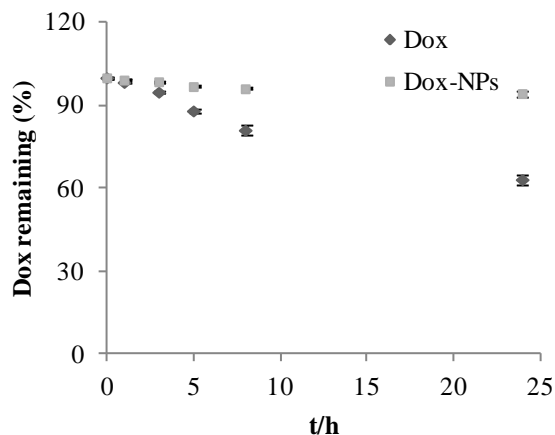


Figure 3.3 Degradation of Dox in Dox solution and Dox-loaded NP solution in PBS buffer at 37 °C. Dox concentration: 20 µg/mg; Dox/NPs: 2 wt%. Error bars indicate the standard deviations.

### Release kinetics of Dox and Vera from NPs

The drug release profile from the NP matrix significantly affects its therapeutic efficacy. We studied the release kinetics of Dox from NPs in which the molar ratio of CEA was fixed at 8%, 25% and 42%. The loading of Dox/NPs was kept at 2 wt%. For analysis of the release study results, the degradation of Dox in PBS buffer was taken into account, using Figure 3 as the calibration curve. It was found that around 20% of Dox was released in 24 h from NPs with 42% CEA; whereas over the same period,

around 40% of Dox was released from NPs with 8% CEA (Figure 3.4(a)). This shows that the release kinetics of Dox from NPs can be adjusted by the NP matrix composition, i.e., the mole fraction of CEA. We also studied the release kinetics of Vera from NPs over 24 h, and the loading of Vera/NPs was kept at 2% wt as well. The molar ratio of CEA in these NPs was fixed at 8%, 25%, and 42%. Around 60% - 70% of Vera was released over 24 h from each of the NPs (Figure 3.4(b)), demonstrating that the release profile of Vera did not depend on the mole fraction of CEA in the NP matrix.

The release kinetics of drugs from NPs are affected by the property of the matrix and the solubility of the drug in solution. We believe that the release of Dox from NPs is a diffusion-dominated process. The interaction of Dox with the NP matrix containing 42% CEA is stronger than that with the NP matrix containing 8% CEA (more negatively charged as indicated by zeta potential data), causing slower release of Dox from NPs with higher ratios of CEA. However, the release kinetics of Vera from the NPs is independent of the ratio of CEA/NPs, which may be related with the higher hydrophilicity of Vera.

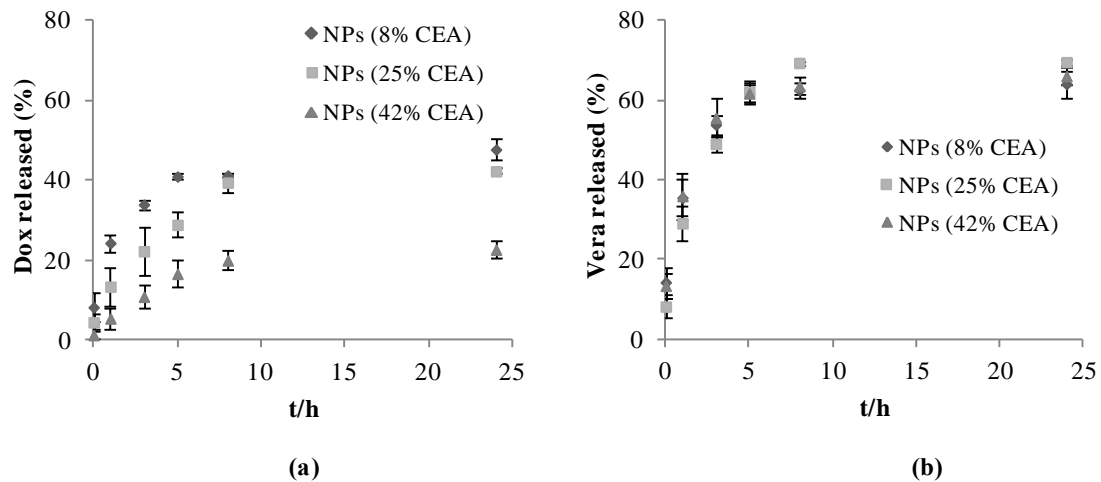
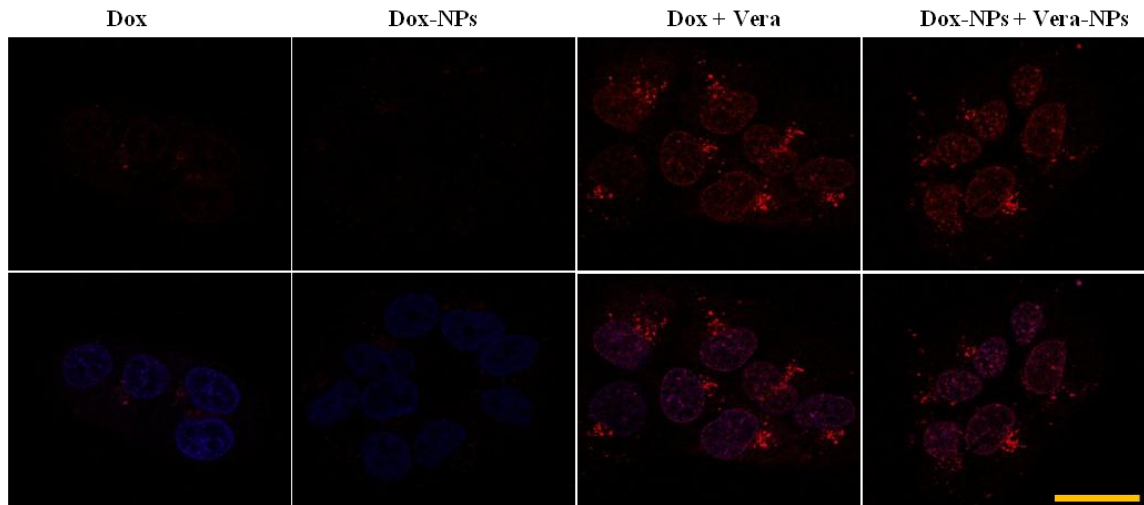
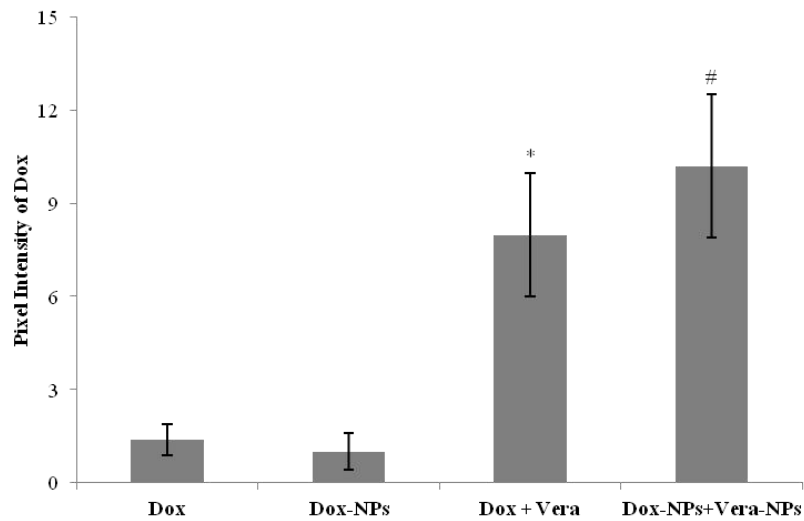


Figure 3.4 Release behaviours of Dox (a) and Vera (b), from hydrogel NPs with varying ratio of CEA in NP matrix. Dox/NPs: 2 wt%; Vera/NPs: 2 wt%; NP concentration: 1 mg/ml. Error bars indicate the standard deviations.





(a)



(b)

Figure 3.5 (a) Confocal microscopy images of NCI/ADR-RES cells after incubation with free Dox, Dox-NPs, free Dox + free Vera and Dox-NPs + Vera-NPs for 6 h. The nucleus is stained with the Hoechst dye (blue). Top: fluorescence signals from Dox (red); bottom: overlap of the fluorescence signals from Dox (red) and Hoechst dye (blue). (b) Histogram analysis of pixel intensity of Dox in (a). Dox concentration: 5  $\mu$ M; Vera concentration: 5  $\mu$ M; scale bar: 25  $\mu$ m. Error bars indicate the standard deviations. \*  $p < 0.05$ , in comparison to Dox; #  $p < 0.05$ , in comparison to Dox-NPs and Dox + Vera.

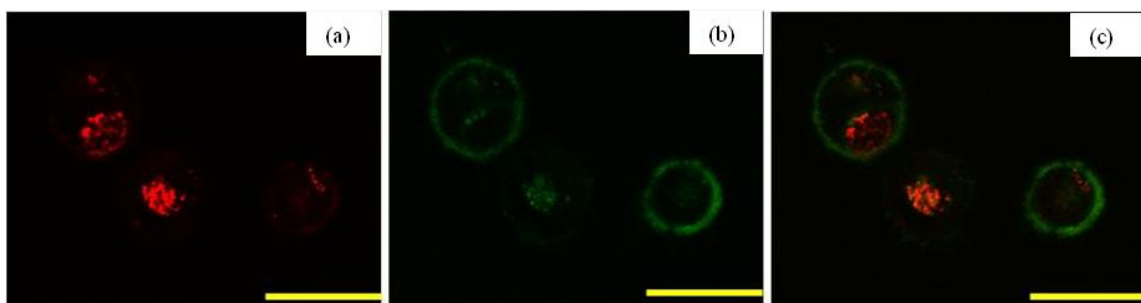


Figure 3.6 Confocal microscopy images of NCI/ADR-RES cells after 6h incubation with Dox-loaded FITC-NPs and Vera-loaded FITC-NPs. (a) Fluorescence signal from Dox (red) in the cells; (b) fluorescence signal from FITC-NPs (green) in the cells; (c) overlap of the fluorescence signal (orange) from Dox and FITC-NPs. Incubation time: 6 h; Dox concentration: 5  $\mu$ M; Vera concentration: 5  $\mu$ M; NP concentration: 1 mg/ml; scale bar: 25  $\mu$ m.

### **Accumulation of free Dox, Dox-NPs, free Dox + free Vera and Dox-NPs + Vera-NPs in NCI/ADR-RES cells**

We studied the accumulation of free Dox, Dox-NPs, free Dox + free Vera and Dox-NPs + Vera-NPs in cells, using confocal microscopy.[9, 32] The human ovarian adenocarcinoma cell line NCI/ADR-RES was chosen because of its reported resistance to Dox.[33] The distribution of Dox in cells was monitored via its own fluorescence signal (red in Figure 3.5). The cell nucleus was labelled with the Hoechst dyes (blue). Cells were incubated with different formulations of Dox for 6 h. After incubation, unbound drug or NPs were removed by washing with PBS buffer for three times. Our results (Figure 3.5(a)) showed that after incubation with free Dox for 6 h, the Dox signal (red) is detected in the NCI/ADR-RES cells, showing moderate uptake of Dox into these cells. After incubation with Dox-NPs for 6 h, the intensity of Dox in cells is marginally but not significantly less than that in those cells after incubation with free Dox. After incubation with free Dox + free Vera for 6 h, the signal intensity of Dox in cells was almost six times higher than the fluorescence intensity from cells with just free Dox ( $p < 0.05$ ); after incubation with Dox-NPs +

Vera-NPs for the same incubation time, the Dox signal in cells was almost seven times higher than the intensity in cells after incubation with just free Dox (Figure 3.5(b),  $p < 0.05$ ). The overlap of fluorescence signals from Dox and Hoechst dye (purple in Figure 3.5(a)) demonstrated that a large amount of Dox accumulated in the nucleus, while some still remained in the cytoplasm. These results demonstrated that Dox-NPs may not increase the uptake of Dox into tumor cells, compared to uptake from free Dox solution. However, most importantly, we found that the formulations of free Dox + free Vera and Dox-NPs + Vera-NPs did significantly improve the uptake of Dox in these drug-resistant cells. This confirms that Vera or Vera-NPs, as a chemosensitizer, can inhibit the drug efflux pump and increase the local concentration of Dox in these MDR cells (Scheme 2). [34]

#### **Colocalization of Dox and FITC-NPs in NCI/ADR-RES cells**

We also studied the colocalization of Dox molecules and carrier NPs in NCI/ADR-RES cells, via confocal microscopy. In order to track their signal, the NPs were labelled with FITC. Cells were incubated with Dox-FITC-NPs and Vera-FITC-NPs for 6 h. As mentioned previously, the Vera-NPs significantly improved the accumulation of Dox in cells. We observed strong fluorescence signals from Dox (red) and the FITC-NP (green), present in the cells (Figure 3.6(a)). The green signal from the FITC-NPs inside the cells demonstrates the successful uptake of these NPs into the cells (Figure 3.6(b)). However, we also note that a majority of the FITC signal was found on the cell membranes (Figure 3.6(b)), indicating that large amounts of NPs may stay attached to the cell membrane. The overlap of the fluorescence

signals from Dox and from FITC-NPs in cells is shown in Figure 6(c). The colocalization of Dox and FITC-NPs (orange) was found in certain locations in the cells, which may be the location of the Dox-loaded NPs, or of the Dox just released from the NPs. In addition, strong Dox signal (red) was also found in other locations inside the cells, showing the intracellular distribution of the Dox that was released from the NPs and delivered into the cells. These results demonstrate that co(CEA-AA) NPs can be taken up by the NCI/ADR-RES cells, and effectively deliver their Dox, which is important for function of the NPs, i.e., serving as a drug delivery vehicle.

***In vitro* Cytotoxicity on NCI/ADR-RES Cells of free Dox, Dox-NPs, free Dox + free Vera, Dox-NPs + free Vera and Dox-NPs + Vera-NPs**

The cytotoxicity of several formulations of Dox on NCI/ADR-RES cells (Dox-resistant cell line) was studied *in vitro* using MTT assay. Additionally, we also tested the cytotoxicity of blank NPs and free Vera on the same cell line. The concentration of Vera (5  $\mu$ M) was chosen following previous literature.[35] Our results (Figure 3.7) show that over 90% ( $\pm 7\%$ ) of the cells survived after incubation with blank NPs (1 mg/ml) for 2 days, while around 98% ( $\pm 8\%$ ) of the cells survived after incubation with free Vera (5  $\mu$ M) for 2 days, demonstrating that neither blank NPs nor Vera show significant toxicity to NCI/ADR-RES cells. Then we tested the cytotoxicity of free Dox, Dox-NPs, free Dox + free Vera, Dox-NPs + free Vera and Dox-NPs + Vera-NPs on the same cell line. Our results (Figure 3.8 and Table 3.2) showed that the estimated  $IC_{50}$  of free Dox on NCI/ADR-RES cells was higher than 20  $\mu$ M, *more than*

250 times higher than that on rat gliosarcoma cell line 9L cells (0.07  $\mu\text{M}$ ), confirming that the NCI/ADR-RES cell line is indeed resistant to Dox. The addition of free Vera reduced the  $\text{IC}_{50}$  of Dox to 10  $\mu\text{M}$  ( $p < 0.05$ ), which demonstrated that Vera improved the cell killing ability of Dox on this drug-resistant cell line, correlating well with its ability to improve the intracellular accumulation of Dox (see above). The  $\text{IC}_{50}$  of Dox-NPs was around 19  $\mu\text{M}$ , which shows that Dox-NPs have marginally better cell-killing efficiency, compared to free Dox. The  $\text{IC}_{50}$  of Dox-NPs + Vera-NPs was found to be around 2.5  $\mu\text{M}$ , which is 8 times lower than that of the free Dox alone ( $p < 0.05$ ), 4 times lower than that of free Dox + free Vera ( $p < 0.05$ ) and marginally but not significantly lower than that of the Dox-NPs + free Vera combination. Notably, the highest concentration of NPs for Dox-NPs + Vera-NPs in Figure 8 was 0.23 mg/ml, while our previous results (Figure 3.7) showed that blank NPs are not toxic to cells, even at 1 mg/ml. Therefore, we believe that the cytotoxicity of Dox-NPs + Vera-NPs (Figure 3.8) is not due to toxicity of the NP carriers.

The enhanced cell-killing ability of Dox-NPs + Vera-NPs can be attributed to the incorporation of the chemosensitizer (Vera), as well as to the protective effect of the nanoplatform on the Dox. In addition, the NPs may also partially protect Vera from being metabolised, which is mediated by cytochrome P450 enzymes in the NCI/ADR-RES cell line. It has been reported that Vera is subject to an extensive oxidative metabolism mediated by cytochrome P450 enzymes in the body.[36] Indeed, the expression of cytochrome P450 has been observed in the NCI/ADR-RES cell line.[37] Additionally, the encapsulation of Vera into NPs may largely obviate, *in vivo*, its potential for severe cardiac side effects.[4] This is due to the enhanced accumulation

of such Vera-containing NPs into tumors via the enhanced permeation and retention effect, and potentially by targeting [27]. In contrast, the much tighter cardiac endothelial walls may prevent any significant local Vera-NP accumulation, as they have been reported to exclude NPs larger than 6 nm.[11] Thus the use of hydrogel NPs for sensitizer delivery is expected to avoid sensitizer toxicity, while overcoming the MDR effect.

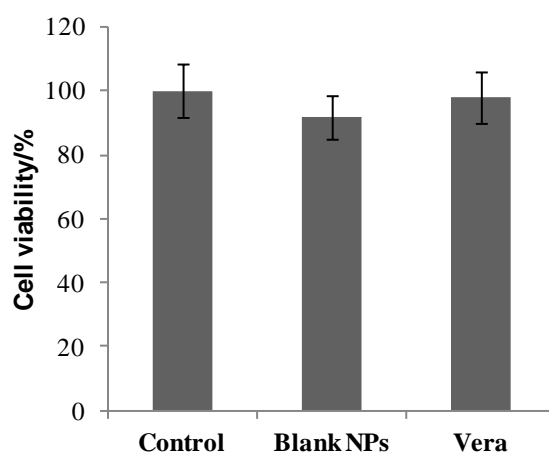


Figure 3.7 Viability of NCI/ADR-RES cells after incubation with blank NPs (1 mg/ml) and Vera (5  $\mu$ M) for 2 days. Error bars indicate the standard deviations.

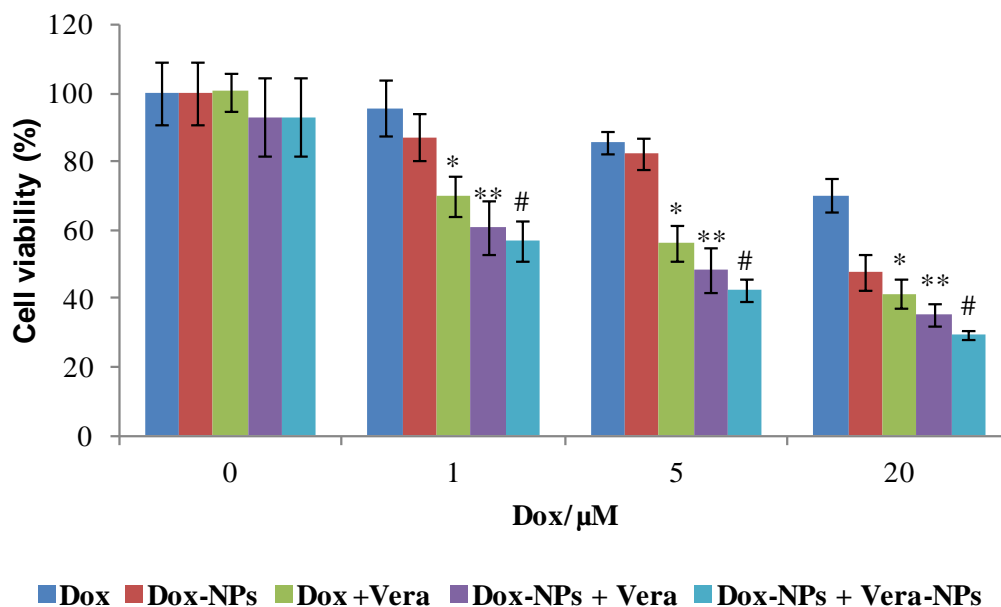


Figure 3.8 Viability of NCI/ADR-RES cells after incubation with free Dox, Dox-NPs, free Dox + free Vera, Dox-NPs + free Vera and Dox-NPs + Vera-NPs for 2 days. Dox /NPs: 7.7 wt%; Vera/NPs: 2 wt%; Vera concentration: 5  $\mu\text{M}$ . The total concentration of NPs in the codelivery of Dox-NPs + Vera-NPs is 0.23 mg/ml when the concentration of Dox is 20  $\mu\text{M}$ . Error bars indicate the standard deviations. Error bars indicate the standard deviations of seven separate experiments. \*  $p < 0.05$ , in comparison to Dox; \*\*  $p < 0.05$ , in comparison to Dox-NPs; #  $p < 0.05$ , in comparison to Dox-NPs and Dox + Vera.

Table 3.2  $\text{IC}_{50}$  value of Dox in the formulation of free Dox, Dox-NPs, free Dox + free Vera, Dox-NPs + free Vera and Dox-NPs + Vera-NPs.  $\text{IC}_{50}$  of Dox is the concentration of Dox required to cause 50% cell killing.

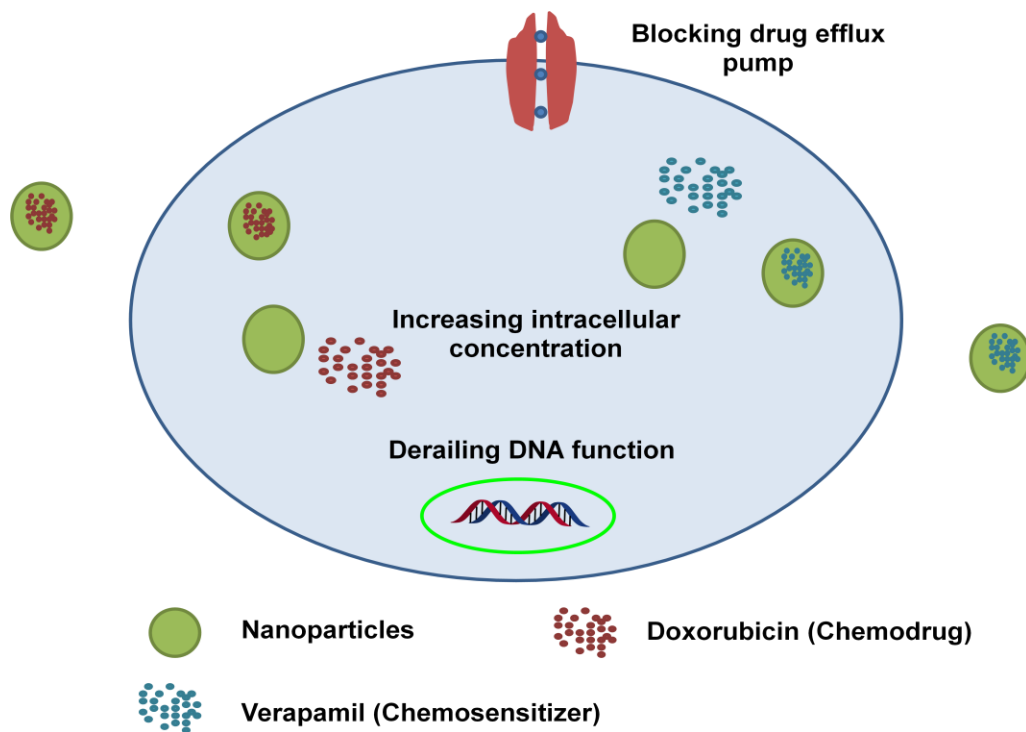
Estimated $\text{IC}_{50}$ of Dox/ $\mu\text{M}$	Dox	Dox-NPs	Dox + Vera	Dox-NPs + Vera	Dox-NPs + Vera-NPs
NCI/ADR-RES	>20	19	10	4.5	2.5

## Conclusion

With the aim of overcoming multidrug resistance, we successfully developed a codelivery system of doxorubicin (chemodrug) and verapamil (chemosensitizer) using hydrogel nanoparticles. These hydrogel NPs were prepared via copolymerization of AA, CEA and AHM, with a varying amount of the CEA towards optimized delivery

kinetics. We observed that the NP size was ion-concentration dependent. The NP matrix enhances the stability of Dox, and the NP size promises to minimize the cardio-toxicity of Vera, as well as potential Dox toxicity to other organs. These NPs also have a high potential for flexible engineerability, including future specific targeting to the tumor. With this nanoplatform, high loading and slow release of both Dox and Vera have been achieved successfully. The release kinetics of Dox from the NPs is adjustable, based on the ratio of carboxyl groups per NP. This nanoplatform also protects Dox from degradation. Notably, these NP combinations were well incorporated by the Dox-resistant cell line (NCI/ADR-RES), thus behaving as an efficient delivery vehicle for Dox. Moreover, with the aid of free Vera and especially Vera-NPs, the intracellular Dox concentration can be significantly increased, demonstrating the advantage of such a synergistic delivery approach for drug resistant cells. Most importantly, the codelivery of Dox-NPs + Vera-NPs did show a synergistic killing effect on these drug-resistant cells. The  $IC_{50}$  of Dox-NPs + Vera-NPs was 8 times lower than that of free Dox alone, or Dox-NPs, and 4 times lower than that of free Dox + free Vera. Thus the codelivery nanoplatform increased the drug efficacy and will potentially minimize toxicity, of both chemodrug (due to tumor targeting) and chemosensitizer (due to size of NP, protecting from cardio-toxicity). It offers a promising nanomedicine approach to drug resistant tumor therapy, and thus should undergo further *in vivo* studies.





Scheme 3.2 Delivery into drug-resistant tumor cells of both doxorubicin (derails DNA) and verapamil (blocks efflux pump) with hydrogel NPs.

## **Acknowledgements**

We thank Teppei Shirakura for discussions on nanoparticle preparation, and Leshern Karamchand for the discussions on data analysis. We would like to thank James Windak and Paul Lennon at the Chemistry Instrument Shop for their technical support on the UV-*vis* spectrometer, and the staff of the Electron Microscopy Analysis Laboratory at the University of Michigan for their help on SEM imaging. We also thank the staff at the Microscopy and Image Analysis laboratory at the University of Michigan for their help with confocal microscopy imaging.

## References

1. Capella, M.A.M. and L.S. Capella, *A light in multidrug resistance: Photodynamic treatment of multidrug-resistant tumors*. Journal of Biomedical Science, 2003. **10**(4): p. 361-366.
2. Szakacs, G., et al., *Targeting multidrug resistance in cancer*. Nature Reviews Drug Discovery, 2006. **5**(3): p. 219-234.
3. Hu, C.-M.J., S. Aryal, and L. Zhang, *Nanoparticle-assisted combination therapies for effective cancer treatment*. Therapeutic Delivery, 2010. **1**(2): p. 323-334.
4. Ozols, R.F., et al., *Verapamil and adriamycin in the treatment of drug-resistant ovarian cancer patients*. Journal of Clinical Oncology, 1987. **5**(4): p. 641-7.
5. Koo, Y.E.L., et al., *Brain cancer diagnosis and therapy with nanoplatforms*. Advanced Drug Delivery Reviews, 2006. **58**(14): p. 1556-1577.
6. Davis, M.E., Z. Chen, and D.M. Shin, *Nanoparticle therapeutics: an emerging treatment modality for cancer*. Nature Reviews Drug Discovery, 2008. **7**(9): p. 771-782.
7. Susa, M., et al., *Doxorubicin loaded Polymeric Nanoparticulate Delivery System to overcome drug resistance in osteosarcoma*. BMC Cancer, 2009. **9**: p. 399.
8. Winer, I., et al., *F3-targeted cisplatin-hydrogel nanoparticles as an effective therapeutic that targets both murine and human ovarian tumor endothelial cells in vivo*. Cancer Research, 2010. **70**(21): p. 8674-8683.
9. Meng, H., et al., *Engineered Design of Mesoporous Silica Nanoparticles to Deliver Doxorubicin and P-Glycoprotein siRNA to Overcome Drug Resistance in a Cancer Cell Line*. ACS Nano, 2010. **4**(8): p. 4539-4550.
10. Khdair, A., et al., *Nanoparticle-mediated combination chemotherapy and photodynamic therapy overcomes tumor drug resistance in vitro*. European Journal of Pharmaceutics and Biopharmaceutics, 2009. **71**(2): p. 214-222.
11. Gaumet, M., et al., *Nanoparticles for drug delivery: The need for precision in reporting particle size parameters*. European Journal of Pharmaceutics and Biopharmaceutics, 2008. **69**(1): p. 1-9.
12. Wang, J., et al., *In Vitro Cytotoxicity of Stealth Liposomes Co-encapsulating Doxorubicin and Verapamil on Doxorubicin-Resistant Tumor Cells*. Biological and Pharmaceutical Bulletin, 2005. **28**(5): p. 822-828.
13. Wu, J., et al., *Reversal of Multidrug Resistance by Transferrin-conjugated Liposomes Co-encapsulating Doxorubicin and Verapamil*. J Pharm Pharmaceut Sci, 2007. **10**(3): p. 8.
14. Theodossiou, T.A., M.C. Galanou, and C.M. Paleos, *Novel Amiodarone-Doxorubicin Cocktail Liposomes Enhance Doxorubicin Retention and Cytotoxicity in DU145 Human Prostate Carcinoma Cells*. Journal of Medicinal Chemistry, 2008. **51**(19): p. 6067-6074.
15. Wong, H.L., et al., *Simultaneous delivery of doxorubicin and GG918 (Elacridar) by new Polymer-Lipid Hybrid Nanoparticles (PLN) for enhanced treatment of multidrug-resistant breast cancer*. Journal of Controlled Release, 2006. **116**(3): p. 275-284.
16. Fan, L., et al., *Co-delivery of PDTA and doxorubicin by multifunctional micellar nanoparticles to achieve active targeted drug delivery and overcome multidrug resistance*. Biomaterials, 2010. **31**(21): p. 5634-5642.
17. Li, P.-Y., et al., *Poly(l-lactide)-Vitamin E TPGS Nanoparticles Enhanced the Cytotoxicity of Doxorubicin in Drug-Resistant MCF-7 Breast Cancer Cells*. Biomacromolecules, 2010. **11**(10): p. 2576-2582.
18. Shieh, M.-J., et al., *Reversal of doxorubicin-resistance by multifunctional nanoparticles in MCF-7/ADR cells*. Journal of Controlled Release, 2011. **152**(3): p. 418-425.
19. Lee, Y.-E.K. and R. Kopelman, *Targeted, Multifunctional Hydrogel Nanoparticles for Imaging and Treatment of Cancer: Multifunctional Nanoparticles for Drug Delivery Applications*, S. Svenson and R.K. Prud'homme, Editors. 2012, Springer US. p. 225-255.
20. Ross, B., et al., *Photonic and magnetic nanoexplorers for biomedical use: from subcellular imaging to cancer diagnostics and therapy*. Proc. SPIE, 2004. **5331**: p. 76-83.
21. Kopelman, R., et al., *Multifunctional nanoparticle platforms for in vivo MRI enhancement*

- and photodynamic therapy of a rat brain cancer. *Journal of Magnetism and Magnetic Materials*, 2005. **293**(1): p. 404-410.
22. Pallua, N. and T.P. Wolter, *A 5-Year Assessment of Safety and Aesthetic Results after Facial Soft-Tissue Augmentation with Polyacrylamide Hydrogel (Aquamid): A Prospective Multicenter Study of 251 Patients*. *Plastic and Reconstructive Surgery*, 2010. **125**(6): p. 1797-1804 10.1097/PRS.0b013e3181d18158.
  23. Wang, S., et al., *Multifunctional Biodegradable Polyacrylamide Nanocarriers for Cancer Theranostics—A “See and Treat” Strategy*. *Acs Nano*, 2012. **6**(8): p. 6843-6851.
  24. Harrel, J.A. and R. Kopelman, *Biocompatible probes measure intracellular activity*. *Biophotonics Int.*, 2000. **7**: p. 22-24.
  25. Xu, H., et al., *Photoexcitation-based nano-explorers: Chemical analysis inside live cells and photodynamic therapy*. *Israel Journal of Chemistry*, 2004. **44**(1-3): p. 317-337.
  26. Reddy, G.R., et al., *Vascular targeted nanoparticles for imaging and treatment of brain tumors*. *Clinical Cancer Research*, 2006. **12**(22): p. 6677-6686.
  27. Nie, G., et al., *Hydrogel Nanoparticles with Covalently Linked Coomassie Blue for Brain Tumor Delineation Visible to the Surgeon*. *Small*, 2012. **8**(6): p. 884-891.
  28. Janssen, M.J.H., et al., *Doxorubicin decomposition on storage. Effect of pH, type of buffer and liposome encapsulation*. *International Journal of Pharmaceutics*, 1985. **23**(1): p. 1-11.
  29. Dadsetan, M., et al., *A stimuli-responsive hydrogel for doxorubicin delivery*. *Biomaterials*, 2010. **31**(31): p. 8051-8062.
  30. Missirlis, D., et al., *Doxorubicin encapsulation and diffusional release from stable, polymeric, hydrogel nanoparticles*. *European Journal of Pharmaceutical Sciences*, 2006. **29**(2): p. 120-129.
  31. Beijnen, J.H., O.A.G.J. van der Houwen, and W.J.M. Underberg, *Aspects of the degradation kinetics of doxorubicin in aqueous solution*. *International Journal of Pharmaceutics*, 1986. **32**(2-3): p. 123-131.
  32. Shen, F., et al., *Quantitation of Doxorubicin Uptake, Efflux, and Modulation of Multidrug Resistance (MDR) in MDR Human Cancer Cells*. *Journal of Pharmacology and Experimental Therapeutics*, 2008. **324**(1): p. 95-102.
  33. Wu, L., et al., *Multidrug-resistant Phenotype of Disease-oriented Panels of Human Tumor Cell Lines Used for Anticancer Drug Screening*. *Cancer Research*, 1992. **52**(11): p. 3029-3034.
  34. Jabr-Milane, L.S., et al., *Multi-functional nanocarriers to overcome tumor drug resistance*. *Cancer Treatment Reviews*, 2008. **34**(7): p. 592-602.
  35. Sadasivan, R., et al., *Reversal of multidrug resistance in HL-60 cells by verapamil and liposome-encapsulated doxorubicin*. *Cancer Letters*, 1991. **57**(2): p. 165-171.
  36. Pauli-Magnus, C., et al., *Characterization of the Major Metabolites of Verapamil as Substrates and Inhibitors of P-glycoprotein*. *Journal of Pharmacology and Experimental Therapeutics*, 2000. **293**(2): p. 376-382.
  37. Yu, L.J., et al., *P450 Enzyme Expression Patterns in the NCI Human Tumor Cell Line Panel*. *Drug Metabolism and Disposition*, 2001. **29**(3): p. 304-312.

## **Chapter 4 Click Conjugation of Peptide to Doxorubicin-loaded Hydrogel Nanoparticles for Targeted Tumor Therapy**

### **Introduction**

Doxorubicin is one of the most effective chemotherapy drugs.[1] It has been widely used for the treatment of several forms of cancer: leukemia, bladder, breast and other cancers. The clinical use of doxorubicin is limited by its side effects, e.g. cardiotoxicity, as well as by multidrug resistance.[2, 3] These side effects are related with poor biodistribution and unfavorable pharmacokinetics of Dox.

Hydrogel nanoparticles (NPs) have emerged as an important drug delivery vehicle for cancer therapy.[4, 5] These NPs preferentially accumulate in tumor areas, via the enhanced permeability and retention effect (EPR), because the vasculature in the tumor area is generally leaky, and the tumor lymphatic system is deficient.[6-8] As a drug delivery vehicle, such NPs offer a strategy to (1) prolong drug circulation time, (2) control the drug release kinetics and (3) enhance solubility of hydrophobic therapeutics. [4, 9] Because of such unique properties, these hydrogel NPs can improve the drug accumulation in the tumor area, thus reducing the side effects from the delivered drugs. Such NPs have also been shown to alleviate the drug resistance effect of cancer cells via various mechanisms.[10-12]

One kind of hydrogel NPs, polyacrylamide NPs, is highly soluble in water, biocompatible, and has enabled multifunctionality.[5, 9] It has been widely used as a drug delivery vehicle for photodynamic therapy, tumor delineation and chemotherapy.[11, 13-15] Recently, we prepared a new kind of hydrogel NPs via the copolymerization of acrylamide (AA), 2-carboxyethyl acrylate (CEA) and 3-(acryloyloxy)-2-hydroxypropyl methacrylate in a micro-emulsion system.[16] It has been used as a delivery vehicle for doxorubicin (chemotherapy drug), verapamil (chemosensitizer) and methylene blue (photosensitizer). However, the uptake of these anionic NPs by tumor cells is always challenging, because they would be repelled by the cell membrane, which is also anionic.[4]

To address this issue, one possible way is attaching tumor-targeting moieties onto the NP surface for “active targeting”. Active targeting further enhances the accumulation of delivered drugs in the tumor area, caused by the passive targeting by the EPR effect. These tumor-targeting ligands, on the NP surface, can recognize receptors on cancer cells, via receptor-mediated endocytosis.[17-19] They can facilitate the retention time of NPs in the tumor area [9, 13, 15], penetrate the tumor tissue [20] and overcome drug resistance by neutralizing the P-glycoprotein-mediated drug efflux pump [12]. Some examples of targeting ligands include peptides, antibodies, aptamers and folate.[21]

Nucleolin, a shuttle protein between the nucleus and the cell surface, is highly expressed on angiogenic tumor vasculatures and certain kinds of tumor cells. Via interaction with nucleolin on the cell surface, the F3 peptide can bind to those tumor

cells.[22, 23] F3 peptide has been attached on NPs successfully, which significantly improved the uptake of such NPs by tumor cells and tumor endothelial cells, *in vitro* and *in vivo*. [11, 13, 14, 20] For example, it is reported that F3-targeted hydrogel NPs (F3-NPs) bind to human tumor endothelial cells *in vitro* and to human tumor vessels *in vivo*. [11] In addition, the attachment of the F3 peptide can reduce the trafficking of the NPs to lysosomes. [24] The latter demonstrated that F3-targeted NPs can prevent the delivered drugs from entering the acidic lysosomes and thus avoid their potential degradation, thereby improving the release behavior of small molecule drugs. [24] Previously, the F3 peptide was attached onto amine-functionalized hydrogel NPs via maleimide-activated crosslinkers. [25] The latter, however, is not suitable for F3 conjugation onto the co(CEA-AA) NPs.

To further facilitate the ability of co(CEA-AA) NPs as a drug carrier, we planned to attach F3 peptides onto them, aimed at enhancing the NP uptake by tumor cells. The co(CEA-AA) NPs were synthesized via a free radical polymerization, performed in a reverse microemulsion system, [16] and conjugated with an azide group, via carbodiimide chemistry. [27] The alkyne-F3 peptide was synthesized and conjugated to the azide-functionalized NPs via a copper (I) catalyzed azide-alkyne “Click” reaction, which is a popular method for the peptide-polymer conjugation. [26] This conjugation method is modular, high yielding, stereo-specific, and can be performed under ambient conditions. [26, 27] The uptake efficiency of F3-targeted NPs by the glioma cell line 9L (high expression of nucleolin), human breast cancer cell line MCF-7 (low expression of nucleolin), and human ovarian cell line NCI/ADR-RES (drug-resistant) is evaluated by confocal microscopy. We also evaluated the loading

and releasing of doxorubicin from the F3-targeted NPs. Finally, the cytotoxicity, toward 9L cells, of Dox-loaded, F3-targeted NPs was studied, *in vitro*.

## **Experimental**

### **Materials**

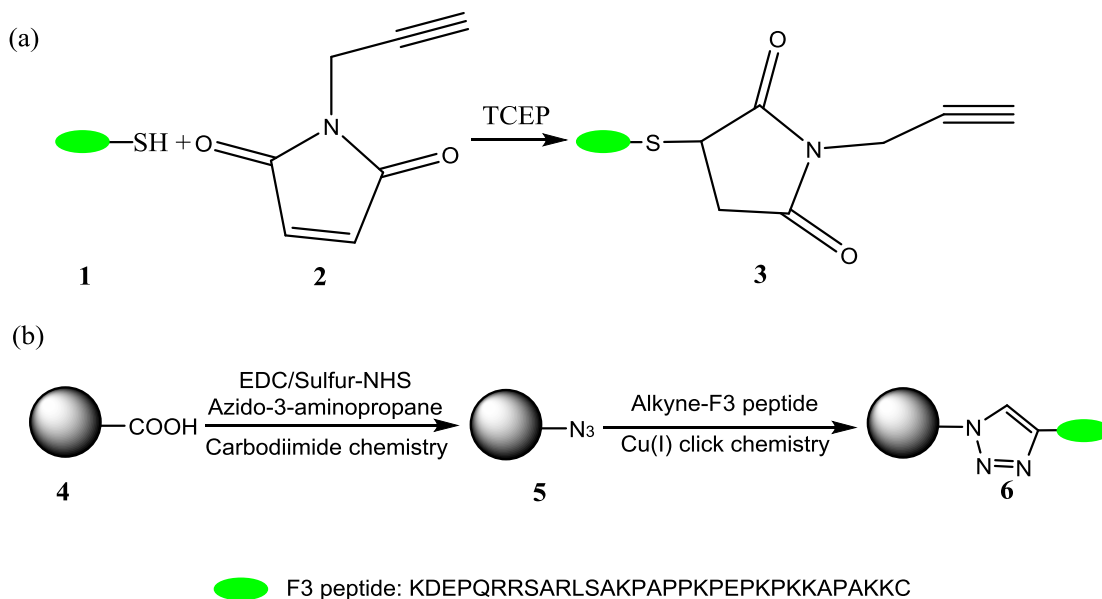
Acrylamide (AA), 2-carboxyethyl acrylate (CEA), 3-(Acryloyloxy)-2-hydroxypropyl methacrylate (AHM), ammonium persulfate (APS), N,N,N',N'-tetramethylethylenediamine (TEMED), sodium dioctyl sulfosuccinate (AOT), Brij 30, dimethylsulfoxide (DMSO), L-ascorbic acid, copper(II) sulfate, phosphate-buffered saline tablet (PBS), Tris(2-carboxyethyl)phosphine (TCEP) and 3-(4,5-dimethylthiazolyl-2)-2,5-diphenyltetrazolium bromide (MTT) were purchased from Sigma Aldrich. Ethanol (95%) and hexane were purchased from Fisher Scientific. 1-Ethyl-3-[3-dimethylaminopropyl]carbodiimide (EDC) and N-hydroxysulfosuccinimide (Sulfo-NHS) were purchased from Thermo Scientific. Human ovarian adenocarcinoma cell line, NCI/ADR-RES was purchased from the USA National Cancer Institute. The 9L rat gliosarcoma and human breast adenocarcinoma cell line MCF-7 were obtained from American Type Culture Collection (Manassas, VA, USA). Roswell Park Memorial Institute medium (RPMI-1640), DAPI and 0.05% Trypsin-EDTA were purchased from Invitrogen. Acetylene Fluor 488 was purchased from Click Chemistry Tools. 1-(prop-2-yn-1-yl) pyrrole-2,5-dione was purchased from Enamine Ltd (Ukraine). F3 peptide (KDEPQRRSARLSAKPAPPKPEPKPKKAPAKKC) was purchased from SynBioSci. Six-well cell culture plates and 96-well microplates were purchased from BD



Biosciences. All chemicals were used as received, without further purification. All the water used was purified with a Milli-Q system from Millipore.

### **Synthesis of co(CEA-AA) NPs**

Deoxygenated hexane (45 ml), AOT (1.6 g) and Brij 30 (4.3 ml) were mixed together, and stirred vigorously, to produce a microemulsion. The mixture of AA (639 mg), CEA (144 mg) and AHM (428 mg) was dissolved in DI water (1.3 ml), which was sonicated until dissolved completely. The monomer solution was added into the hexane solution, under argon atmosphere. After 20 min, fresh APS solution (100  $\mu$ L, 10 wt%) and TEMED (100  $\mu$ L) were added into the mixture solution, to initiate polymerization. After a 2 h reaction, hexane was removed by rotary evaporation. The residue was suspended in ethanol and transferred into an Amicon ultra-filtration cell (Millipore Corp.). In order to remove the surfactants and unreacted monomers, the NPs were washed with ethanol and DI water 5 times, respectively, with a 300 kDa filter membrane, under the pressure of 15-20 psi. The NP solutions were lyophilized and stored in freezer.



Scheme 4.1 (a) Synthesis of alkyne-F3 peptide (TCEP: reducing agent); (b) Synthesis of F3-targeted co(CEA-AA) NPs via carbodiimide chemistry and click chemistry.

### Modification of F3 with alkyne

F3 peptide (2 ml, 10 mg/ml in PBS buffer), 1-(prop-2-yn-1-yl) pyrrole-2,5-dione (compound 2 in Scheme 4.1, 0.5 ml, 7.6 mg/ml in DMF) and TCEP (56  $\mu$ L, 50 mg/ml in PBS) were mixed together stirred overnight. (Scheme 4.1(a)) TCEP was used to reduce the possible disulfide bond between F3 peptide molecules. The solution mixture was diluted 10 times in PBS buffer. Then the NPs were purified using an Amicon ultra-filtration cell (1000 Da) (5 times in DI water), freeze dried and stored in a freezer. The molecular weight of F3 peptide and alkyne-F3 peptide (compound 3) was analyzed with an Agilent Q-TOF HPLC/MS Electrospray instrument: the peptide was dissolved in DI water (1 mg/ml), then 5  $\mu$ l of the peptide solution was diluted into 500  $\mu$ l of acetonitrile; after that, 2  $\mu$ l of the diluted peptide solution was injected into the instrument, which is carried by a 0.4 ml/min flow of 90% acetonitrile/10% water (with 0.1% formic acid).

F3 peptide and alkyne-F3 peptide were analyzed with Ultra Performance Liquid Chromatography (UPLC), which was carried out on a Waters Acquity Peptide Mapping System equipped with a photodiode array detector. The peptide solution (1 mg/ml) was run on an Acquity BEH C4 column (100 x 2.1 mm, 1.7  $\mu$ m) while the flow rate was kept at 0.208 mL/min. Gradient elution was a mixture of water/acetonitrile (ACN), in which the ratio of water/ACN ranged from 99:1 (v/v) to 20: 80. Flow rate was maintained at 0.208 mL/min. Trifluoroacetic acid (TFA) at 0.14 wt % in water as well as in ACN was used as a counter ion. The column temperature was maintained at 35  $^{\circ}$ C.

### **Synthesis of azide-NPs**

Azido-3-aminopropane was synthesized as reported.[28] NPs (10 mg) were dissolved in PBS buffer (pH 7.4) at 10 mg/ml, followed by 1-Ethyl-3-[3-dimethylaminopropyl]carbodiimide (EDC, 6.3 mg) and N-hydroxysulfosuccinimide (Sulfo-NHS, 7.3 mg) are dissolved in the NP solution. (Scheme 4.1(b)) Azido-3-aminopropane (3.4 mg, 50 mg/ml in acetonitrile) was added into the NP solution dropwise. The mixed solution was kept stirring for 4 h. Then the azide-NPs (compound 5 in Scheme 4.1) were purified by centrifuge in a centrifuge filter (100 k Da, 4000 g), in PBS buffer, for four times and collected at 10 mg/ml, which was stored at 4  $^{\circ}$ C prior to use.

### **Characterization of NPs**

The size and zeta potential of the NPs in aqueous solution were measured using a Delsa Nano (Beckman Coulter). The FTIR spectrum of the NPs was analyzed with a

Spectrum BX FTIR (PerkinElmer). <sup>1</sup>H NMR spectra of the NPs were analyzed with a Varian Inova 500 MHz spectrometer.

### **Attachment of alkyne-F3 peptide onto azide-NPs**

Azide-NPs (1 ml, 10 mg/ml in PBS), alkyne-F3 (100  $\mu$ L, 10 mg/ml in H<sub>2</sub>O), CuSO<sub>4</sub> (20  $\mu$ L, 10 mM in water) and L-ascorbic acid (10  $\mu$ L, 50 mM in water) were mixed together and stirred at room temperature overnight. (Scheme 4.1(b)) The mixture solution was purified using centrifuge in a centrifuge filter (100 k Da, 4000 g), for five times, in PBS buffer, and four times in DI water. The F3-conjugated NP (compound 6 in Scheme 4.1) solution was adjusted to 10 mg/ml and stored at 4 °C. The amount of F3 peptide on the NPs was analyzed by quantitative amino acid analysis (QAAA, Protein Chemistry Lab, Texas A&M University).

### **Fluorescence labeling of NPs**

In order to track NPs under confocal microscopy, the NPs were labeled with Acetylene Fluor 488 (AF488). AF488 (2  $\mu$ L, 10 mg/ml in DMSO), CuSO<sub>4</sub> (20  $\mu$ L, 10 mM in water) and L-ascorbic acid (10  $\mu$ L, 50 mM in water) were added into an azide-NP solution (1 ml, 10 mg/ml in PBS) and stirred for 4 h. The mixture solution was washed in a centrifuge filter (100 k Da, 4000 g), in PBS buffer, for four times, and the AF488-labeled NPs (10mg/ml) were stored at 4 °C, prior to use.

### **Loading of doxorubicin into NPs**

Doxorubicin (Dox) was loaded into the nontargeted or F3-targeted NPs via post-loading. The particle solution in DI water (1 mg/ml, 10 mg/ml) and Dox solution in

DI water (100  $\mu$ L, 10 mg/ml) were mixed together and kept stirring overnight. Then the drug-loaded NP solution was centrifuged in a centrifuge filter (100 k Da, Millipore), at 4000 g, for three times, in order to remove the free drug molecules.

### **Drug release from NPs**

Drug-loaded NP solution (0.2 mg/ml, 10 ml) in PBS buffer was prepared via the dilution of drug-loaded NP solution (10 mg/ml, 0.2 ml) with PBS buffer. After that, this drug-loaded NP solution in PBS buffer (0.2 mg/ml, 10 ml) was incubated in a water bath at 37  $^{\circ}$ C, for a drug releasing study. After incubation for 0 h, 1 h, 3 h, 5 h, 8 h and 24 h, 1 ml of Drug-NP solution was taken out and transferred into a centrifuge filter (100 k Da). The NP solution was centrifuged at 4000 g for 15 min at room temperature, and the filtrate was collected for UV-*vis* analysis. In view of the easy degradation of free Dox in PBS buffer, a calibration showing the degradation of free Dox was performed. The ratio of Dox released at time  $t$  equals to the (amount of Dox released at time  $t$  after degradation)/(the total amount of Dox at time  $t$  after degradation).

### **Cell culture and confocal microscopy imaging**

The human breast adenocarcinoma cell line MCF-7, rat gliosarcoma cell line 9L, and human ovarian adenocarcinoma cell line NCI/ADR-RES were cultivated in RPMI 1640 medium with 10% heat-inactivated fetal bovine serum (Hi-FBS) and 1% PSG. The cells were cultivated on an eight-well chambered cover glass system (Nunc, Lab-Tek) for 2 days. After that, the cells were incubated with AF488-labeled NPs (1 mg/ml in PBS buffer) for 2 h. After incubation, unbound NPs were removed via

rinsing with fresh DPBS buffer, three times. The cells were fixed with paraformaldehyde (4%) for 15 min, and washed with fresh DPBS buffer three times. Then the cells were stained with DAPI for 5 min and washed with fresh DPBS buffer three times. After that, the cells were stored in PBS buffer and the fluorescence signal of the NPs was analyzed with an Olympus DSU (Disk Scanning Unit) Confocal Microscope. Pixel intensity of the fluorescence picture was analyzed with ImageJ.

### ***In vitro* cytotoxicity tests**

*In vitro* cytotoxicity of drug-loaded NPs was analyzed in the 9L cell line, using an MTT assay: the cells were incubated on a 96-well plate overnight (5000 cells/well), then varying formulations of Dox or NPs were added into the cell solution and co-incubated with cells for 4 h. After that, the cell medium was replaced with fresh medium and the cells were incubated for 2 days. Then cells were treated with an MTT reagent solution (0.83 mg/ml), in colorless RPMI medium, for an additional 4 h. Then, the produced formazan crystals were dissolved in DMSO for 1 h. The visible absorption from each well was measured at 550 nm in a Biochrom Anthos microplate reader.

### **Competitive uptake tests**

9L cells were incubated with F3 peptide (0  $\mu$ M, 2  $\mu$ M, 10  $\mu$ M, 50  $\mu$ M and 200  $\mu$ M) for 30 min. After that, AF488-labeled F3-NPs were added to the cells and incubated with cells for 2 h. Then the fluorescence intensity of F3-NPs was studied with fluorescence microscopy and analyzed quantitatively with ImageJ.

## Results and Discussion

### Synthesis and characterization of co(CEA-AA) NPs

The hydrogel NPs were prepared by a reverse microemulsion polymerization.[16] The results from dynamic light scattering (DLS) showed that the hydrodynamic size of NPs was  $57.5 \pm 0.1$  nm in PBS buffer (Table 4.1), indicating the successful synthesis of the nanoparticles. The zeta potential of these hydrogel NPs was also analyzed, which was  $-61.6 \pm 3.2$  mV in DI water (Table 4.1). The negative charge on the NP surface is related with the carboxyl group from 2-carboxyethyl acrylate (CEA, 8 mole% in NPs). Additionally, we compared the  $^1\text{H}$  NMR spectra of co(CEA-AA) NPs (8 mole%) and those without CEA. Compared to that of NPs without CEA, a strong peak at 4.25 ppm appeared on the  $^1\text{H}$  NMR spectrum of co(CEA-AA) NPs (Figure 4.1), which also demonstrates the incorporation of CEA into the NPs.

Table 4.1 Size and zeta potential of NPs, azide-NPs and F3-targeted NPs from DLS

	<b>NPs</b>	<b>Aizde-NPs</b>	<b>F3-targeted NPs</b>
Size in PBS/nm	$57.5 \pm 0.1$	$45.5 \pm 0.7$	$48.5 \pm 1.6$
Zeta potential/mV	$-61.6 \pm 3.2$	$-53 \pm 5.1$	$-50.5 \pm 5.4$

### Synthesis of alkyne-F3 peptide

F3 peptide binds to the angiogenic tumor vasculatures and certain tumor cells, by binding with nucleolin, a cell surface receptor.[22, 23] It has been previously attached on NPs successfully, for active targeting of tumor cells and tumor endothelial cells, both *in vitro* and *in vivo*. [11, 14, 20] Aimed at conjugating the F3 peptide on co(CEA-AA) NPs via click chemistry, attachment of alkyne group onto the peptide is a crucial step. Cysteine

(Cys) is attached at one end of the F3 peptide, which is used for the modification of the peptide. Via reaction with the Cys on the peptide, the alkyne group was attached onto the peptide. Since this is the only Cys on the peptide, we can avoid any side reaction. The sulfur group of the Cys of the F3 peptide reacted with the maleimide group from compound 2, resulting in the attachment of the alkyne group onto the F3 peptide (Scheme 4.1(b)). To prevent the formation of a disulfide bond between F3 molecules, tris(2-carboxyethyl)phosphine (TCEP) was used as a reducing agent. The attachment of the alkyne group onto the F3 peptide was confirmed with the results from both Mass spectrometry and Ultra Performance Liquid Chromatography (UPLC). The Mass spectrometry results of F3 peptide (Figure 4.2(a)) showed a main peak at 3536.0 m/z, which matches the calculated molecular weight of the F3 peptide (3536). Moreover, the Mass Spectrometry of the alkyne-F3 peptide showed a single peak at 3671.0 m/z (Figure 2(b)), which is exactly the same as expected. In addition, HPLC results (Figure 4.3) demonstrated a single peak of alkyne-F3, which is completely separated from that of the F3 peptide, indicating the high purity of the product (alkyne-F3). These results confirmed the successful conjugation of an alkyne group onto the F3 peptide.



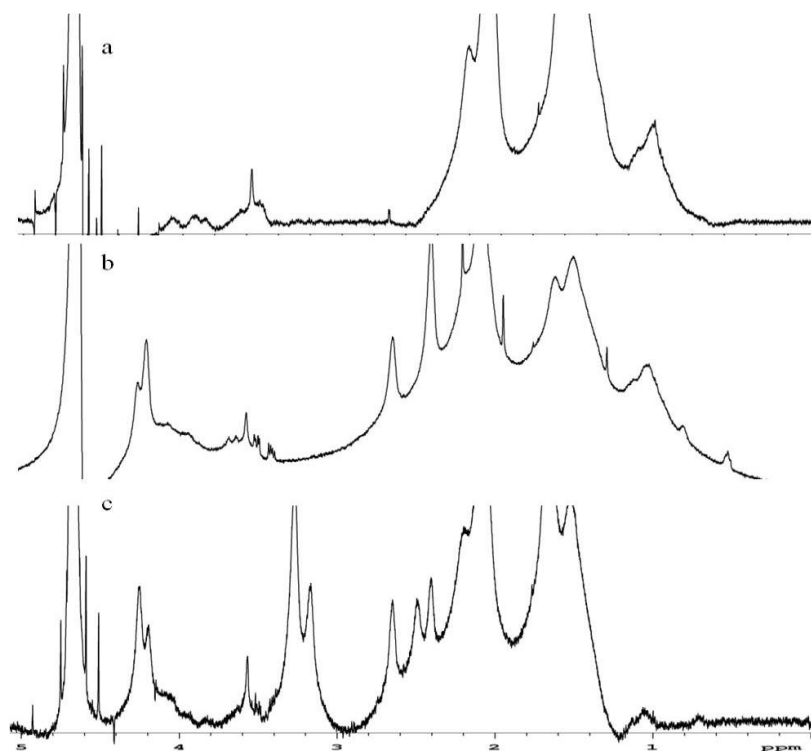


Figure 4.1 <sup>1</sup>H NMR spectra of PAA NPs (a), co(CEA-AA) NPs (b) and azide-functional co(CEA-AA) NPs (c).

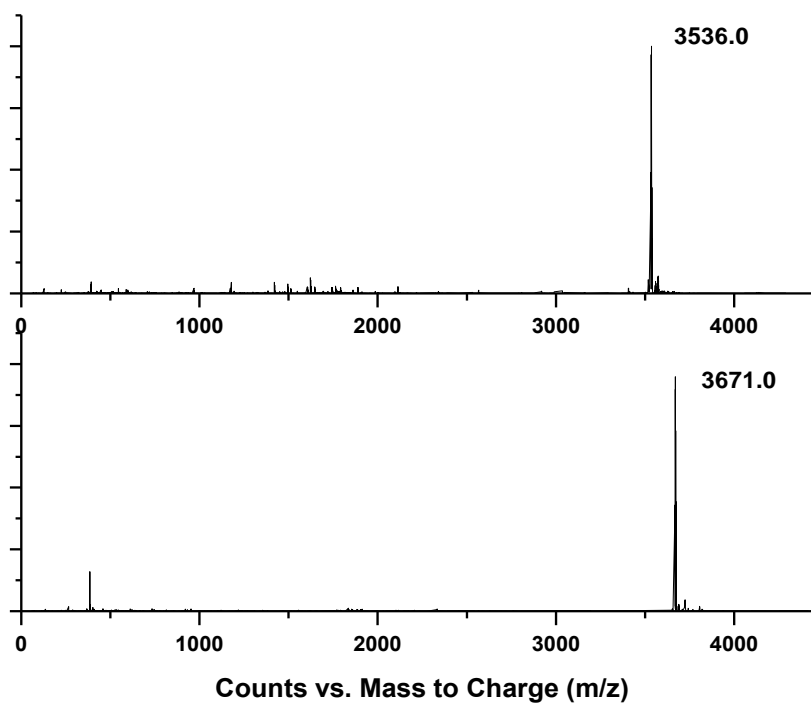


Figure 4.2 (a) Mass spectra of F3 peptide (on the top) and alkyne-F3 peptide (on the bottom)

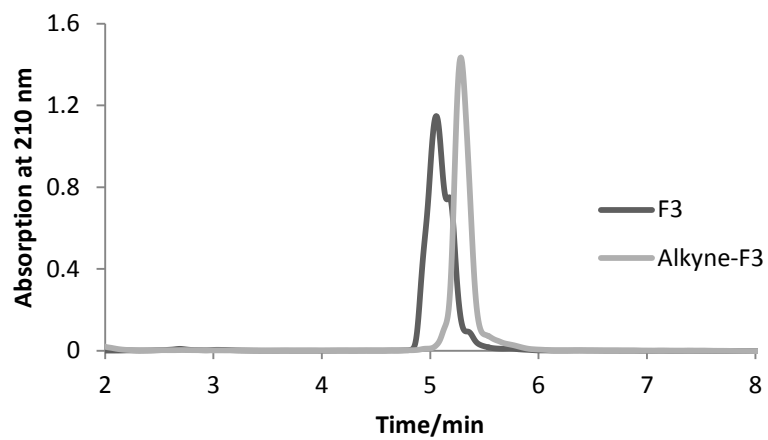


Figure 4.3 HPLC results of F3 and alkyne-F3

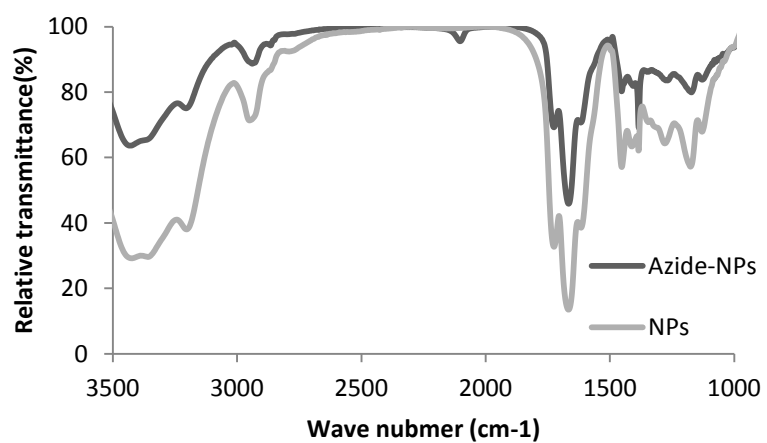


Figure 4.4 FTIR spectra of NPs and azide-NPs

### **Click conjugation of alkyne-F3 peptide onto co(CEA-AA) NPs**

Precise conjugation of F3 peptide onto NPs avoids unexpected side reactions, which is critical for keeping its binding affinity. Towards the conjugation of alkyne-F3 onto the NPs, a functionalization of the NPs with azide is necessary. The attachment of azide was done via the carbodiimide reaction, between amine group from azido-3-aminopropane and carboxyl group on the NPs, with EDC/sulfo-NHS as a crosslinker. The successful attachment of azide group onto the NPs was confirmed by the results from FTIR spectra (Figure 4.4) and  $^1\text{H}$  NMR spectra (Figure 4.4). In the spectra of both NPs and azide-NPs (Figure 4.3), we observed the signals of the  $\text{NH}_2$  group from the amide at  $3500\text{-}3300\text{ cm}^{-1}$  and the alkyl group at  $2950\text{-}2850\text{ cm}^{-1}$ . In addition, a strong absorption at  $1600\text{ cm}^{-1}$  to  $1800\text{ cm}^{-1}$  is related to the mixed signals of carbonyl groups from the amide, carboxylic acid and ester. Compared to that of blank NPs, a clear peak at  $2100\text{ cm}^{-1}$  was found in the spectrum of azide-NPs, which is exactly the absorption of the azide group.[29, 30] This result confirmed the attachment of an azide group onto the co(CEA-AA) NPs. The successful preparation of azide-NPs was also supported from the  $^1\text{H}$  NMR spectrum results. After conjugation with the azide group, two new peaks appeared at 3.2 ppm and 3.3 ppm, on the NMR spectra of the azide-NPs (Figure 4.1).

We conjugated the azide-NPs with the alkyne-F3 peptide click chemistry method, at room temperature, with copper (I) as catalyst. The presence of F3 peptide is confirmed with quantitative amino acid analysis (QAAA), which showed that the amount of F3 peptide on the NPs was 1.66 wt% after conjugation. To our knowledge,

this is the first report on F3 peptide being conjugated onto NPs via click chemistry. The conjugation of alkyne-F3 onto the azide-NPs via click chemistry is also stereospecific. Because click chemistry is modular, this conjugation method may be applied to the attachment of F3 peptide onto other kinds of NPs. Additionally, the azide-NPs were also labeled with an alkyne-functionalized fluorescence dye (AF488) via click chemistry, successfully, with which the intracellular location of NPs can be tracked by confocal microscopy.

DLS studies on the unmodified NPs, azide-NPs and F3-NPs (Table 4.1), demonstrated that the attachment of both the azide group and the F3 peptide did not significantly affect the size of NPs ( $57.5 \pm 0.1$  nm,  $45.5 \pm 0.7$  nm and  $48.5 \pm 1.6$  nm, respectively). Compared to the unmodified NPs ( $-61.6 \pm 3.2$  mV), the zeta potential of the azide-NPs and F3-NPs was  $-53 \pm 5.1$  mV and  $-50.5 \pm 5.4$  mV, respectively. The less negative charge of the modified NPs may be related to (i) part of the carboxyl groups on the NP surface is used for the conjugation of azide groups and (ii) the attachment of the positively charged F3 peptide.[14]

### **Loading and release of Dox from F3-targeted NPs**

The hydrophobic chemotherapy drug, doxorubicin, was loaded onto F3-targeted NPs via post-loading. Dox was loaded onto both unmodified NPs and F3-targeted NPs effectively, with loadings of  $8.68 \pm 0.16\%$  and  $8.48 \pm 0.15\%$ , respectively. These results show that the attachment of F3 peptide does not affect the ability of the NPs as a drug carrier. We also studied the releasing kinetics of Dox from both nontargeted NPs and F3-targeted NPs, in PBS buffer. The results (Figure 4.5) show that that the release

behavior of Dox from F3-NPs was similar to that from nontargeted NPs. These results demonstrated the effective loading and slow releasing of Dox from F3-targeted NPs, suggesting its potential as a drug delivery vehicle.

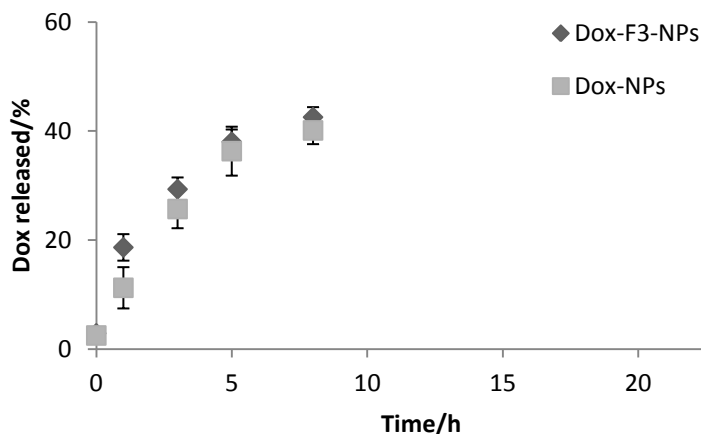


Figure 4.5 Release profile of Dox from unmodified NPs and F3-targeted NPs in PBS buffer. NP concentration: 0.2 mg/ml; Temperature: 37 °C; Loading of Dox/NPs: 8.68±0.16 wt%; loading of Dox/F3-NPs: 8.48±0.15 wt%.

### **Uptake of F3-targeted NPs and nontargeted NPs by tumor cells: 9L, MCF-7 and NCI/ADR-RES**

One important property of a targeted drug delivery vehicle is its ability to selectively accumulate inside tumor cells. Confocal microscopy was used to evaluate the uptake of F3-targeted NPs by tumor cells, and azide-NPs were used as a control. Both kinds of NPs were labeled with AF488 (green). The glioma cell line 9L was chosen due to its relatively high surface expression of nucleolin; and the human breast cancer cell line MCF was selected as an example with relatively low expression of nucleolin.[31] Additionally, in order to study the potential of F3-targeted NPs to deliver drugs to

MDR cells, their uptake by the human ovarian adenocarcinoma cell line NCI/ADR-RES was also studied, which is well known to be Dox-resistant. [31, 32]

Figure 4.6 shows the confocal microscopy images of 9L, MCF-7 and NCI/ADR-RES cells after incubation with nontargeted NPs and with F3-targeted NPs, where the cell nucleus was stained with DAPI (blue). Results showed a minimal nonspecific internalization of the nontargeted NPs into the 9L, MCF-7 and NCI/ADR-RES cells. The attachment of F3 peptide greatly enhances the uptake of NPs into the 9L cells. The fluorescence-labeled F3-NPs are seen to be mainly located in the perinuclear region of the 9L cells, demonstrating their successful internalization into the cytoplasm. Notably, the hydrogel NPs cannot accumulate inside the nucleus because of their large size.[31] The F3-targeted NPs also show improved uptake by the MCF-7 cells, compared to nontargeted NPs. The majority of the F3-targeted NP signal was found on the membrane of MCF-7 cells, suggesting incomplete internalization into the cytoplasm. Considering the difference in nucleolin surface-expression between the 9L and MCF-7, these results are consistent with the hypothesis that the uptake of F3-targeted NPs by tumor cells is nucleolin-mediated. Notably, the surface decoration with F3 peptide also significantly enhanced the uptake of NPs by the drug-resistant NCI/ADR-RES cells, where the NPs are found to be located both on the cell membrane and in the cytoplasm area. As far as we know, this is the first observation that F3 peptide improves the uptake of NPs by a drug-resistant cell line. This improved uptake may again be related with the overexpression of nucleolin on the NCI/ADR-RES cell surface. These results suggest that the F3-targeted NPs may bypass the P-glycoprotein pathway (drug efflux pump), demonstrating its potential as

a targeted drug delivery vehicle for drug-resistant cells.

We analyzed quantitatively the intracellular signals of nontargeted NPs and F3-targeted NPs (see Figure 4.6). The results (Table 4.2) show that the signals of F3-targeted NPs are 20 times higher in 9L cells, 10 times higher in MCF-7 cells and 15 times higher in NCI/ADR-RES cells, compared to those of the nontargeted NPs. Overall, the use of F3 for NP targeting is highly efficient in nucleolin-expressing cancer cells. The relevant pathways also prevent high NP accumulation in the lysosomes.[24]

Generally, the uptake of anionic NPs by tumor cells is challenging, because such NPs cannot easily penetrate the negatively charged cell membrane. Several kinds of anionic NPs were reported previously to enter cells effectively. For example, spherical nucleic acids (zeta potential < -30 mV) were found to enter many kinds of cells effectively, which is believed to be related with scavenger receptors at the cell surface.[33] Active targeting, with a tumor-targeting ligand, can also improve the intracellular uptake of anionic NPs. It is reported that the attachment of folate improved the uptake of negatively charged polyacrylacid-iron oxide NPs by A549 lung cancer cells, on which the folate receptor is overexpressed.[27] Our findings here provide another avenue to improve on the uptake of anionic NPs by tumor cells.

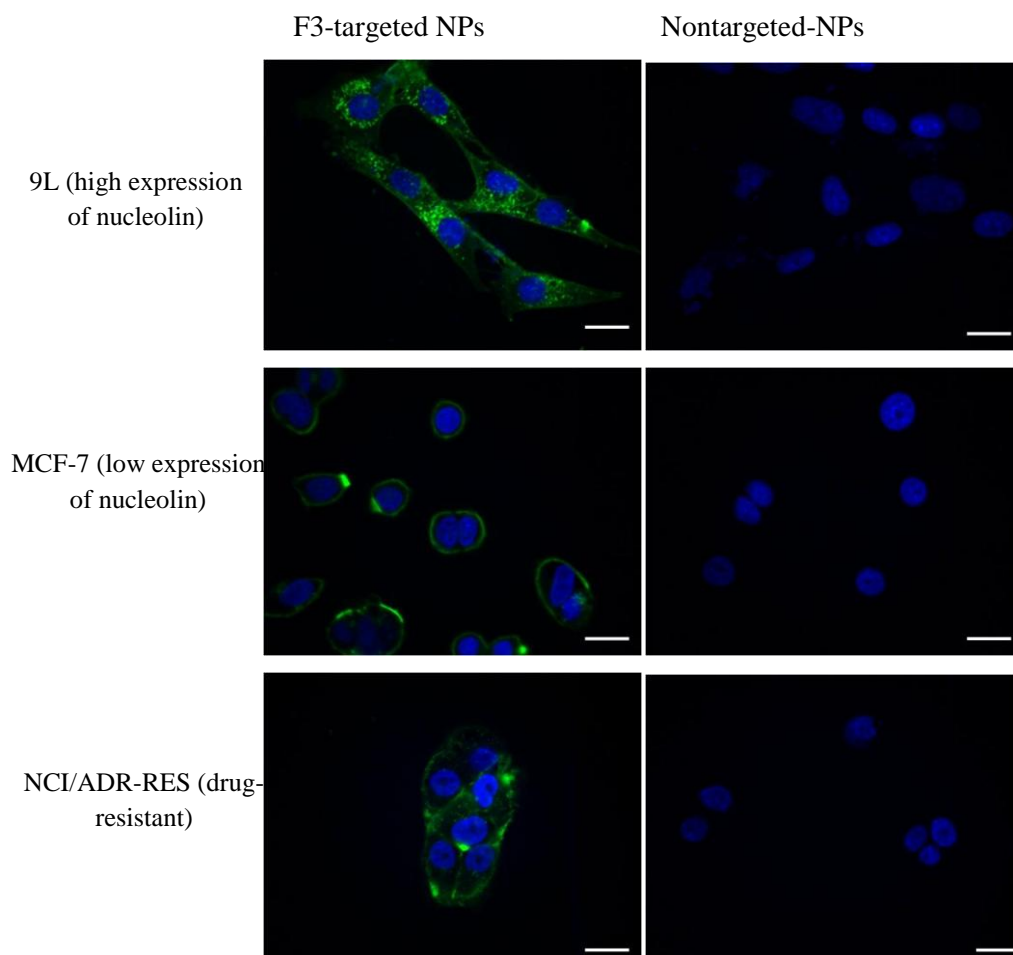


Figure 4.6 Confocal microscopy images of 9L, MCF-7 and NCI/ADR-RES cells after incubation with F3-targeted NPs and nontargeted NPs for 2 h respectively. NPs were labeled with Fluor 488 (green), while the cell nucleus was stained with DAPI (blue). NP concentration: 1.0 mg/ml. scale bar: 25  $\mu$ m.

Table 4.2 Pixel intensity analyses of Fluorescence microscopy images of 9L, MCF-7 and NCI/ADR-RES cells after incubation with nontargeted-NPs or F3-targeted NPs for 2 h. NPs were labeled with Fluor 488.

Sample	9L	MCF-7	NCI/ADR-RES
Nontargeted-NPs	1.9 $\pm$ 0.7	0.8 $\pm$ 0.2	2.0 $\pm$ 1.8
F3-targeted NPs	43.0 $\pm$ 10.8	9.9 $\pm$ 3.6	30.3 $\pm$ 11.8



### **Uptake of F3-targeted NPs via receptor-mediated endocytosis and a blocking test**

We assume that the improved uptake of F3-targeted NPs by tumor cells, such as 9L, is related with receptor-mediated endocytosis. Nucleolin is the cell surface receptor for the F3 peptide.[13, 24] To test this hypothesis, we studied the competitive uptake by 9L cells of F3 peptide vs. F3-targeted NPs. After incubation with varying concentrations of F3 peptide for 30 min, the cells were incubated with AF488-labeled F3-NPs (1 mg/ml) for another 2 h. The results (Figure 4.7) show that the fluorescence intensity of F3-targeted NPs decreases with increasing concentration of F3 peptide. The fluorescence intensity of F3-targeted NPs is limited the most when the F3 peptide concentration is higher than 50  $\mu\text{M}$ . As the concentration of F3 in the F3-targeted NP solution (1 mg/ml) is 4.7  $\mu\text{M}$ , from QAAA analysis, it is not surprising that an over 10 times preponderance of F3 peptide effectively blocks (“saturates”) the receptor-mediated endocytosis process.

We also compared the uptake of F3-targeted NPs and nontargeted NPs by 9L cells at 37  $^{\circ}\text{C}$  and 4  $^{\circ}\text{C}$ , using confocal microscopy. The 9L cells were incubated with the NPs for 2 h, at a given temperature, before conducting the microscopy study. The results (Figure 4.8) showed that the nontargeted NPs exhibited minimal uptake by 9L cells at both 37  $^{\circ}\text{C}$  and 4  $^{\circ}\text{C}$ , suggesting that temperature does not affect much the *nonspecific* uptake of nontargeted NPs. On the other hand, the signal of F3-targeted NPs after incubation at 4  $^{\circ}\text{C}$  is approximately three times lower than that at 37  $^{\circ}\text{C}$ , suggesting that the uptake of F3-targeted NPs is energy-dependent, which is a distinct property of receptor-mediated endocytosis.[22] These results support our assumption

that the uptake of F3-targeted NPs by 9L cells is mainly via nucleolin-mediated endocytosis.

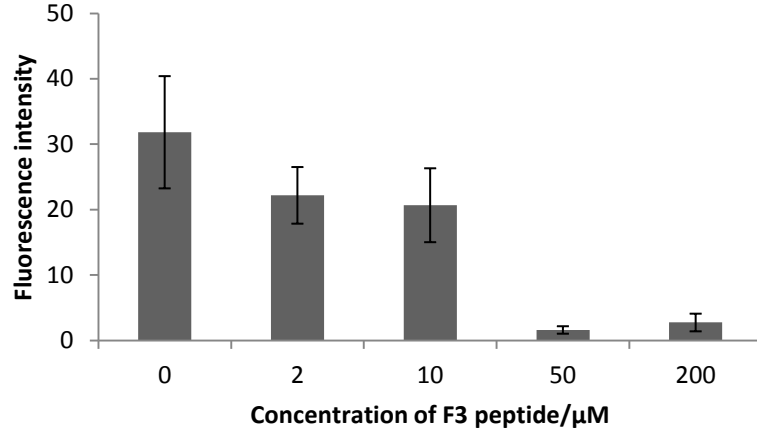


Figure 4.7 Blocking (“saturation”) effect of free F3 peptide on nucleolin sites, preventing cell-incorporation of F3-NPs. Pixel intensity analyses of confocal microscopy images of 9L cells. The cells were incubated with varying concentration of F3 peptide for 30 min, after that the cells were incubated with F3-NPs (1 mg/ml) for 2 h. NPs were labeled with Fluor 488. The results showed that with increasing concentration of F3 peptide, the binding of F3-targeted NPs to 9L cells was inhibited significantly. NP concentration: 1.0 mg/ml.

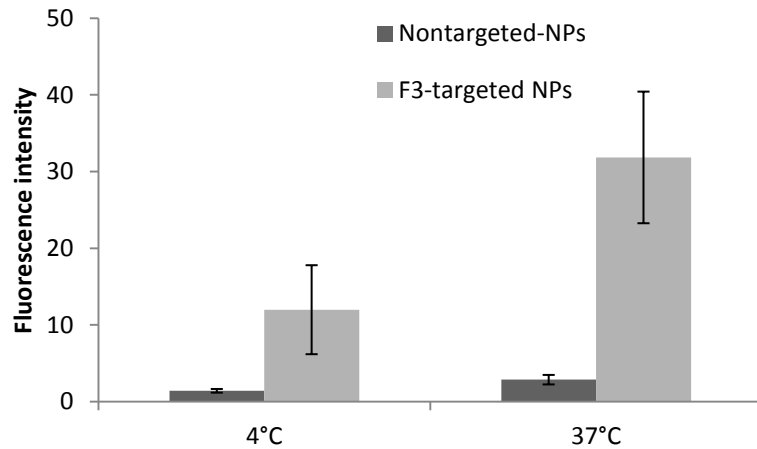


Figure 4.8 Pixel intensity analyses of confocal microscopy images of 9L cells after incubation with F3-targeted NPs (1 mg/ml) or nontargeted-NPs for 2 h at 4 °C or 37 °C. NPs were labeled with Fluor 488. The results showed that the uptake of F3-targeted NPs into 9L cells was affected by the incubation temperature, which may be an energy-dependent process. NP concentration: 1.0 mg/ml.

### ***In vitro* cytotoxicity to 9L cells of Dox-loaded F3-targeted NPs**

The *in vitro* cytotoxicity to 9L cells of Dox-NPs and Dox-F3-NPs was evaluated with an MTT assay (Figure 4.9). The concentration of Dox was either 0.5  $\mu\text{M}$  or 2  $\mu\text{M}$ . When the concentration of Dox was 0.5  $\mu\text{M}$ , 86% and 67% of cells survived after incubation with Dox-NPs and Dox-F3-NPs, respectively; however, at a Dox concentration of 2  $\mu\text{M}$ , only 20% and 16% of the cells survived, after incubation with Dox-NPs and Dox-F3-NPs, respectively (Figure 4.9). These results demonstrate for Dox-F3-NPs a marginally better cell-killing efficiency than for Dox-NPs. In contrast, the “blank”, drug-free NPs, including both nontargeted NPs and F3-targeted NPs, were not toxic to 9L cells (Figure 4.10). We also tested the cytotoxicity of Dox-NPs and Dox-F3-NPs to NCI/ADR-RES cells. These results show that Dox-F3-NPs express similar or stronger cytotoxicity to NCI/ADR-RES cells than the Dox-NPs, when the Dox concentration ranges from 10  $\mu\text{M}$ , or 20  $\mu\text{M}$  to 40  $\mu\text{M}$  (Figure 4.11). As a contrast, after incubation with nontargeted NPs and F3-NPs, around 95% and 80% cells survived (Figure 4.12). This higher cytotoxicity of Dox-F3-NPs may be related to the improved uptake of the F3-NPs by the high nucleolin expressing cancer cells (9L and NCI/ADR-RES).

### **Discussion and Conclusions**

The development of one kind of peptide-targeted NPs for the targeted delivery of doxorubicin into tumor cell was successful. The cell surface nucleolin-targeting peptide, F3, was successfully conjugated onto co(CEA-AA) NPs via the copper (I) catalyzed “click chemistry. This modular conjugation is efficient and should be

applicable to other kinds of peptide-nanoparticle conjugations. This “precise” conjugation method does not affect the binding activity of the F3 peptide. This binding activity significantly enhances the intracellular uptake of co(CEA-AA) NPs by nucleolin-overexpressing cell lines. This enhanced uptake of F3-targeted NPs appears to be related with the nucleolin-mediated endocytosis. Interestingly, F3-targeted NPs show a much higher uptake by the drug-resistant cell line (NCI/ADR-RES), compared to nontargeted NPs, suggesting that they may bypass the P-glycoprotein efflux pump pathway. It demonstrated the potential of F3-targeted NPs for the treatment of drug-resistant tumors. Surprisingly, the attachment with F3 peptide does not affect much the ability of the NPs to deliver doxorubicin; the targeted, Dox-loaded F3-NPs showed only marginally better *in vitro* cytotoxicity to 9L cells and NCI/ADR-RES cells than non-targeted, Dox-loaded NPs. Our findings suggest that F3-targeted co(CEA-AA) NPs present a promising drug delivery system for further *in vivo* study.

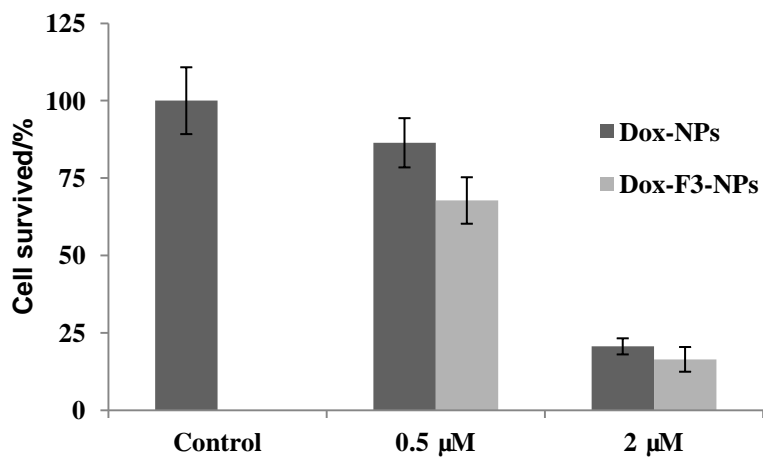


Figure 4.9 Viability of 9L cells after incubation with Dox-NPs and Dox-F3-NPs (loading of Dox/NPs: 2 % wt). The cells were incubated with NPs for 4 h. After that, the medium was replaced and the cells were left to incubate for 48 h. The NP concentration was 0.05 mg/ml, when the Dox concentration was 2  $\mu\text{M}$ .

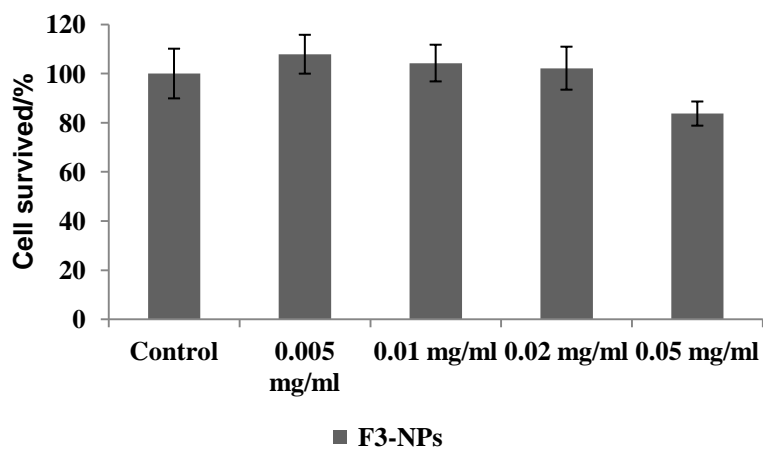


Figure 4.10 Viability of 9L cells after incubation with F3-NPs. The cells were incubated with NPs for 4 h. After that, the medium was replaced and the cells were continued to incubate for 48 h.

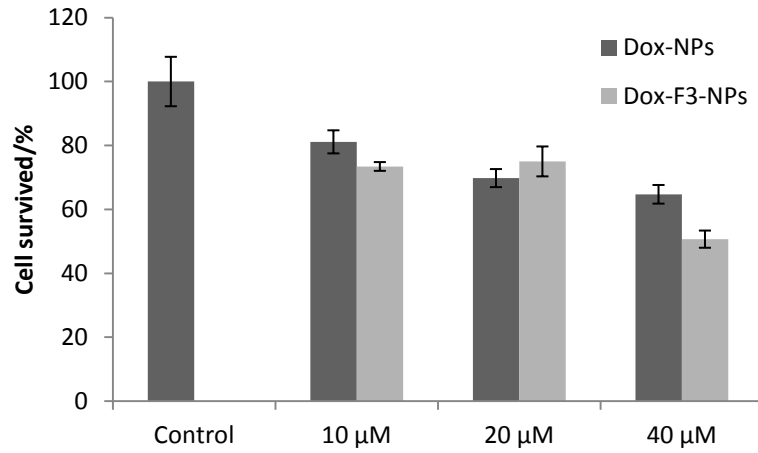


Figure 4.11 Viability of NCI/ADR-RES cells after incubation with Dox-NPs and Dox-F3-NPs (loading of Dox/NPs: 10 % wt). The cells were incubated with NPs for 4 h. After that, the medium was replaced and the cells were left to incubate for 48 h. The NP concentration was 0.1 mg/ml, when the Dox concentration was 20  $\mu$ M.

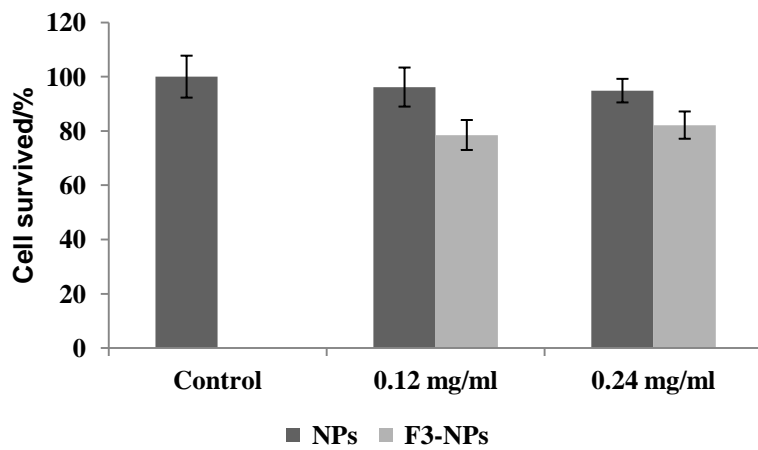


Figure 4.12 Viability of NCI/ADR-RES cells after incubation with nontargeted and F3-targeted NPs. The cells were incubated with NPs for 4 h. After that, the medium was replaced and the cells were continued to incubate for 48 h.

## **Acknowledgements**

The authors would like to thank Dr Martin Philbert and Kristen Russ for allowing us to use the confocal microscope in their lab. The authors thank Leshern Karamchand for his help with the confocal microscopy, and also like to thank Leshern Karamchand and Aniruddha Ray for discussions on the intracellular studies of hydrogel NPs. They thank James Windak and Paul Lennon for their help with Mass Spectrometry and FTIR.

## References

1. Binascchi, M., et al., *Anthracyclines: selected new developments*. *Curr Med Chem Anti-Canc Agents*, 2001. **1**(2): p. 113-130.
2. Rinehart, J.J., R.P. Lewis, and S.P. Balcerzak, *Adriamycin Cardiotoxicity in Man*. *Annals of Internal Medicine*, 1974. **81**(4): p. 475-478.
3. Goldenberg, G.J., H. Wang, and G.W. Blair, *Resistance to Adriamycin: Relationship of cytotoxicity to drug uptake and DNA single- and double-strand breakage in cloned cell lines of Adriamycin-sensitive and -resistant P388 leukemia*. *Cancer Research*, 1986. **46**(6): p. 2978-2983.
4. Davis, M.E., Z. Chen, and D.M. Shin, *Nanoparticle therapeutics: an emerging treatment modality for cancer*. *Nature Reviews Drug Discovery*, 2008. **7**(9): p. 771-782.
5. Lee, Y.-E.K. and R. Kopelman, *Targeted, Multifunctional Hydrogel Nanoparticles for Imaging and Treatment of Cancer: Multifunctional Nanoparticles for Drug Delivery Applications*, S. Svenson and R.K. Prud'homme, Editors. 2012, Springer US. p. 225-255.
6. Maeda, H., et al., *Tumor vascular permeability and the EPR effect in macromolecular therapeutics: a review*. *Journal of Controlled Release*, 2000. **65**(1-2): p. 271-284.
7. Torchilin, V.P., *Recent advances with liposomes as pharmaceutical carriers*. *Nature Reviews Drug Discovery*, 2005. **4**(2): p. 145-160.
8. Duncan, R., *Polymer conjugates as anticancer nanomedicines*. *Nature Reviews Cancer*, 2006. **6**(9): p. 688-701.
9. Koo, Y.E.L., et al., *Brain cancer diagnosis and therapy with nanoplatforms*. *Advanced Drug Delivery Reviews*, 2006. **58**(14): p. 1556-1577.
10. Susa, M., et al., *Doxorubicin loaded Polymeric Nanoparticulate Delivery System to overcome drug resistance in osteosarcoma*. *Bmc Cancer*, 2009. **9**: p. 399.
11. Winer, I., et al., *F3-targeted cisplatin-hydrogel nanoparticles as an effective therapeutic that targets both murine and human ovarian tumor endothelial cells in vivo*. *Cancer Research*, 2010. **70**(21): p. 8674-8683.
12. Ma, P. and R.J. Mumper, *Anthracycline nano-delivery systems to overcome multiple drug resistance: A comprehensive review*. *Nano Today*, 2013. **8**(3): p. 313-331.
13. Reddy, G.R., et al., *Vascular targeted nanoparticles for imaging and treatment of brain tumors*. *Clinical Cancer Research*, 2006. **12**(22): p. 6677-6686.
14. Hah, H.J., et al., *Methylene Blue-Conjugated Hydrogel Nanoparticles and Tumor-Cell Targeted Photodynamic Therapy*. *Macromolecular Bioscience*, 2011. **11**(1): p. 90-99.
15. Nie, G., et al., *Hydrogel Nanoparticles with Covalently Linked Coomassie Blue for Brain Tumor Delineation Visible to the Surgeon*. *Small*, 2012. **8**(6): p. 884-891.
16. Qin, M., et al., *Overcoming Cancer Multidrug Resistance by Codelivery of Doxorubicin and Verapamil with Hydrogel Nanoparticles*. *Macromolecular Bioscience*, 2013. Submitted.
17. Xiao, K., et al., *"OA02" Peptide Facilitates the Precise Targeting of Paclitaxel-Loaded Micellar Nanoparticles to Ovarian Cancer In Vivo*. *Cancer Research*, 2012.
18. von Maltzahn, G., et al., *In Vivo Tumor Cell Targeting with "Click" Nanoparticles*. *Bioconjugate Chemistry*, 2008. **19**(8): p. 1570-1578.
19. Werner, M.E., et al., *Folate-Targeted Polymeric Nanoparticle Formulation of Docetaxel Is an Effective Molecularly Targeted Radiosensitizer with Efficacy Dependent on the Timing of Radiotherapy*. *Acs Nano*, 2011. **5**(11): p. 8990-8998.
20. Hu, Q., et al., *F3 peptide-functionalized PEG-PLA nanoparticles co-administrated with tLyp-1 peptide for anti-glioma drug delivery*. *Biomaterials*, 2013. **34**(4): p. 1135-1145.
21. Yu, B., et al., *Receptor-targeted nanocarriers for therapeutic delivery to cancer*. *Molecular Membrane Biology*, 2010. **27**(7): p. 286-298.
22. Porkka, K., et al., *A fragment of the HMGN2 protein homes to the nuclei of tumor cells and tumor endothelial cells in vivo*. *Proceedings of the National Academy of Sciences of the United States of America*, 2002. **99**(11): p. 7444-7449.



23. Christian, S., et al., *Nucleolin expressed at the cell surface is a marker of endothelial cells in angiogenic blood vessels*. Journal of Cell Biology, 2003. **163**(4): p. 871-878.
24. Karamchand, L., et al., *Modulation of hydrogel nanoparticle intracellular trafficking by multivalent surface engineering with tumor targeting peptide*. Nanoscale, 2013. **5**(21): p. 10327-10344.
25. Qin, M., et al., *Methylene blue covalently loaded polyacrylamide nanoparticles for enhanced tumor-targeted photodynamic therapy*. Photochemical & Photobiological Sciences, 2011. **10**(5): p. 832-841.
26. Le Droumaguet, B. and K. Velonia, *Click Chemistry: A Powerful Tool to Create Polymer-Based Macromolecular Chimeras*. Macromolecular Rapid Communications, 2008. **29**(12-13): p. 1073-1089.
27. Santra, S., et al., *Drug/Dye-Loaded, Multifunctional Iron Oxide Nanoparticles for Combined Targeted Cancer Therapy and Dual Optical/Magnetic Resonance Imaging*. Small, 2009. **5**(16): p. 1862-1868.
28. Carboni, B., A. Benalil, and M. Vaultier, *Aliphatic amino azides as key building blocks for efficient polyamine syntheses*. The Journal of Organic Chemistry, 1993. **58**(14): p. 3736-3741.
29. Martin, A.L., et al., *Enhanced Cell Uptake of Superparamagnetic Iron Oxide Nanoparticles Functionalized with Dendritic Guanidines*. Bioconjugate Chemistry, 2008. **19**(12): p. 2375-2384.
30. Zhang, J., et al., *Synthesis of thermosensitive P(NIPAAm-co-HEMA)/cellulose hydrogels via "click" chemistry*. Carbohydrate Polymers, 2009. **77**(3): p. 583-589.
31. Orringer, D.A., et al., *In vitro characterization of a targeted, dye-loaded nanodevice for intraoperative tumor delineation*. Neurosurgery, 2009. **64**(5): p. 965-971.
32. Wu, L., et al., *Multidrug-resistant Phenotype of Disease-oriented Panels of Human Tumor Cell Lines Used for Anticancer Drug Screening*. Cancer Research, 1992. **52**(11): p. 3029-3034.
33. Cutler, J.I., E. Auyeung, and C.A. Mirkin, *Spherical Nucleic Acids*. Journal of the American Chemical Society, 2012. **134**(3): p. 1376-1391.

## **Chapter 5 Covalent Binding of Coomassie Blue in Polyacrylamide Nanoparticles for *in vivo* Tumor Delineation**

Some of the material in this chapter has been adapted with minor modifications from the following publication:

Hydrogel Nanoparticles with Covalently Linked Coomassie Blue for Brain Tumor Delineation Visible to the Surgeon; Nie, G.; Hah, H. J.; Kim, G.; Lee, Y.-E. K.; Qin, M.; Ratani, T. S.; Fotiadis, P.; Miller, A.; Kochi, A.; Gao, D.; Chen, T.; Orringer, D. A.; Sagher, O.; Philbert, M. A.; Kopelman, R., *Small* 2012, 8 (6), 884-891

### **Introduction**

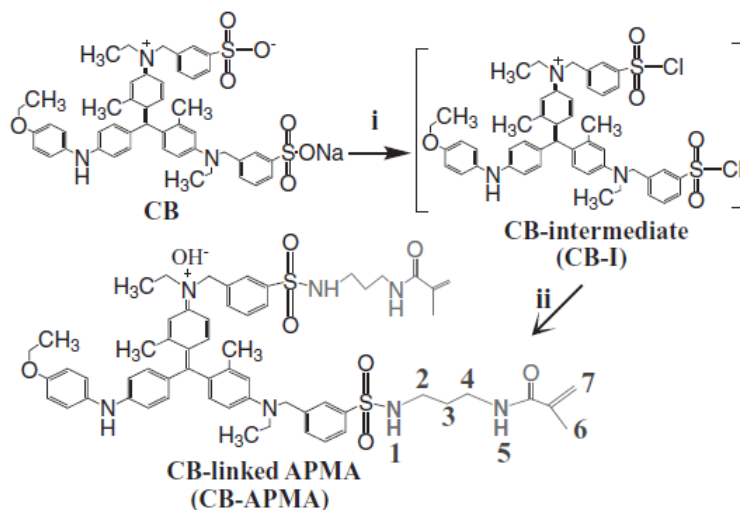
Surgery is the main treatment for brain cancer. During surgery, a complete resection without any damage to the important parts on the neighbor area is a big challenge, which is determined by the precise tumor delineation and the surgeon's ability to distinguish the tumor from the healthy tissue.[1] Medical imaging instrumentation, such as the image-guided stereotactic navigation [2] and intraoperative magnetic resonance imaging (MRI) [3], were widely used for tumor delineation. However, their use was limited to high cost, limited availability, the practicing surgeon's divided attention between patient and monitor, and strong magnetic fields within the operating space of MRI. In addition, fluorophores and visible dyes were also used for the staining of the tumor tissue, e.g. fluorescein,[4] 5-aminolevulinic acid [5, 6] and indocyanine green [7]. These dye-based delineation methods help the surgeons

completely focus on the patient, since the visual contrasting effect comes from the tumor tissue directly. However, these fluorophores and visible dyes lack target specificity and have short retention time at the tumor area.[8] In addition, special lighting is required for fluorescence-based delineation, which may interrupt the surgery.

To overcome the limitations of the dye-based tumor delineation, the use of targeted hydrogel nanoparticles (NPs) has been studied as a dye carrier.[9] Hydrogel NPs can accumulate specifically into tumor area via passive targeting by the enhanced permeability and retention (EPR) effect and active targeting by attachment of tumor-targeting moiety.[10] As a dye carrier, the NPs have the advantages of high loading, good solubility and good biocompatibility. Recently, our group proposed a brain-tumor targeted delineation reagent, based on polyacrylamide (PAA) NPs.[11] Coomassie blue (CB) was post-loaded into PAA NPs as the delineation reagent. CB has a high molar extinction coefficient, and its color is stable in pH 3-11.[12] CB is also known to be safe for intravenous injection into the human body, even at very high doses.[13] The results showed that F3 peptide-targeted, CB-loaded NPs cause definitive color change in glioma cells *in vitro*. However, the CB-loaded NPs also produced a rather high degree of nonspecific staining because of the leaching of CB from NPs, which may lead to inefficient specific tumor staining *in vivo*. [11]

To overcome these drawbacks, we report CB-covalently linked PAA NPs for brain tumor delineation. CB derivative was developed by Guochao Nie in our group (Scheme 1), [14] which can be incorporated into NPs via free radical polymerization.

The CB-linked NPs was prepared in a reverse microemulsion system. Compared to that of blank NPs, the synthesis procedure of CB-linked NPs was modified significantly to achieve sufficient dye loading. The NPs were modified with polyethylene glycol(PEG) to improve their stability in blood plasma and prevent nonspecific binding. For brain tumor targeting, the NPs were decorated with F3 peptide, which can improve the internalization of NPs into angiogenic tumor vasculatures and nucleolin-expressing tumor cells via interaction with nucleolin on cell surface. The *in vivo* tumor staining experiment of F3-targeted, CB-linked NPs was studied in 9L-bearing rats with a cranial window, with nontargeted CB-linked PAA NPs as a control.



Scheme 5.1 Synthesis of CB-APMA [14]

## Experimental

### Materials

Coomassie Blue G (CB), acrylamide (AA), glycerol dimethacrylate (GDMA),

ammonium persulfate (APS), N', N', N', N'-tetramethylethylenediamine (TEMED), sodium dioctyl sulfosuccinate (AOT), Brij 30, hexane, N, N-dimethylformamide (DMF), dimethyl sulfoxide (DMSO), L-cysteine and phosphate-buffered saline tablet from Sigma Aldrich. N-(3-Aminopropyl)methacrylamide hydrochloride (APMA) was purchased from Polysciences Inc. Ethanol (95%) and hexane were purchased from Fisher Sci. F3-Cys peptide (KDEPQRRSARLSAKPAPPKPEPKPKKAPAKKC) was purchased from SynBioSci. A heterobifunctional polyethylene glycol (MALPEG-NHS, 2k) was purchased from Creative PEGWorks. Coomassie blue derivative (CB-APMA) was synthesized in our group. The water used throughout the experiments was deionized (DI) water, purified by a Milli-Q system from Millipore Co.

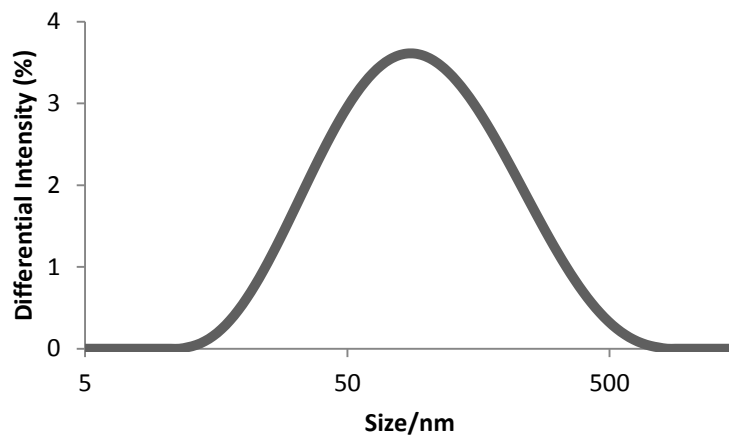
#### **Preparation of CB-linked PAA NPs**

CB-linked PAA NPs were prepared by a reverse microemulsion polymerization method. A monomer solution was prepared by dissolving acrylamide (610 mg) and APMA (45 mg) in water (1 ml). A dye solution was prepared by dissolving CB-APMA (100 mg) in DMF (0.4 mL) and then GDMA (360  $\mu$ l) was added to the dye solution. The monomer solution was added to the mixture and then it was stirred and sonicated to make a homogeneous solution. The prepared CB-containing monomer solution was added to deoxygenated hexane (120 ml) that contained two surfactants, AOT (3.9 g) and Brij 30 (10.3 ml). After stirring the mixture under an inert atmosphere for 20 min, a freshly prepared 50% (w/v) APS solution (240  $\mu$ l) and TEMED (150  $\mu$ l) were added to initiate polymerization. The solution was then stirred under an inert atmosphere at room temperature for 1 h. After completion of the

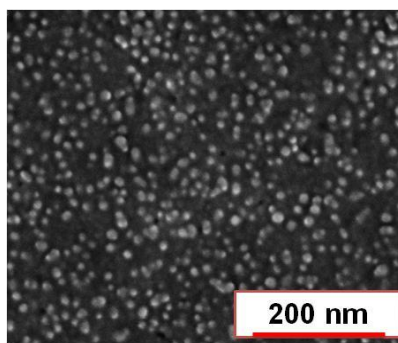
polymerization, hexane was removed with a rotary evaporator and the residue was made into a suspension by adding ethanol. The suspension was subjected to a washing procedure in an Amicon filtration system (Millipore Co.) with a 500 kDa filter membrane under 10–20 psi of pressure. The washing procedure was carried out with ethanol ten times and with water ten times, during which surfactants and free monomers were removed from the product. The resultant CB-linked NPs were freeze dried and stored at -20 °C.

### **Preparation of F3-targeted CB-loaded PAA NPs**

CB-linked PAA NPs (50 mg) were dissolved in PBS (2.5 ml, pH 7.4). NHS-PEG-MAL (4 mg), a bifunctional conjugating polyethylene glycol, was added to the NP solution and the mixture was stirred for 30 min. The NPs were washed with PBS buffer in an Amicon centrifugal filter (Millipore, 100 kDa) by centrifugation at 4000 g for 20 min. This washing procedure was repeated three times. After that, the NPs were dissolved in PBS at 20 mg/ml, and F3-Cys peptide (2 μmol) was added. The mixture was stirred overnight at room temperature. L-Cysteine aqueous solution (63 μl, 10 mg/ml) was added and the mixture was stirred for 2 h to deactivate the unreacted PEG molecules. The F3-targeted CB-linked PAA NPs were obtained after additional washing with repetitive centrifugation.



(a)



(b)

Figure 5.1 (a) Size distribution of CB-PAA NPs from dynamic light scattering; (b) SEM image of CB-PAA NPs.

### Preparation of nontargeted CB-loaded PAA NPs

CB-linked PAA NPs (50 mg) were dissolved in PBS (2.5 ml, pH 7.4). NHS-PEG-MAL (4 mg), a bifunctional conjugating polyethylene glycol, was added to the NP solution and the mixture was stirred for 30 min. The NPs were washed with PBS buffer in an Amicon centrifugal filter (Millipore, 100 kDa) by centrifugation at 4000 g for 20 min. This washing procedure was repeated three times. The NP solution was collected with a concentration of 20 mg/ml. L-cysteine aqueous solution (125  $\mu$ l, 10 mg/ml) was added and the mixture was stirred for 2 h. The resultant nontargeted CB-

loaded PAA NPs were obtained after additional washing with repetitive centrifugation.

### ***In vivo* tumor delineation study**

The *in vivo* tumor delineation was performed in a rat brain tumor model that was prepared as previously described.[15] Briefly, biparietal craniectomies were performed on 8-week-old Sprague-Dawley rats. 9L glioma cells were injected intraparenchymally. A coverslip was bonded to the cranial defect with cyanoacrylate glue. When the tumor radius reached 1-2 mm, CB-linked NPs were administered intravenously while the appearance of the cortical surface was recorded.

## **Results and discussion**

### **Preparation and characterization of CB-linked PAA NPs**

CB-linked PAA NPs were prepared by reverse microemulsion polymerization. The monomers include CB-APMA, acrylamide (monomer), APMA (amine-functional monomer), and glycerol dimethacrylate (GDMA, crosslinker). The amine group from APMA can be used for NP modification. The prepared NPs were biodegradable *in vivo*, because the crosslinker (GDMA) contains hydrolysable ester bonds.[10, 16] The synthesis method of CB-linked PAA NPs was significantly modified compared to that of blank PAA NPs. Since the CB-APMA is insoluble in water, the monomer mixtures were dissolved in a mixture of DMF/water. The amount of surfactants was increased three times, in order to keep a stable microemulsion system. In addition, much more amount of initiators (16 times) were required for the initiation of the polymerization,



because the produced radicals may be quenched by the larger amounts of dye and surfactant.

Results from dynamic light scattering (DLS) showed that the average size of CB-linked PAA NPs in water is around 76.3 nm (Figure 5.1(a)). The scanning electron microscopy (SEM) image showed that the CB-linked NPs have spherical particulate morphology and a size of around 20 nm in diameter (Figure 5.1(b)), which is much smaller than the hydrodynamic size of these NPs. This is related with the swelling behavior of hydrogel NPs in aqueous solution.[17]

#### **Attachment of polyethylene glycol and F3 peptide on NPs**

To further improve the accumulation efficiency of CB-linked PAA NPs *in vivo*, the NPs were modified with polyethylene glycol (PEG) and tumor targeting peptide, F3. First, the CB-linked NPs were PEGylated via reaction with the hererobifunctional PEG, SCM-PEG-MAL. The amine-reactive group (SCM) from bifunctional PEG reacted with amine group from the NPs. After that, F3 peptide was conjugated on PEGylated NPs via the reaction between the sulfhydryl-reactive group (MAL) from PEG and the sulfhydryl group from F3-Cys. The attachment of F3 peptide on NPs was confirmed with the results from quantitative amino acid assays, which showed that the amount of F3 peptide/NPs was 0.027  $\mu\text{mol}/\text{mg}$  of NP. Both surface modification steps were confirmed by the change of zeta potential on NP surface indirectly. Unmodified NPs exhibited a relatively strong positive charge ( $+17.38 \pm 3.30$  mV in zeta potential) due to the presence of protonated amine groups on the surface. After PEGylation, the zeta potential of NPs reduces to  $2.98 \pm 1.40$  mV. The F3-conjugated NPs regained a

net positive surface charge ( $+15.11 \pm 2.36$  mV) because of the strong basic amino acid composition of the F3 peptide.

### Quantification of dye loading efficiency

The loading of CB/NPs was calculated based on its absorption. The CB-linked NPs in aqueous solution showed that their absorption maximum was at 610 nm (Figure 5.2), which is slightly different from that of the free dye (597 nm). The peak shift does not cause significant color changes and affect the delineation affect. The loading efficiency of CB in NPs was high (7 wt%) and tunable by changing the input amount of CB-APMA. A CB loading of up to 14 wt% was achieved for the CB-linked NPs.

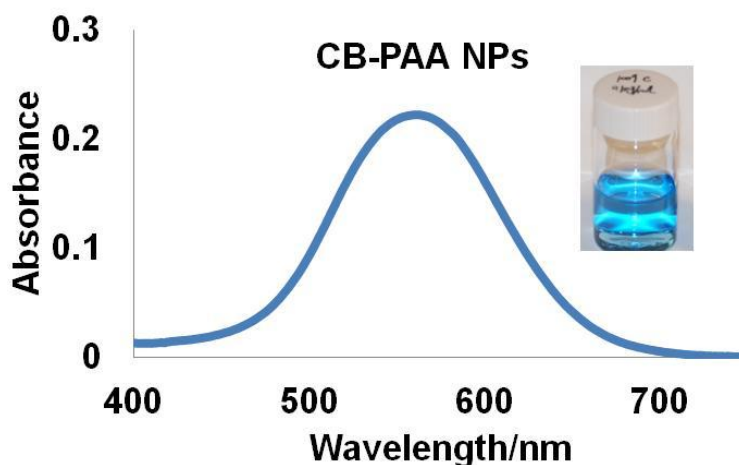


Figure 5.2 UV-*vis* absorption spectrum of CB-PAA NPs in DI water (0.1 mg/ml)

### *In vivo* tumor delineation

An *in vivo* tumor delineation study was performed in a rat BTW model, which is rats with implanted 9L gliosarcoma and with a glass cranial window. Through the window, the *in vivo* tumor delineation was evaluated in real time by visual observation.[11] Figure 5.3 showed representative pictures of the tumors in the BTW

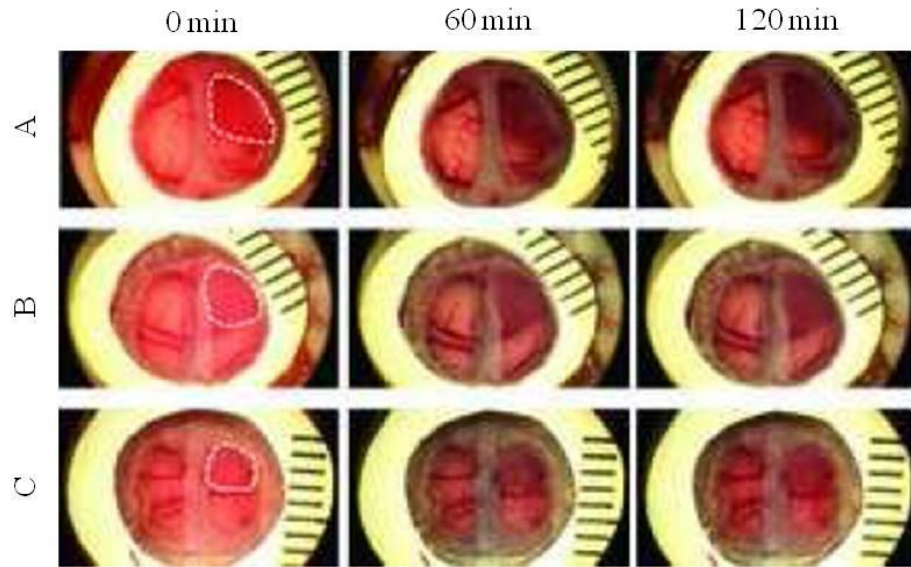
models at 0, 60, and 120 min after injection of F3-targeted and nontargeted CB-linked PAA NPs. The NP dose was at 500 mg/kg. The tumor margin was unclear before administration of the NPs. However, the margin became readily apparent after administration of nontargeted CB-linked NPs. The enhanced accumulation of nontargeted NPs in brain tumor area may be related with passive targeting by the EPR effect.

The visual delineation effect induced by the F3-targeted NPs was stronger than that by the nontargeted NPs, suggesting their stronger ability of tumor delineation. This enhancement can be attributed to the additive effects of active targeting by the F3 peptide. These results clearly demonstrated the advantage of F3-targeted CB-linked NPs for tumor-selective delineation.

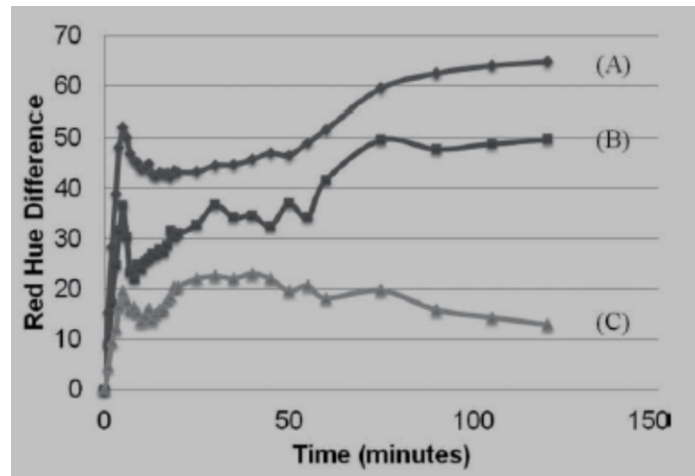
## **Conclusion**

We have demonstrated the development of tumor-targeted, intensely blue colored NP agents for tumor-specific visible color contrast, designed to aid in intraoperative tumor margin delineation. The color contrast agent is made of CB-linked PAA hydrogel NPs, via the copolymerization of CB-derivative and acrylamide. The CB-linked PAA NPs is stable in aqueous solutions and can avoid leaching of the color contrast ingredient. The conjugation of PEG and F3 peptide enable efficient and long-term *in vivo* tumor targeting of the NPs. Their selective and visible tumor staining ability was confirmed in a 9L tumor-bearing rat model (*in vivo*). The tumor-targeting blue colored NP agents are likely to enable color-guided tumor resection in real time, without the need for extra equipment, special lighting conditions, or surgery

interruptions.



(a)



(b)

Figure 5.3 (a) Photographs of representative tumors in BTW models, at 0, 60, and 120 min after injection of F3-targeted CB-linked NPs (A), nontargeted CB-linked NPs (B) and nontargeted CB-loaded NPs (C). The tumor margin in each animal was marked by a white dashed line on the initial (0 min) images. (b) Colorimetric analysis results with ImageJ, to quantify the degree of color change in the tumor. The difference in red hue is the best method to reflect the visual difference between tumor and normal brain tissue.

## **Acknowledgements**

This work was supported by NIH/NIBIB "Quantum Leap Grant" 1R01 EB007977 (RK) and NIH R33CA125297 (RK). The authors would like to thank the staff of the Electron Microscopy Analysis Laboratory of the University of Michigan.

## References

1. Rogers, L., et al., *Is gross-total resection sufficient treatment for posterior fossa ependymomas?* Journal of Neurosurgery, 2005. **102**(4): p. 629-636.
2. Willems, P.W.A., et al., *Effectiveness of neuronavigation in resecting solitary intracerebral contrast-enhancing tumors: a randomized controlled trial.* Journal of Neurosurgery, 2006. **104**(3): p. 360-368.
3. Nimsky, C., et al., *Intraoperative magnetic resonance imaging combined with neuronavigation: A new concept.* Neurosurgery, 2001. **48**(5): p. 1082-1089.
4. Shinoda, J., et al., *Fluorescence-guided resection of glioblastoma multiforme, by using high-dose fluorescein sodium - Technical note.* Journal of Neurosurgery, 2003. **99**(3): p. 597-603.
5. Stummer, W., et al., *Intraoperative detection of malignant gliomas by 5-aminolevulinic acid-induced porphyrin fluorescence.* Neurosurgery, 1998. **42**(3): p. 518-525.
6. Stummer, W., et al., *Fluorescence-guided resection of glioblastoma multiforme by using 5-aminolevulinic acid-induced porphyrins: a prospective study in 52 consecutive patients.* Journal of Neurosurgery, 2000. **93**(6): p. 1003-1013.
7. Britz, G.W., et al., *Intracarotid RMP-7 enhanced indocyanine green staining of tumors in a rat glioma model.* Journal of Neuro-Oncology, 2002. **56**(3): p. 227-232.
8. Hansen, D.A., et al., *INDOCYANINE GREEN (ICG) STAINING AND DEMARCATION OF TUMOR MARGINS IN A RAT GLIOMA MODEL.* Surgical Neurology, 1993. **40**(6): p. 451-456.
9. Reddy, G.R., et al., *Vascular targeted nanoparticles for imaging and treatment of brain tumors.* Clinical Cancer Research, 2006. **12**(22): p. 6677-6686.
10. Koo, Y.E.L., et al., *Brain cancer diagnosis and therapy with nanoplateforms.* Advanced Drug Delivery Reviews, 2006. **58**(14): p. 1556-1577.
11. Orringer, D.A., et al., *IN VITRO CHARACTERIZATION OF A TARGETED, DYE-LOADED NANODEVICE FOR INTRAOPERATIVE TUMOR DELINEATION.* Neurosurgery, 2009. **64**(5): p. 965-971.
12. Chial, H.J., H.B. Thompson, and A.G. Splittgerber, *A SPECTRAL STUDY OF THE CHARGE FORMS OF COOMASSIE BLUE-G.* Analytical Biochemistry, 1993. **209**(2): p. 258-266.
13. Taylor, S.H. and J.P. Shillingford, *Clinical Applications of Coomassie Blue.* British Heart Journal, 1958. **21**(4): p. 8.
14. Nie, G., et al., *Hydrogel Nanoparticles with Covalently Linked Coomassie Blue for Brain Tumor Delineation Visible to the Surgeon.* Small, 2012. **8**(6): p. 884-891.
15. Ozawa, T., et al., *Bromophenol blue staining of tumors in a rat glioma model.* Neurosurgery, 2005. **57**(5): p. 1041-1046.
16. Holland, S.J., B.J. Tighe, and P.L. Gould, *Polymers for biodegradable medical devices. 1. The potential of polyesters as controlled macromolecular release systems.* Journal of Controlled Release, 1986. **4**(3): p. 155-180.
17. Hah, H.J., et al., *Methylene Blue-Conjugated Hydrogel Nanoparticles and Tumor-Cell Targeted Photodynamic Therapy.* Macromolecular Bioscience, 2011. **11**(1): p. 90-99.

## Chapter 6 Summary and Future Directions

### Summary

Hydrogel NPs showed a great potential for biomedical applications, especially in the drug delivery area. We focused on some important but challenging questions in the drug delivery field, including targeted therapy, codelivery of multiple kinds of drugs, and overcoming multidrug resistance. Extending our previous study on polyacrylamide NPs, we developed several novel kinds of hydrogel NPs for photodynamic therapy,[1] chemotherapy [2] and tumor delineation [3].

In Chapter 2, two novel variants of MB-conjugated PAA NPs were introduced, aimed at targeted photodynamic therapy.[1] Two MB derivatives (MBI and MBII) were incorporated into NPs via free radical polymerization. With this conjugation method, MB does not leach out of the NPs, and the loading of MB in the NPs was optimized for high  $^1\text{O}_2$  production. The prepared MB-conjugated PAA NPs showed significantly lower MB deactivation by enzymes, compared to their respective MB ingredients, giving an expectation of high *in vivo* PDT efficacy. The best  $^1\text{O}_2$  production, for both MBI-NPs and MBII-NPs, was obtained with MB loadings around  $11 \text{ nmol mg}^{-1}$ . Both MBI-NPs and MBII-NPs were modified with the tumor-targeting ligand (F3 peptide) successfully, which improved the selective uptake of these NPs

into human melanoma cells MDA-MB-435. *In vitro* PDT results showed that both kinds of targeted NPs, F3-MBI-PAA-NPs and F3-MBII-PAA-NPs, killed tumor cells effectively, with only 1 min illumination (at *ca.* 100 J cm<sup>-2</sup>), in contrast to the same NPs without F3. None of the NPs, targeted and untargeted, showed dark toxicity.

After chemotherapy treatment, the cancer may relapse and become drug resistant, which is a major barrier towards successful chemotherapy. Chapter 3 presents a codelivery system of doxorubicin (chemodrug) and verapamil (chemosensitizer) using hydrogel NPs, so as to improve the performance of the chemodrug on the MDR cells.[2] These hydrogel NPs were prepared via copolymerization of acrylamide (AA) and 2-carboxyethyl acrylate (CEA), with a varying amount of the CEA towards optimized delivery kinetics. With this nanoplatform, a high loading and a slow release of both Dox and Vera have been achieved successfully. The release kinetics of Dox from the NPs is adjustable, based on the ratio of carboxyl groups per NP. This nanoplatform also protects the Dox from chemical degradation. These NP combinations were well incorporated by the Dox-resistant cell line (NCI/ADR-RES), thus behaving as an efficient delivery vehicle for Dox. Moreover, with the aid of free Vera, and especially with Vera-NPs, the intracellular Dox concentration can be significantly increased, demonstrating the advantage of such a synergistic delivery approach for drug resistant cells. Most importantly, the codelivery of Dox-NPs + Vera-NPs did show a synergistic killing effect on these drug-resistant cells. The IC<sub>50</sub> of Dox-NPs + Vera-NPs was 8 times lower than that of free Dox alone, or Dox-NPs, and 4 times lower than that of free Dox + free Vera.



The negatively charged co(CEA-AA) NP described above is a good delivery vehicle. However, its uptake by tumor cells is limited, since it would be repelled by the cell membrane, which is also anionic. Chapter 4 described the development of peptide-targeted co(CEA-AA) NPs for the targeted delivery of doxorubicin, so as to further facilitate their ability as a drug carrier. The cell surface nucleolin-targeting peptide, F3, was successfully conjugated onto co(CEA-AA) NPs via the copper (I) catalyzed “click chemistry”. This modular conjugation is efficient and is applicable to other kinds of peptide-nanoparticle conjugations. This covalent binding significantly enhances the intracellular uptake of co(CEA-AA) NPs by nucleolin-overexpressing cell lines (e.g. 9L). Our results demonstrate that this enhanced uptake of F3-targeted NPs appears to be correlated with nucleolin-mediated endocytosis. Interestingly, F3-targeted NPs show a much higher uptake by the drug-resistant cell line (NCI/ADR-RES), compared to nontargeted NPs, suggesting that the targeted NPs may bypass the P-glycoprotein efflux pump pathway.[4] This may demonstrate the potential of F3-targeted NPs for the treatment of drug-resistant tumors. The attachment with F3 peptide does not affect much the ability of the NPs to deliver doxorubicin; the targeted, Dox-loaded F3-NPs showed only marginally better *in vitro* cytotoxicity to 9L cells than non-targeted, Dox-loaded NPs. Our findings suggest that the F3-targeted co(CEA-AA) NPs are a promising drug delivery system for further *in vivo* study.

As a carrier of small molecule drugs, hydrogel NPs can also benefit the delivery of tumor contrast agents. A tumor-targeted, intensely blue colored contrast agent, based on PAA NPs, was developed in Chapter 5.[3] The delineation agent, Coomassie Blue (CB), was incorporated into the NPs via copolymerization with acrylamide. With high

loading of CB (7 wt %), the NPs can well stain the tumor area, at a tolerate NP concentration. This covalent conjugation method avoids leaching of the dye from the NPs and the delineation of nontargeted areas, *in vivo*. These CB-conjugated NPs were further modified with PEG and F3 peptide, thus improving their circulation time in the blood-stream, thus enhancing the *in vivo* tumor targeting of these NPs. The *in vivo* tumor delineation experiment, in a 9L tumor-bearing rat model, confirmed the selective and visible tumor staining effect of F3-conjugated CB-PAA NPs, just 2 h after intravenous injection of the NPs. This contrast agent is visible to the naked eye, and can be used for intraoperative tumor delineation, without specialized instruments.

## **Future Directions**

### **Optimization of the NP matrix**

The encouraging results presented in this thesis demonstrated the potential of multifunctional NPs for biomedical applications; however, they are not perfect yet. As mentioned in Chapter 3, codelivery of Dox and Vera with hydrogel NPs showed a synergistic effect on the NCI/ADR-RES cell, an effect that can counteract the multidrug resistance *in vitro*. However, the relatively fast release of Vera from NPs might be a concern, demanding further *in vivo* study. Such further study may be necessary so as to slow down the release kinetics of Vera, which may be achieved via a modification of the NP matrix. We note that the Vera NPs, due to their relatively large dimension (about 50 nm), will pass the tumor, but not the heart endothelial barrier, thus minimizing cardiotoxicity. In addition, to reduce the cardiotoxicity of Vera, a new generation of chemosensitizers, with lower cardiotoxicity, may be used

instead of Vera, e.g., elacridar (an acridonecarboxamide derivative) and tariquidar (an anthranilic acid derivative).[5] The peptide-conjugated NPs in Chapter 4 showed impressive targeting effects toward 9L cells and NCI/ADR-RES cells. However, PEGylation of the NP surface may improve its circulation time *in vivo*.

### ***In vivo* studies of the drug-loaded NPs**

Since most of the NPs described here were studied *in vitro*, extensive *in vivo* studies are needed, towards clinical studies. Some important *in vivo* experiments would include biodistribution, pharmacokinetics studies of the NPs and further therapeutic efficacy studies of the drug-loaded NPs. In particular, for the codelivery of Dox and Vera *in vivo*, a study of optimal dose ratio would also be critical.[6]

### **NP targeting with better tumor-penetrating peptides**

The efficacy of drug-loaded hydrogel NPs is limited by the inefficient extravasation from the blood vessels and penetration through the extravascular stroma. Tumor-penetrating peptides, e.g. iRGD and LyP-1, provide a solution for this challenge.[7] They can recognize the endothelium of tumor vessels, extravasate and penetrate deeply into the tumor extravascular tissue. The tumor-penetrating properties of these peptides are mediated by C-end Rule peptides (CendR) which contain the motif of R/KXXR/K (X represents any amino acid).[7] The CendR binds to neuropilin-1, which is overexpressed on the endothelial cells of tumor blood vessels, thus activating an endocytic bulk transport pathway through tumor tissue.[7] These tumor-penetrating peptides may improve the tumor penetration ability of nanoparticles, by

conjugation of peptides on NPs, or coadministration of peptide with drug-loaded NPs.[8, 9]

### **Codelivery of siRNA and doxorubicin to overcome MDR**

As described in Chapter 4, the therapeutic efficacy of Dox is limited by the multidrug resistance, which is mediated by drug-efflux pumps on the cell membrane, e.g. P-glycoprotein (Pgp). siRNA may knock down Pgp gene expression and improve the intracellular accumulation of Dox. However, the delivery of siRNA *in vivo* is challenging, because of its extremely negative charge, hydrophilicity and easy degradation by enzymes. Here we propose a dual delivery system for Dox and siRNA, based on albumin-PAA hybrid NPs. The anionic siRNA will be loaded into cationic NPs via electrostatic interaction. The incorporation of albumin into the PAA matrix may improve the loading of Dox into the NPs. The synthesis of albumin-PAA hybrid NPs has been studied in our group.[10]

## References

1. Qin, M., et al., *Methylene blue covalently loaded polyacrylamide nanoparticles for enhanced tumor-targeted photodynamic therapy*. Photochemical & Photobiological Sciences, 2011. **10**(5): p. 832-841.
2. Qin, M., et al., *Overcoming Cancer Multidrug Resistance by Codelivery of Doxorubicin and Verapamil with Hydrogel Nanoparticles*. Macromolecular Bioscience, 2013. **Submitted**.
3. Nie, G., et al., *Hydrogel Nanoparticles with Covalently Linked Coomassie Blue for Brain Tumor Delineation Visible to the Surgeon*. Small, 2012. **8**(6): p. 884-891.
4. Ma, P. and R.J. Mumper, *Anthracycline nano-delivery systems to overcome multiple drug resistance: A comprehensive review*. Nano Today, 2013. **8**(3): p. 313-331.
5. Nieto Montesinos, R., et al., *Delivery of P-glycoprotein substrates using chemosensitizers and nanotechnology for selective and efficient therapeutic outcomes*. Journal of Controlled Release, 2012. **161**(1): p. 50-61.
6. Greco, F. and M.J. Vicent, *Combination therapy: Opportunities and challenges for polymer-drug conjugates as anticancer nanomedicines*. Advanced Drug Delivery Reviews, 2009. **61**(13): p. 1203-1213.
7. Teesalu, T., K.N. Sugahara, and E. Ruoslahti, *Tumor penetrating peptides*. Frontiers in Oncology, 2013. **3**.
8. Sugahara, K.N., et al., *Coadministration of a Tumor-Penetrating Peptide Enhances the Efficacy of Cancer Drugs*. Science, 2010. **328**(5981): p. 1031-1035.
9. Hu, Q., et al., *F3 peptide-functionalized PEG-PLA nanoparticles co-administrated with tLyp-1 peptide for anti-glioma drug delivery*. Biomaterials, 2013. **34**(4): p. 1135-1145.
10. Yoon, H.K., et al., *Polymer-protein hydrogel nanomatrix for stabilization of indocyanine green towards targeted fluorescence and photoacoustic bio-imaging*. Journal of Materials Chemistry B, 2013. **1**(41): p. 5611-5619.